Dynamic Modeling and Control of Spherical Robots

Thesis by
Matthew Ryan Burkhardt

In Partial Fulfillment of the Requirements for the
degree of
Doctor of Philosophy

CALIFORNIA INSTITUTE OF TECHNOLOGY
Pasadena, California

2018
Defended May 7th, 2018

Matthew Ryan Burkhardt
ORCID: 0000-0002-4240-7496

ACKNOWLEDGEMENTS

I would first like to acknowledge my adviser, Dr. Joel Burdick. During my time at Caltech, I have come to believe that Joel's efforts, and perhaps a measure of his own success, are aimed at the professional and personal development of the students he advises. I am honored to have held Joel's trust throughout these years and I am grateful that Joel believed in both my abilities and character. I will sorely miss the intellectual flexibility and creative freedom that characterize the Burdick group.

Moreover, I would like to thank my committee: Dr. Richard Murray, Dr. Paul Backes, Dr. Aaron Ames, and Dr. Soon-Jo Chung. In particular, thank you to Dr. Murray for enlightening conversations on Lagrangian reduction, and allowing me to add to the theory that he and Dr. Burdick labored over early in their careers.

I am grateful to NASA for supporting my research through a NASA Space Technology Research Fellowship. In particular, thank you to Dr. Dannette Allen, Jeff Antol, and Paul Rothhaar for hosting me at NASA Langley Research Center's (LaRC) Autonomy Incubator in 2016. Thank you to Dr. Paul Backes, Dr. Sisir Karumanchi, and Kyle Edelberg for welcoming me into the Jet Propulsion Laboratory's (JPL) Robotic Manipulation and Sampling Group in 2017. These experiences exposed me to interesting problems I would not have otherwise encountered, and it was a pleasure to work alongside the dedicated NASA researchers at both LaRC and JPL.

I must also acknowledge Faranak Davoodi, Dr. Junichi Asama, Joe Bowkett, and Mike Jenson. Faranak Davoodi invented the Moball and introduced me to the project. Dr. Asama dedicated himself to the Moball project for over two years and developed the electrical systems necessary for energy-harvesting. I thoroughly enjoyed working with Dr. Asama and will miss the daily lessons on Japanese culture. Joe Bowkett and Michael Jenson provided significant help on the design and experimentation of Moball. Joe conducted energy-harvesting and control tests that helped validate the Moball concept and Mike patiently improved the design of the vehicle as we tested new ideas and learned from our past mistakes.

Graduate school is not meant to be endured alone, and I was lucky to experience it with a close group of loyal friends. I have fond memories of navigating through the first year with Andres Goza, Alex Zelhofer, Anthony Massari, and Tess Saxton-Fox. I am especially thankful to my fellow Burdick group members for the welcome diversions in the office, lunches at Chandler, and late night team-bonding at Roy's.

Of course, I owe a great deal of gratitude to my family. My parents taught by their example and imbued into our family the values of hardwork, sacrifice, public service, and humility. I now have the happy fortune of grasping at once unforeseen opportunities, a circumstance that must be ascribed to the tireless efforts of my parents. I am also grateful to the Anzelmos, for welcoming me into their familty and caring for me as one of their own.

And certainly this thesis would not be possible without the indefatigable patience and support of my wife Michelle. This daring woman married a young graduate student with only a vague conception of the future. Nonetheless, she was invested in the graduate school experiment, she encouraged me to trust my judgment along the way, and to never lose sight of the vision we set for ourselves. Completing this work is an achievement to her as much as it is to me.

ABSTRACT

In this work, a rigorous framework is developed for the modeling and control of spherical robotic vehicles. Motivation for this work stems from the development of Moball, which is a self-propelled sensor platform that harvests kinetic energy from local wind fields. To study Moball's dynamics, the processes of Lagrangian reduction and reconstruction are extended to robotic systems with symmetry-breaking potential energies, in order to simplify the resulting dynamic equations and expose mathematical structures that play an important role in subsequent control-theoretic tasks. These results apply to robotic systems beyond spherical robots. A formulaic procedure is introduced to derive the reduced equations of motion of most spherical robots from inspection of the Lagrangian. This adaptable procedure is applied to a diverse set of robotic systems, including multirotor aerial vehicles.

Small time local controllability (STLC) results are derived for barycentric spherical robots (BSR), which are spherical vehicles whose locomotion depends on actuating the vehicle's center of mass (COM) location. STLC theorems are introduced for an arbitrary BSR on flat, sloped, or smooth terrain. I show that STLC depends on the surjectivity of a simple *steering matrix*. An STLC theorem is also derived for a class of commonly encountered multirotor vehicles.

Feedback linearizing and PID controllers are proposed to stabilize an arbitrary spherical robot to a desired trajectory over smooth terrain, and direct collocation is used to develop a feedforward controller for Moball specifically. Moball's COM is manipulated by a novel system of magnets and solenoids, which are actuated by a "ballistic-impulse" controller that is also presented. Lastly, a motion planner is developed for energy-harvesting vehicles. This planner charts a path over smooth terrain while balancing the desire to achieve scientific objectives, avoid hazards, and the imperative of exposing the vehicle to environmental sources of energy such as local wind fields and topology. Moball's design details and experimental results establishing Moball's energy-harvesting performance ($7W$ while rolling at a speed of $2m/s$), are contained in an Appendix.

PUBLISHED CONTENT AND CONTRIBUTIONS

M.R. Burkhardt and J.W. Burdick. "Reduced Dynamical Equations for Barycentric Spherical Robots." In: *2016 International Conference on Robotics and Automation (ICRA).* DOI: 10.1109/ICRA.2016.7487434

Geometric reduction and reconstruction as applied to spherical robots, included in Chapter 3.

J. Bowkett, M.R. Burkhardt, and J.W. Burdick. "Combined Energy Harvesting and Control of Moball: A Barycentric Spherical Robot." In: *2016 International Symposium on Experimental Robotics.* DOI: 10.1007/978-3-319-50115-4_7

Energy-harvesting analysis of three dimensional Moball with preliminary control experiments, forming part of Appendix A.

J. Asama, M.R. Burkhardt, F. Davoodi, and J.W. Burdick. "Design Investigation of a Coreless Tubular Linear Generator for a Moball: A Spherical Exploration Robot with Wind-Energy Harvesting Capability." In: *2015 International Conference on Robotics and Automation (ICRA).* DOI: 10.1109/ICRA.2015.7139007

Optimization of Moball's electromechanical subsystem, included in Appendix A.

M.R. Burkhardt et al. "Energy Harvesting Analysis for Moball, A Self-Propelled Mobile Sensor Platform Capable or Long Duration Operation in Harsh Terrains." In: *2014 International Conference on Robotics and Automation (ICRA).* DOI: 10.1109/ICRA.2014.6907241

Preliminary simulations of Moball's energy-harvesting mechanism, forming part of Appendix A.

TABLE OF CONTENTS

LIST OF ILLUSTRATIONS

LIST OF TABLES

Number *Page*

Chapter 1

INTRODUCTION

Spherical robots represent an alternative design paradigm to conventional wheeled or tracked field vehicles. A spherical robot is generally characterized by an external spherical shell that contains an internal drive mechanism, which enables active steering and control. Naturally, rolling is the primary means of locomotion for a spherical robot, although other modalities (e.g. hopping, jumping) are possible. Spherical robots are actively being developed and deployed in a broad range of applications ranging from the commercial (see Fig. 1.1) to planetary science missions.

(a) Remote controlled toy *BB-8* from the Star Wars franchise[1].

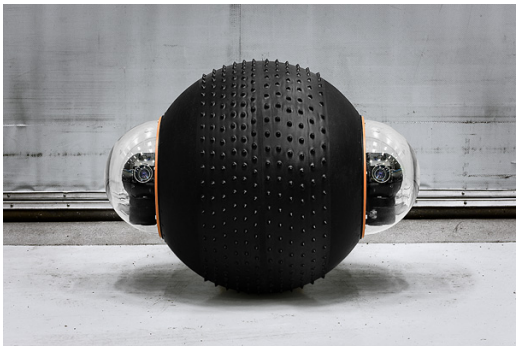

(b) Rotundus GroundBot security robot[2].

Figure 1.1: Commercial Applications of Spherical Robots.

1.1 Spherical Vehicles and Planetary Science

This thesis is motivated in part by the application of spherical robots to support planetary science missions. Many planetary science missions require *in situ* measurements over a large spatial area. The operational environment may be harsh, located far from human settlement, with limited conventional energy resources available. Consider an atmospheric survey of the Arctic, whereby temperature, humidity, and chemical concentrations (e.g. CO_2, CH_4, O_3) are desired at regular intervals over the ice. A vehicle for such a mission must contend with extreme temperatures, unreliable solar energy, and potentially hazardous obstacles. Furthermore, mea-

[1]Image courtesy of Sphero, http://www.sphero.com.
[2]Image used with permission from Rotundus, http://www.rotundus.se/.

surements should be continually available in order to track climatic changes over long periods.

Spherical robots possess distinct advantages that are well-suited for a planetary science mission of this kind. The external shell can be hermetically sealed, protecting the vehicle from moisture and dirt, as well as offering thermal insulation. A spherical robot can move omnidirectionally and does not have a preferred orientation like tracked or wheeled vehicles, which mitigates concern about stability and maneuverability on undulating or sloped terrain. The hardware of a spherical robot is often simple and reliable, as suspensions and gearboxes are typically unneccesary. A spherical robot can also maneuver over debris that may be otherwise impassable; an inflatable spherical vehicle developed in [41] was able to traverse obstacles up to one-third of its diameter.

Incorporating energy-harvesting capabilities into spherical robots is necessary to support planetary science missions. Many scientific environments of interest are characterized by unreliable solar power availability. Shadows cast by craters on the Moon, dust accumulation on Mars, and the long winter in the Arctic all impose serious solar energy limitations that reduce the scientific opportunities of surface assets. Depending on solar power is even less tenable for scientific environments further from the Sun than Earth or Mars. Moreover, scientists increasingly want to sample environmental data for long periods of time. Thus, next-generation planetary exploration robots should be energy-opportunistic in the sense that domestic sources of energy can be recovered to prolong mission life. The Moball is one such vehicle that combines mobility with energy harvesting from sustained winds.

1.2 Moball Mobile Sensor Platform

Moball is a mobile sensor platform that harvests energy from sustained wind gusts, and whose development motivates the work in this thesis (see Appendix A). Moball's energy harvesting and locomotion stems from a unique electromechanical apparatus shown in Fig. 1.2a. Contained within Moball are six tubes arranged along three orthogonal axes. A permanent dipole magnet slides along a rod within the center of each tube. Concentric and exterior to each internal tube are several copper solenoids.

Energy-harvesting relies on electrical induction between the solenoids and moving magnets. A sustained wind-gust imparts a force on Moball, causing it to roll. Consequently, Moball's internal magnets reciprocate through the solenoids. As the

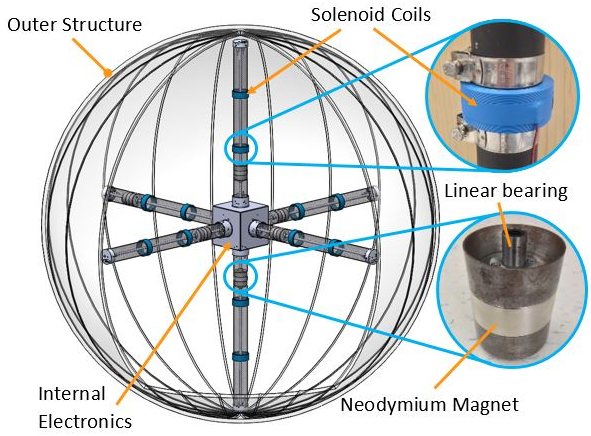

(a) Diagram of Moball showing major structural components.

(b) Moball with closed external shell.

(c) Moball with open shell, displaying internal hardware.

Figure 1.2: Moball Mobile Sensor Platform.

magnets pass through the solenoids, part of the magnet's kinetic energy is converted into electrical energy via induction and stored in an on-board battery for later use. Experiments (Appendix A) showed that a $2m$- diameter Moball with two solenoids per tube travelling at approximately 1.25 m/s harvested 4-5 watts of usable power.

Locomotion is enabled by operating the same electromechanical apparatus "in reverse." Applying a current to a solenoid will impart a force on a nearby magnet. By coordinating the currents applied to each solenoid, all of the magnets can be actively positioned to manipulate the vehicle's center of mass (COM). Moving the COM away from the geometrical center of rotation (COR) offsets the vehicle's equilibrium and causes the vehicle to roll. This is the basis of Moball's active control.

Moball is intended to operate in harsh environments with consistent surface winds. Candidate environments of scientific interest include Earth's polar regions, Mars, and Saturn's moon Titan [25]. It is envisioned that dozens of Moballs would be deployed to form a dense sensor network over a large spatial area [26]. Peer-to-peer communication and self-propulsion would enable such a network to adapt flexibly to changing mission requirements. Moball's energy-harvesting capability would also reduce battery mass. Currently, approximately 20%-30% of spacecraft mass is attributed to power systems [60]; as an energy-opportunistic sensor platform, Moball's power system can be made smaller and cheaper than conventional designs.

1.3 Taxonomy of Spherical Robots

Moball is one of many types of spherical robot, which can be classified based on the method used for self-propulsion. Barycentric spherical robots (BSR) are actively steered by moving the vehicle's COM away from its COR. Moball is an example of a BSR since interior magnets are used to displace the COM. Commonly-encountered BSRs rely on the following mechanisms for self-propulsion (examples of which are shown in Fig. 1.3):

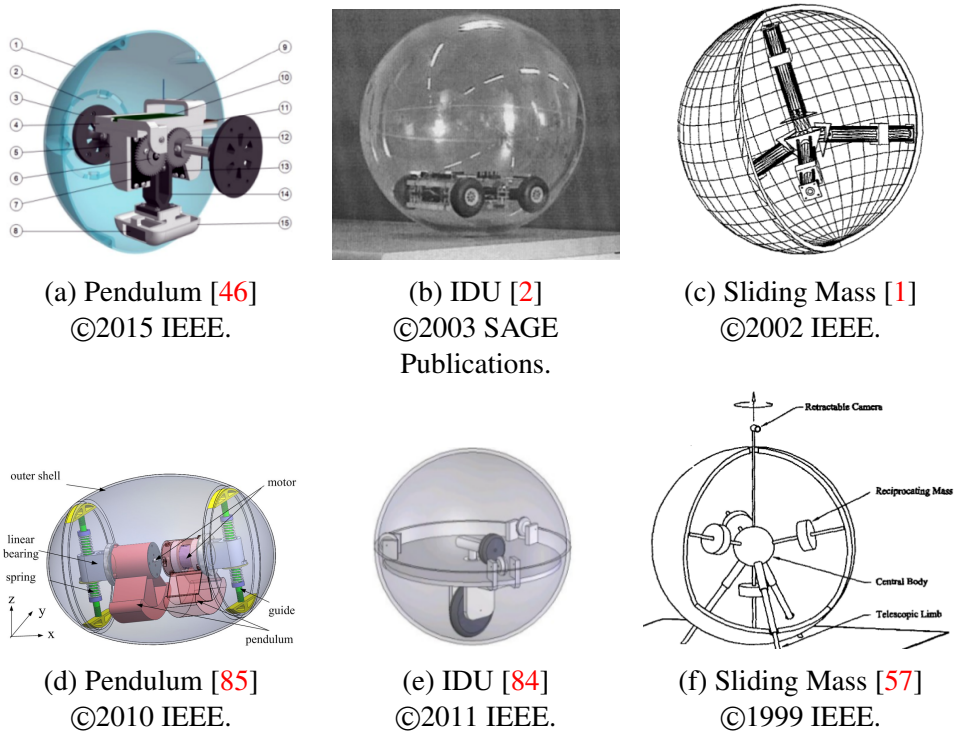

(a) Pendulum [46] ©2015 IEEE.

(b) IDU [2] ©2003 SAGE Publications.

(c) Sliding Mass [1] ©2002 IEEE.

(d) Pendulum [85] ©2010 IEEE.

(e) IDU [84] ©2011 IEEE.

(f) Sliding Mass [57] ©1999 IEEE.

Figure 1.3: Various Barycentric Spherical Robots (BSR).

1. *Pendulums*. An internal pendulum is rotated such that the pendulum bob

points in the direction of desired travel [46, 85].

2. *Internal Drive Units (IDU)*. Masses attached to wheels are "driven" on the inner surface of the vehicle's shell. Such vehicles resemble hamster balls and have been developed by several researchers [2, 13, 84].

3. *Sliding Masses*. Like Moball, these vehicles rely on masses that move along prismatic axes to control the COM position [1, 57].

Many other spherical robots rely on the conservation of angular momentum for self-propulsion. Typically, these vehicles are actuated by internal flywheels [12, 79]. A torque applied to the flywheel generates a reaction torque on the external shell via the conservation of angular momentum. Gyroscopic precession is relied upon in vehicles actuated by control moment gyroscopes (CMG) [23]. In these vehicles, an input torque is applied perpendicularly to the spinning axis of a flywheel, which generates an output torque along the remaining orthogonal direction via precession. The maximum torque of angular-momentum based vehicles is constrained by the speed/torque applied to the internal flywheels. Consequently, these vehicles often generate larger driving torques than BSRs, whose maximum torque is constrained by the diameter of the vehicle, i.e. the COM cannot be placed outside the robot's external shell. However, spherical robots relying on flywheels cannot harvest kinetic energy as easily as BSRs. Exotic locomotion modalities, including shape-changing spherical robots, have been developed and can be found in the review by Chase et. al [22].

Several passive, wind-powered spherical vehicles have been developed. In 2000, Jack Jones of NASA's Jet Propulsion Laboratory (JPL) was testing an tricycle rover concept with inflatable wheels (Fig. 1.4a) when one wheel broke loose. Much to the amazement of the researchers, the runaway wheel demonstrated the ability to traverse rough terrain and climb steep slopes [34, 41]. This was the motivation for JPL's Tumbleweed rover (Fig. 1.4c). Tumbleweed is an inflated $1.5m$-diameter sphere, which is passively blown by wind gusts. Ambient pressure and temperature are measured from an onboard electronic package and data is transmitted via the Iridium satellite network to a ground station far from the field [11]. In 2003, Tumbleweed was deployed to Greenland where it traversed $131km$ in 9 days [51]. The following year, Tumbleweed traveled $134km$ in 7 days at the South Pole and $200km$ in 7 days back in Greenland [51]. These field tests verify the feasibility of wind-driven mobility over difficult terrain in extremely challenging environments.

(a) JPL's Jack Jones and the inflatable tricycle.

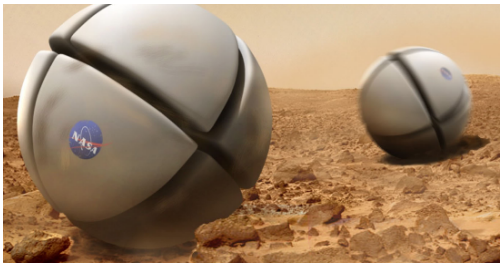

(b) LaRC Wedge

(c) Tumbleweed in Greenland [11]. ©2004 IEEE.

(d) LaRC Dandelion

Figure 1.4: Passive Wind-Powered Spherical Vehicles.

However, Tumbleweed's disadvantages include an uncontrollable trajectory due to the lack of active control and a mission duration limited by the onboard battery.

Similarly, NASA's Langley Research Center (LaRC) developed the concept of "deployable open-structures" [3, 4]. These biomimetically-inspired vehicles have open, rather than closed, external shells. Features such as pockets, cutouts, and cups are designed into the shell to capture a passing breeze. Examples include the "wedge" (Fig. 1.4b) and the "dandelion" design (Fig. 1.4d). Several prototypes were tested in a wind-tunnel to identify the design with the maximum drag coefficient over a large range of vehicle orientations. The LaRC prototypes are envisioned to be deployed en masse, with a mission of sampling Mars's climate similar to Moball. Of course, these vehicles are again characterized by an uncontrollable trajectory and reliance on an onboard battery.

Lastly, a few researchers have considered pendulum-actuated BSRs that harvest energy from sustained winds. The internal pendulum of these vehicles swings along a single preferred axis, which is attached to a motor/generator. In [27, 37], the equations of motion are derived for an energy-harvesting pendulum robot and Lyapunov stability is assessed. In [10], an inflatable $2m$-diameter vehicle weighing

$30kg$ was built and tested. During a single experiment, the vehicle was propelled by the wind to a speed of 30 km/hr, generating 3 watts of useful power [10]. An energy-harvesting BSR based on sliding masses, like Moball, has the advantage of harvesting energy from rotations in any direction as compared to pendulum-based vehicles. Furthermore, manipulating the COM during active control is costly for pendulum-based BSRs due to the high torque caused by the pendulum bob on the motor.

1.4 Challenges of Spherical Robots

Although spherical vehicles offer a competitive set of advantages compared to conventional mobility platforms, these vehicles also face unique challenges. Generally, a spherical robot can be modeled as a dynamical system whose inputs are the velocities of its internal actuators (e.g. sliding masses, pendulum, etc.) and whose output is the vehicle's inertial state. Most models also include constraints that prohibit the sphere from skidding and/or turning in place. For conventional wheeled or tracked vehicles, these constraints imply that the dynamical system's inputs are kinematically related to its outputs. This dramatically simplifies the analysis as the engineer can use the kinematic relationship to understand the input-output mapping. For most spherical robots, however, the system's inputs and outputs are not kinematically related. Instead, the inputs directly affect the system's momentum, which in turn affects the vehicle's position, or inertial state. This indirect relationship can make it more challenging to understand how actuator policies correspond to vehicle behaviors, but it is clear that understanding the evolution of momentum is key.

Another challenge confronting spherical robots arises when modeling the vehicle's orientation. Unlike conventional land and air vehicles, whose motions deviate only slightly from a desired stable orientation, the orientation of spherical vehicles may assume any rotational state. Consequently, the dynamic linearization modeling techniques popular with conventional vehicles cannot be applied to spherical robots, whose governing dynamics are inherently nonlinear. Furthermore, although standard methods of parameterizing the vehicle's rotation state (e.g. Euler angles, quaternions, etc.) can be employed, this approach typically results in overcomplicated equations of motion that obscure insight into the vehicle's dynamics. Of course, choosing to retain the rotation matrix as a state variable increases the dimension of the problem and introduces cumbersome constraints on the orientational state. Equations of motion, which hold globally, and that incorporate the vehicle's orientation without parameterization are desirable for spherical robots.

Lastly, the constraints that prohibit skidding and/or turning in place are nonholonomic velocity constraints[3]. These constraints, in combination with the indirect input-output relationship described above, result in convoluted equations of motion with forcing terms arising from the constraints, actuation, and fictitious forces. In turn, any controllability conditions and motion controllers derived from these complex equations are often intricate and unintuitive. These salient theoretical issues must be resolved before spherical vehicles can be confidently deployed in the high-risk environments that characterize planetary science missions. This dissertation leverages the mathematical structures underlying the equations of motion of spherical robots to simplify and solve these challenges.

1.5 Thesis Contributions & Organization

The process of Lagrangian reduction has a history stretching back to the early 20th century [61, 68, 71]. A symmetry[4] occurs when the Lagrangian, constraints, and external forces are invariant with respect to the action of a group. In such cases, the equations of motion can be "reduced" to a lower-dimensional configuration space that does not include the symmetry group. In addition to being defined over a smaller space, the reduced equations of motion are often algebraically simpler, which aids in the analysis of subsequent control-theoretic issues. For many dynamical systems, including most robotic systems of interest, the configuration space can be expressed as a direct product $Q = G \times M$, where G is a Lie group and M is a smooth manifold. For robotic systems, G often describes the vehicle's inertial pose and M denotes the states of internal actuators. If the Lagrangian system is invariant with respect to the group G, then the system can be reduced to a lower-dimensional space as described above. Inertial motions are then recovered by solving the lower-dimensional equations of motion and "reconstructing" the full dynamics including the inertial state using a reconstruction equation [45]. For robotic systems, the reconstruction equation naturally describes how momenta and internal actuation affect inertial motion, which can be used to provide insight into a range of practical control-theoretic issues [35, 67, 75, 76].

Reduction and reconstruction of mechanical systems is limited by the largest common symmetry group shared by the Lagrangian, constraints, and external forces. Often, a parameter dependency (e.g. the direction of gravity) in a mechanical system's potential energy or constraint set limits the extent of reduction possible.

[3] See Chapter 2 for precise definitions.
[4] See Chapter 3 for precise definitions.

This parameter is said to "break" the symmetry of the system. One method to overcome a broken symmetry is to introduce additional states into the Lagrangian called advected parameters [21, 74, 82]. By choosing an advected parameter that corresponds to the parameter breaking the system's symmetry, the augmented Lagrangian system can often be made invariant with respect to the maximal symmetry group. The result is a reduced set of equations coupled to an additional equation governing the evolution of the advected parameter. Although this technique permits reduction of systems with broken symmetries, a reconstruction process, and the concomitant benefits of the reconstruction equation, have not been incorporated.

This thesis contributes a novel reduction and reconstruction approach to dynamical systems with symmetry-breaking potential energies and nonholonomic constraints. Consequently, these results can be applied to a variety of vehicle platforms far removed from spherical vehicles e.g., multirotor, legged, and underwater vehicles. Furthermore, the reduced/reconstructed equations can be written from inspection of the system's Lagrangian, and the equations can be easily generalized to vehicles operating on undulating terrains. This original reduction/reconstruction approach is then applied to the equations of motion for a wide class of spherical robots, including all BSR vehicles. Reduction by the rotation group obviates the challenges associated with modeling the vehicle's orientation. Reconstruction allows the equations to be written in an intuitive form, highlighting the role of momentum in sustaining vehicle motion while revealing mathematical structures that play a definitive role in assessing controllability.

Small-time local controllability (STLC) conditions are also developed for a wide class of spherical robots, including all BSR vehicles. Necessary STLC conditions follow from determining the rank of a simple *steering matrix*, whose terms depend on quantities identified in the reduced/reconstructed equations of motion. Similarly, these STLC conditions can be checked by simple inspection of the system's Lagrangian, which enables one to easily determine how damage or changes to the vehicle's internal design affect controllability. Controllability conditions for spherical vehicles on flat, sloped, and generic undulating terrain are presented.

An intuitive, generic feedback controller and energy-opportunistic motion planning framework are also contributed for the BSR vehicle class. Each of these components are extendable to generic terrains. For Moball specifically, a feedforward controller is developed using a low-order dynamic model and the direct collocation scheme. This thesis also contributes a "ballistic-impulse" controller for Moball,

which can be used to control the position of Moball's magnets in spite of the limited control authority inherent to the electromechanical design. Path planning, feedback, and feedforward controllers are combined in a simulation environment to assess Moball's ability to traverse paths on flat and generic, smooth terrain.

The remainder of the thesis is organized as follows. Chapter 2 contains mathematical preliminaries adopted in the remaining chapters. Chapter 3 presents a Lagrangian method for the reduction and reconstruction of nonholonomic mechanical systems, which is employed to simplify the equations of motion of spherical robots. Next, necessary STLC conditions are derived for a generic class of spherical robot in Chapter 4. Chapter 5 presents feedback controllers and a path planning framework for BSRs, in addition to a feedforward controller and simulation results for the Moball. Chapter 6 highlights future work and concludes the thesis. In Appendix A, one can find details on Moball's design and experimental results.

Chapter 2

PRELIMINARIES

This brief chapter contains mathematical preliminaries that are used throughout the remainder of the thesis.

2.1 Configuration Spaces

This thesis is motivated by spherical robots that can be modelled as a finite set of rigid bodies, e.g. the external shell, internal masses, and internal rotors are all assumed to be rigid. The generalized coordinates of a single rigid body are the variables $\{q_1, \ldots, q_n\}$ that are sufficient to specify the body's position and pose. The space of generalized coordinates necessary to specify all rigid bodies composing a spherical robot is called the configuration space, Q. The state of the vehicle,

$$q = \{q_1, \ldots, q_m\} \in Q,$$

represents a specific vehicle configuration, i.e. the position and pose of every rigid body is fully specified. The degrees of freedom (DOF) of a spherical robot is defined as the number of independent variables that span Q, i.e. $\dim(Q) = m$. For spherical vehicles with actuated internal components, the configuration space can be expressed as a direct product, $Q = G \times M$, where G and M denote the generalized coordinates corresponding to the external shell and all internal components (e.g. masses, rotors), respectively.

2.2 Differentiable Manifolds

The configuration spaces of interest are differentiable manifolds,

Definition 2.2.1 (Differentiable Manifold [14])**.** An m-dimensional differentiable manifold P is a set of points together with a finite or countably infinite set of subsets $U_\alpha \in P$ and 1-to-1 mappings $\varphi_\alpha : U_\alpha \to \mathbb{R}^n$ such that:

1. $\bigcup_\alpha U_\alpha = P$.
2. For each nonempty intersection $U_\alpha \cup U_\beta$, $\varphi_i(U_\alpha \cup U_\beta)$ is an open subset of $\mathbb{R}^n$, and the 1-to-1 and onto mapping $\varphi_\alpha \circ \varphi_\beta^{-1} : \varphi_\beta(U_\alpha \cup U_\beta) \to \varphi_\alpha(U_\alpha \cap U_\beta)$ is a smooth function.

3. The family $\{U_\alpha, \varphi_\alpha\}$ is maximal with respect to conditions 1 and 2.

Each set U_α is called a coordinate chart and each φ_α is a coordinate function. The second condition is necessary to ensure that the transition between neighboring charts has continuous partial derivatives. The third condition ensures that a manifold is specified independent of the specific coordinate charts chosen. This thesis assumes that the configuration space is a C^2-differentiable manifold, whereby the transition maps $\varphi_\alpha \circ \varphi_\beta^{-1}$ have continuous partial derivatives up to the second order. A configuration space Q that is a differentiable manifold may also be called a configuration manifold.

The tangent vector on a differentiable manifold is defined as follows,

Definition 2.2.2 (Tangent Vector [19])**.** A differentiable map $\gamma : (-\epsilon, \epsilon) \to P$ is called a curve on P. Assume that $\gamma(0) = p$ and let D denote the set of functions on P that are differentiable at p. The tangent vector to the curve γ at $t = 0$ is the function $\gamma'(0) : D \to \mathbb{R}$ given by,

$$\gamma'(0)(f) = \frac{d(f \circ \gamma)}{dt}\Big|_{t=0}, \quad f \in D.$$

A tangent vector at a point $p \in P$ is the tangent vector at $t = 0$ of some curve $\gamma : (-\epsilon, \epsilon) \to P$ with $\gamma(0) = p$.

The space of all tangent vectors at a point $p \in P$ is called the tangent space and is denoted T_pP. The tangent space is independent of the coordinate chart used, and is a vector space of the same dimension as the manifold P. Given a local coordinate chart $\varphi_\alpha : U_\alpha \to \mathbb{R}^n$, a natural basis spanning the tangent space at p is given by $\{(\partial/\partial x_1), \ldots, (\partial/\partial x_n)\}$, where $(\partial/\partial x_i)$ is the i^{th} standard basis vector of $\mathbb{R}^n$ projected by φ_α^{-1}.

Definition 2.2.3 (Tangent Bundle [14])**.** The tangent bundle of a manifold P, denoted by TP, is the differentiable manifold whose underlying set is the disjoint union of the tangent spaces to P at the points $x \in P$, i.e.,

$$TP = \bigcup_{x \in P} T_xP.$$

Definition 2.2.4 (Cotangent Bundle [14])**.** The dual to the tangent space, T_xP, is the cotangent space, T_x^*P. Members of the cotangent space are called one-forms and are linear functionals mapping $T_xP \to \mathbb{R}$. The cotangent bundle of a manifold P,

denoted by T^*P, is the differentiable manifold whose underlying set is the disjoint union of the cotangent spaces to P at the points $x \in P$, i.e.,

$$T^*P = \bigcup_{x \in P} T_x^* P.$$

2.3 Lie Groups

The space of generalized coordinates describing the inertial state of a spherical robot's external shell are often Lie groups.

Definition 2.3.1 (Group [59])**.** A set S together with a binary operation $\circ$, defined on elements of S, is a group if the following axioms are satisfied:

1. *Closure*: If $s_1, s_2 \in S$, then $s_1 \circ s_2 \in S$.
2. *Identity*: An identity element exists, e, such that $s \circ e = e \circ s = s$ for all $s \in S$.
3. *Inverse*: For every $s \in S$, a unique inverse exists such that $s^{-1} \in S$ and $s \circ s^{-1} = s^{-1} \circ s = e$.
4. *Associativity:* If $s_1, s_2, s_3 \in S$, then $(s_1 \circ s_2) \circ s_3 = s_1 \circ (s_2 \circ s_3)$.

Definition 2.3.2 (Lie Group [14])**.** A Lie group is a smooth manifold P that is a group, and for which the group operations of multiplication $(p_1, p_2) \rightarrow p_1 p_2$ for $p_1, p_2 \in P$, and inversion $p \rightarrow p^{-1}$, are smooth.

Definition 2.3.3 (Matrix Lie Group [14])**.** A matrix Lie group is a set of invertible $n \times n$ matrices that is closed under matrix multiplication and that is a submanifold of $\mathbb{R}^{n \times n}$.

Matrix Lie groups play an important role in the modeling of spherical robots. The Special Orthogonal Group in 3-dimensions, SO(3), is defined by,

$$SO(3) = \left\{ A \in \mathbb{R}^{3\times 3} | A^T A = A A^T = I, \det(A) = +1 \right\},$$

where $\det(\cdot)$ is the standard matrix determinant. The columns of matrices belonging to $SO(3)$ naturally represent the bases of a right-handed orthonormal frame. Consequently, the SO(3) group is used to model the orientation of rigid bodies. The Special Orthogonal Group defines a non-Euclidean space, which implies that SO(3) is not closed under addition, i.e. if $S_1, S_2 \in SO(3)$ then $S_1 + S_2 \notin SO(3)$. Practically, this will prohibit standard numerical integration and derivative techniques,

which depend on a Euclidean structure, from being applied to SO(3) (an integration scheme that respects the structure of SO(3) is employed in Chapter 5).

Another important matrix group is the Special Euclidean Group in 3-dimensions, $SE(3)$,

$$SE(3) = \left\{(v, R) | v \in \mathbb{R}^3, R \in SO(3)\right\} = \mathbb{R}^3 \times SO(3).$$

Elements of $SE(3)$ are typically represented as $\mathbb{R}^{4\times4}$ matrices,

$$A = \begin{bmatrix} R & v \\ \vec{0} & 1 \end{bmatrix} \in SE(3),$$

where $\vec{0}$ is a three-dimensional row vector. Members of the Special Euclidean Group can be used to represent the position (in the v-component) and the orientation (in the R-component) of a rigid body.

Definition 2.3.4 (Translations and Adjoint [14])**.** For a Lie group G, the left-translation can be defined as $L_g : G \to G$ such that $L_g(h) = g \circ h$. Similarly, the right-translation is defined by $R_g : G \to G$ such that $R_g(h) = h \circ g$. The adjoint action $AD_g : G \times G \to G$ is defined by $AD_g h = L_g(R_{g^{-1}} h) = g \circ (h \circ g^{-1})$. For matrix Lie groups these operations follow simply from matrix multiplication.

2.4 Matrix Lie Algebras

The tangent space at the identity element of a Lie group, T_eG, is a special vector space that satisfies the conditions of a Lie algebra.

Definition 2.4.1 (Matrix Lie Bracket [14])**.** For any pair of $n \times n$ matrices A, B the matrix Lie bracket is defined by $[A, B] = AB - BA$.

Proposition 2.4.1. The matrix Lie bracket satisfies the following properties:

1. *Bilinearity*: For $n \times n$ matrices A, B, C and scalars $\alpha, \beta, \gamma \in \mathbb{R}$,

$$[\alpha A + \beta B, C] = \alpha[A, C] + \beta[B, C],$$
$$[A, \beta B + \gamma C] = \beta[A, B] + \gamma[A, C],$$

2. *Skew-symmetry*: For any $n \times n$ matrices A and B, $[B, A] = -[A, B]$.

3. *Jacobi Identity*: For any $n \times n$ matrices A, B, C,

$$[[A, B], C] + [[B, C], A] + [[C, A], B] = 0.$$

Definition 2.4.2 (Matrix Lie Algebra [14])**.** A matrix Lie algebra $\mathfrak{g}$ is a set of $n \times n$ matrices that is a vector space with respect to matrix addition and scalar multiplication, which is also closed under the matrix Lie bracket $[\cdot, \cdot]$.

Proposition 2.4.2 ([14])**.** For any matrix Lie group G, the tangent space at the identity T_eG is a Lie algebra, denoted $\mathfrak{g}$.

Let a Lie group tangent vector be denoted by $\dot{g} \in T_gG$. For non-Abelian Lie groups such as SO(3) and SE(3), there are two natural ways to map $\dot{g}$ back to the Lie algebra T_eG. The first is by using the lifted-left action $T_gL_{g^{-1}}$ and the second is by using the lifted-right action $T_gR_{g^{-1}}$. These actions correspond to left and right multiplication by the inverse for matrix Lie groups, e.g. $\dot{R} \in T_RSO(3)$ may be mapped back to the Lie algebra using a lifted-left action $R^{-1}\dot{R} \in \mathfrak{so}(3)$ or a lifted-right action $\dot{R}R^{-1} \in \mathfrak{so}(3)$, where $\mathfrak{so}(3)$ is the Lie algebra of SO(3) defined by,

$$\mathfrak{so}(3) = \left\{A \in \mathbb{R}^{3\times3} | A^T = -A\right\},$$

which is the space of skew-symmetric 3×3 matrices. Elements of $\mathfrak{so}(3)$ are characterized by three independent parameters. Thus, it is natural to represent members of $\mathfrak{so}(3)$ as vectors in $\mathbb{R}^3$ using the wedge map $\wedge : \mathbb{R}^3 \to \mathfrak{so}(3)$,

$$\begin{bmatrix} v_1 \\ v_2 \\ v_3 \end{bmatrix}^\wedge = \begin{bmatrix} 0 & -v_3 & v_2 \\ v_3 & 0 & -v_1 \\ -v_2 & v_1 & 0 \end{bmatrix} \in \mathfrak{so}(3)$$

The inverse of the $\wedge$ map is the $\vee : \mathfrak{so}(3) \to \mathbb{R}^3$ operator. A tangent vector defined on $SE(3)$, $\dot{G} \in T_GSE(3)$ can analogously be mapped via lifted-right or lifted-left actions to the Lie algebra $\mathfrak{se}(3)$,

$$\mathfrak{se}(3) = \left\{ \begin{bmatrix} \hat{\omega} & v \\ 0_{1\times3} & 0 \end{bmatrix} \in \mathbb{R}^{4\times4} \middle| \hat{\omega} \in \mathfrak{so}(3), v \in \mathbb{R}^3 \right\}.$$

Elements of $\mathfrak{se}(3)$ are defined by 6 independent quantities, and $\wedge$ and $\vee$ operators exist similarly to those defined for $\mathfrak{so}(3)$ [59].

The lifted-left and lifted-right actions have important physical meanings for $\mathfrak{so}(3)$ and $\mathfrak{se}(3)$. Lie algebra elements that have been mapped to the Lie algebra using the lifted-left action correspond to velocities expressed in a body-fixed coordinate frame, e.g. $R^T\dot{R} = \hat{\omega}^b \in \mathfrak{so}(3)$ corresponds to an angular velocity viewed from a coordinate frame fixed to a moving rigid body. Similarly, $G^{-1}\dot{G} = \xi^b \in \mathfrak{se}(3)$ corresponds to an angular velocity and translational velocity viewed with respect

to a body frame. The lifted-right action produces velocities expressed with respect to a fixed spatial frame, $\dot{R}R^T = \hat{\omega}^s \in \mathfrak{so}(3)$ and $\dot{G}G^T = \xi^s \in \mathfrak{se}(3)$. Thus, the Lie algebra is the space of body and spatial velocities for spherical robots. Body-coordinates are used in developing the equations of motion of spherical robots in this thesis.

The adjoint operator between a Lie group and a Lie algebra member, $Ad : G \times \mathfrak{g} \rightarrow \mathfrak{g}$, is defined as $Ad_g\xi = T_{g^{-1}}L_g(T_eR_{g^{-1}}\xi)$, which for matrix groups corresponds to $Ad_g\xi = g\xi g^{-1}$. This relationship enables one to easily convert between body and spatial coordinates on the Lie algebra, i.e. $\xi^s = Ad_g\xi^b$. The adjoint operation between Lie algebra members, $ad : \mathfrak{g} \times \mathfrak{g} \rightarrow \mathfrak{g}$, is defined as $ad_\xi\eta = [\xi, \eta]$, which will play an important role in the forthcoming controllability calculations.

Just as tangent vectors can be mapped to the Lie algebra, a Lie algebra member ξ can be mapped back onto a tangent space of the Lie group using a left, $T_eL_g\xi$, or right, $T_eR_g\xi$, action. This action applied to all $g \in G$ results in a vector field defined over the Lie group, which depends on ξ. Let this vector field be denoted by $X_\xi(g) \in \mathcal{X}(Q)$, where $\mathcal{X}(Q)$ denotes the set of all smooth vector fields defined over Q. Let $\phi_\xi : \mathbb{R} \rightarrow G$ be the integral curve of $X_\xi(g)$ that passes through the identity element $e \in G$ when $t = 0$. Then,

Definition 2.4.3 (Exponential Map [59])**.** The function $\exp : \mathfrak{g} \rightarrow G$ defined by $exp(\xi) = \phi_\xi(1)$ is called the exponential map of the Lie algebra $\mathfrak{g}$ into the Lie group G. The exponential map takes the line $\xi s \in \mathfrak{g}$, $s \in \mathbb{R}$, into a one-parameter subgroup of G, i.e.

$$exp(\xi s) = \phi_\xi(s).$$

For the Special Orthogonal Group SO(3), the exponential map is available in closed-form via the Rodrigues' formula,

$$e^{\hat{\omega}} = I + \frac{\hat{\omega}}{||\omega||}sin||\omega|| + \frac{\hat{\omega}^2}{||\omega||^2}(1 - cos||\omega||),$$

for $\omega \in \mathbb{R}^3 \in SO(3)$. An analogous relationship exists for $SE(3)$ as well. The exponential map is important because it allows reduced dynamical systems to be analyzed on the Lie algebra, where the results can be projected into the Lie group when explicit rotation matrices are required for computation. In Chapter 5, a vector-based integration scheme acting on the Lie algebra $\mathfrak{so}(3)$ is used to integrate dynamics on $SO(3)$, and the results are projected back to G using the exponential map.

2.5 Nonholonomic Constraints

Interactions between a spherical robot and the terrain are governed by motion constraints. Prohibitions against penetrating the ground plane, slipping, or turning in place are all represented via appropriate constraints.

Definition 2.5.1 (Holonomic Constraints [59])**.** A holonomic constraint restricts the motion of the system to a smooth hypersurface of the configuration space Q. Holonomic constraints can be represented locally as algebraic constraints on the configuration space,

$$h_i(q) = 0, \quad i = 1, \ldots, k.$$

A relevant example of a holonomic constraint includes mandating that a spherical robot cannot separate from a flat plane. Velocity constraints that can be integrated to pure positional constraints are holonomic. If the configuration space has dimension m, then a set of k independent holonomic constraints will effectively reduce the dynamical system's degrees of freedom to $m - k$. Consequently, the equalities in Definition 2.5.1 can be used to simplify the equations of motion by eliminating k variables.

Definition 2.5.2 (Nonholonomic Constraints)**.** Consider velocity constraints of the form $A(q)\dot{q} = 0$, where $A(q) \in \mathbb{R}^{k \times m}$ and $\dim(Q) = m$. Nonholonomic velocity constraints cannot be integrated into holonomic constraints.

Physically, nonholonomic constraints limit a dynamical system's velocities without explicitly restricting the configuration manifold Q. An example of a nonholonomic constraint is the no-slip constraint between a ball and a flat plate. This constraint mandates that a rotation of the ball results in a corresponding translation, in proportion to the ball's radius. Although this constraint couples rotational and translational velocities, the ball can occupy any position and orientation contained in Q. Given a set of nonholonomic constraints, the allowable velocities are enumerated by the constraint distribution $\mathcal{D}$.

Definition 2.5.3 (Constraint Distribution)**.** The constraint distribution is defined as,

$$\mathcal{D} = \{(q, \dot{q}) \in T_q Q \mid A(q)\dot{q} = 0\}.$$

At $q \in Q$, the velocities allowed by the constraints is written as $\mathcal{D}(q)$.

The coordinates chosen to express the constraint distribution $\mathcal{D}$ have a strong impact on the complexity of the resulting equations of motion, as Chapter 3 will show.

2.6 Lagrangian Dynamics

Traditionally, the equations of motion of multibody robotic systems are derived using a Lagrangian approach. For the types of mechanical robots considered here, the Lagrangian is defined as follows:

Definition 2.6.1 (Lagrangian)**.** The Lagrangian of a mechanical system, $L : TQ \to \mathbb{R}$, is defined as $L(q, \dot{q}) = T(q, \dot{q}) - V(q)$, where $T(q, \dot{q})$ and $V(q)$ represent the net kinetic and potential energy, respectively.

For the spherical robots of interest here (and most mechanical systems), the kinetic energy is a quadratic function in the generalized velocities $\dot{q}$. If the generalized velocities are expressed in spatial coordinates, then $T(q, \dot{q}) = \dot{q}^T \mathcal{M}_s(q)\dot{q}$, where $\mathcal{M}_s$ is the spatial mass matrix. Similarly, when the generlized velocities are expressed in body coordinates, $T(q, \dot{q}) = \dot{q}^T \mathcal{M}_b(q)\dot{q}$, where $\mathcal{M}_b$ is the body mass matrix. As the name suggests, the mass matrices contain the masses and inertias of the mechanical system.

Definition 2.6.2 (Nonholonomic Mechanical System)**.** A nonholonomic mechanical system is defined by the tuple $\Sigma = (Q, L, \mathcal{D}, F)$ where:

(A1) Q denotes a configuration space, assumed to be finite-dimensional.

(A2) $L : TQ \to \mathbb{R}$ is a smooth Lagrangian, where smoothness is defined with respect to the arguments $(q, \dot{q})$. The potential is conservative and $L(q, \dot{q})$ is hyperregular [54].

(A3) Motions are constrained by an independent set of k nonholonomic constraints that define a constraint distribution, $\mathcal{D}$, which is assumed to be smooth as a distribution.

(A4) External forces are expressed as one-forms $F(q, \dot{q}) \in T^*Q$.

Nonholonomic mechanical systems are the most basic class of dynamical systems considered in this work. For these systems, the equations of motion follow from solving the variational Lagrange-d'Alembert principle.

Theorem 2.6.1 (Constrained Lagrange-d'Alembert Principle [54])**.** Given a Lagrangian $L(q, \dot{q})$, a force field $F(q, \dot{q})$, and a constraint distribution $\mathcal{D}(q, \dot{q})$, the

Lagrange-d'Alembert principle for a curve $q(t) \in Q$ is:

$$\delta \int_a^b L(q(t), \dot{q}(t))\, dt \;+\; \int_a^b F(q(t), \dot{q}(t)) \cdot \delta q \; dt \;=\; 0, \tag{2.1}$$

for all curves $q(t)$ and variations $\delta q(t) \in \mathcal{D}_{q(t)}$ such that $\delta q(a) = \delta q(b) = 0$.

External forces derived from potential functions, e.g. gravitational or magnetic forces, are called potential forces and can be represented as one-forms $F(q) = -dV(q)$. These forces play a special role in the Lagrange-d'Alembert principle, namely:

Corollary 2.6.1. [17] Based on assumptions **(A1)**-**(A4)**, the Lagrange-d'Alembert principle (2.6.1) can be rewritten in terms of the kinetic energy $T(q, \dot{q})$, a potential force $-dV(q)$, and external forces, $F(q, \dot{q})$:

$$\delta \int_a^b T(q, \dot{q}) dt \;=\; \int_a^b dV(q) \cdot \delta q \; dt - \int_a^b F(q, \dot{q}) \cdot \delta q \; dt, \quad \delta q \in \mathcal{D}\,. \tag{2.2}$$

This result asserts dynamical equivalence between the nonholonomic mechanical systems $\Sigma_L = (Q, L, \mathcal{D}, F)$ and $\Sigma_T = (Q, T, \mathcal{D}, -dV + F)$.

The equations of motion follow from the constrained Lagrange-d'Alembert principle (2.6.1) via the Euler-Lagrange equations.

Proposition 2.6.1 (Euler-Lagrange [65])**.** A path $\gamma : [a, b] \to Q$ satisfies the nonholonomic constrained principle (2.6.1) if $\dot{\gamma}(t) \in \mathcal{D}$ for all $t \in [a, b]$ and,

$$\frac{d}{dt}\left(\frac{\partial L(\gamma, \dot{\gamma})}{\partial \dot{q}}\right) - \frac{\partial L(\gamma, \dot{\gamma})}{\partial q} = \lambda A(\gamma) + F(\gamma, \dot{\gamma}),$$

where $\mathcal{D} = \left\{(q, \dot{q}) \in T_q Q \mid A(q)\dot{q} = 0\right\}$ and λ_i for $i = 1, \ldots, k$ are Lagrange multipliers.

Traditionally, the lagrange multiplers λ_i are solved for algebraically, leaving m second-order differential equations and k first-order differential equations comprising the equations of motion. In the next chapter, an equivalent set of dynamical equations will be derived in an intuitive, geometric-based form that does not rely on Lagrange multipliers.

Chapter 3

LAGRANGIAN REDUCTION OF NONHOLONOMIC MECHANICAL SYSTEMS

A spherical robot can be modeled as a nonholonomic mechanical system (Definition 2.6.2). Before developing the equations of motion for spherical robots, a Lagrangian reduction and reconstruction method is introduced for the class of nonholonomic mechanical systems with broken symmetries. The resulting approach will produce the equations of motion for a wide class of spherical robots, and other relevant systems including multirotor and legged vehicles. First, the relevant basics of Lagrangian reduction and reconstruction will be reviewed.

3.1 Review of Reduction & Reconstruction

This section contains necessary background information on Lagrangian reduction, nonholonomic momenta, principal bundles and connections, semi-direct product spaces, the Bloch-Krishnaprasad-Marsden-Murray (BKMM) reduction/reconstruction method, and reduction via advected parameters.

3.1.1 Lagrangian Reduction

Similar to a Lie group's left-translation, $L_g : G \to G$, a Lie group may also act on a manifold via a left action,

Definition 3.1.1 (Lie Group (Left) Action [54])**.** Let P be a manifold and let G be a Lie group. A (left) action of a Lie group G on P is a smooth mapping $\Phi : G \times P \to P$ such that,

1. $\Phi(e, x) = x$ for all $x \in P$, where $e \in G$ is the Lie group's identity element.
2. $\Phi(g, \Phi(h, x)) = \Phi(gh, x)$ for all $g, h \in G$ and $x \in P$.

Definition 3.1.2 (Free Action [65])**.** An action $\Phi(g, x)$ is free if it does not have fixed points, i.e. $\Phi(g, x) = x$ implies that $g = e$ for all $x \in P$.

Typically, $\Phi(g, x)$ will be denoted by $\Phi_g(x)$. A right action can be similarly defined, but the left action is consistent with our choice of modeling the equations of motion

using body coordinates. The left-action $\Phi_g(x)$ has a collateral effect on tangent vectors that is described by the lifted action.

Definition 3.1.3 (Lifted Action [14])**.** The lifted action is the map,

$$T\Phi_g : TQ \to TQ : (q,v) \to (\Phi_g(q), T_q\Phi_g(v)),$$

which relates the tangent space T_qQ to $T_{\Phi_g(q)}Q$.

Then, the concept of G-invariance can be introduced.

Definition 3.1.4 (Lie Group Invariance [65])**.** A Lagrangian function, $L : TQ \to \mathbb{R}$, a vector field $X \in \mathcal{X}(Q)$, and a one-form $\omega \in \mathcal{X}^*(Q)$, are said to be G-invariant if they are invariant with respect to the induced action of Lie group G on Q, i.e.,

$$\begin{aligned} L(\Phi_g(q), T_q\Phi_g\dot{q}) &= L(q,\dot{q}), \\ T_q\Phi_g X(q) &= X(\Phi_g(q)), \\ T_q^*\Phi_g\omega(\Phi_g(q)) &= \omega(q), \end{aligned}$$

respectively, which holds for all $g \in G$ and $\dot{q} \in T_qQ$.

Definition 3.1.5 (Symmetry)**.** A nonholonomic mechanical system (2.6.2) possesses a *symmetry* with respect to a Lie group G if its Lagrangian $L : TQ \to \mathbb{R}$, constraint distribution $\mathcal{D}(q,\dot{q}) \in \mathcal{X}(Q)$, and external forces $F(q,\dot{q}) \in \mathcal{X}^*(Q)$, are all G-invariant according to definition (3.1.4).

Symmetries allow the equations of motion to be "reduced" to a lower-dimensional space, TQ/G, which is the quotient space between the configuration space and the symmetry group. This is the basis of Lagrangian reduction.

Reduction was used by early pioneers including Euler, Lagrange, Hamilton, and Jacobi. Routh's reduction of cyclic variables, Poincaré's generalization of Euler's equations to Lie groups, and Noether's conservation laws are notable examples of early work [61, 68, 71]. The modern era of reduction began in the 1960s with Arnold's work on the dynamics of rigid bodies and ideal fluids, Smale's treatment of relative equilibria in celestial mechanics problems, and the synthesis of these works in Abraham and Marsden, amongst others [5, 55, 80]. A comprehensive historical review of reduction is provided by Marsden [55].

An intuitive understanding of symmetries follows from identifying a symmetry with transformations to a dynamical system's inertial coordinate system that do

not change the resulting equations of motion. For example, consider a spherical robot rolling on a flat plane. It is clear that translating the inertial coordinate system along a horizontal plane would not change a rolling ball's equations of motion (the ball should roll the same if it is measured from any location on the plane). However, translating the inertial frame in a vertical direction *would* alter the equations of motion via changes to the measurement of potential energy. Thus, a spherical robot rolling on a flat plane has a symmetry with respect to horizontal, but not vertical, translations.

Although the dynamics of most spherical robots can be simplified using symmetries, some vehicles (including BSRs like Moball) can only be partially reduced due to "broken" symmetries. Consider a mechanical system with $Q = G$, a finite-dimensional Lie group. Assume invariance of the kinetic energy with respect to the left-action Φ_g, for all $g \in G$. Furthermore, suppose that the potential $V(g, a_0)$ depends upon a parameter $a_0 \in \mathbb{R}^n$, e.g. $a_0 \in \mathbb{R}^3$ may be a unit vector collinear with the direction of gravity in an inertial frame. The Lagrangian will then be invariant with respect to the isotropy subgroup $G_{a_0} = \{g \in G \mid g \cdot a_0 = a_0\}$, and since $G_{a_0} \subset G$, the parameter a_0 is said to "break" the G-symmetry. The symmetry condition (3.1.5) only then applies to G_{a_0}. Although reduction by G_{a_0} is possible, one is forced to parameterize G/G_{a_0} in the resulting equations of motion, which imposes additional complexity when G is a subgroup of $SE(3)$.

Broken symmetries typically occur in nonholonomic mechanical systems whenever the potential energy or constraints depend on a parameter expressed in an inertial frame. For example, spherical robots often have broken symmetries due to a dependency on the direction of gravity (the standard basis vector e_3) in the potential, $V(q)$, or a dependency on the surface normal over which the vehicle rolls in $\mathcal{D}(q, \dot{q})$. Broken symmetries are ubiquitous across a broad class of field vehicles, as a dependency on the direction of gravity in $V(q)$ is almost always encountered. These broken symmetries will prevent the equations of motion from being decomposed using the geometric method of BKMM (3.1.5), but in Section (3.2) a method relying on advected parameters (see 3.1.6) is developed to overcome this challenge.

3.1.2 Nonholonomic Momentum

Symmetries are naturally associated with momenta that play a major role in the motion of spherical robots. In the absence of constraints, Noether's theorem associates symmetries with conserved quantities that are interpreted as momenta. In the

presence of nonholonomic constraints, "nonholonomic" or "generalized" momenta may not be conserved but differential equations describing their evolution can be derived, and their derivation will now be reviewed [45].

Definition 3.1.6 (Group Orbit)**.** The group orbit for the left action $\Phi_g(q)$ on a manifold P is the set,

$$Orb(q) = \{\Phi_g(q) | \ \forall g \in G\}.$$

The tangent space to the orbit at $q \in Q$ is denoted by $T_q Orb(q)$.

When G is the Lagrangian symmetry group, the tangent space $T_q Orb(q)$ represents velocities along the symmetry directions. Then, the number of generalized momenta depends on the dimension of the set $\mathcal{S}_q$,

$$\mathcal{S}_q = \mathcal{D}_q \cap T_q Orb(q), \tag{3.1}$$

where $\mathcal{S}_q$ can be interpreted as the tangent vectors that simultaneously lie along symmetry directions and satisfy the nonholonomic constraints.

Definition 3.1.7 (Infinitesimal Generator)**.** For a given element of the Lie algebra $\xi \in \mathfrak{g}$, define a flow $\gamma^\xi(t,x) = \Phi(exp(t\xi), x)$, where $t \in \mathbb{R}$ and $x \in P$, where P is a smooth manifold. The vector field,

$$\xi_P(x) = \frac{d}{dt}\bigg|_{t=0} \gamma^\xi(t,x),$$

is the *infinitesimal generator* of the action corresponding to ξ.

The infinitesimal generator produces a vector field defined over the manifold analogous to the vector field resulting from projecting a Lie algebra element onto G via a left or right action. For each $q \in Q$, where Q is the configuration manifold of a mechanical system, the set of Lie algebra elements whose infinitesimal generators lie in $\mathcal{S}_q$ is denoted by $\mathfrak{g}^q$,

$$\mathfrak{g}^q = \left\{\xi \in \mathfrak{g} \mid \xi_Q(q) \in \mathcal{S}_q\right\}.$$

Let the bundle over Q, with fibers $\mathfrak{g}^q$ at $q \in Q$, be denoted by $\mathfrak{g}^{\mathcal{D}}$ [45]. The nonholonomic momentum map defines the momenta that are consistent with the nonholonomic constraints. Each generalized momenta obeys a differential equation described in the following theorem.

Definition 3.1.8 (Nonholonomic Momentum Map [45])**.** The nonholonomic momentum map $J^{nhc} : T_qQ \to (\mathfrak{g}^{\mathcal{D}})^*$ is defined by,

$$\langle J^{nhc}(\dot{q}), \xi \rangle = \Big\langle \frac{\partial L}{\partial \dot{q}}, \xi_Q \Big\rangle,$$

where $\xi \in \mathfrak{g}^q$, and $\langle \cdot, \cdot \rangle$ denotes the standard vector inner-product.

Theorem 3.1.1. [45] Assume that the Lagrangian of a mechanical system is invariant with respect to Φ_g. Then, any solution to the Lagrange-d'Alembert equations for a nonholonomic system must satisfy, in addition to the given kinematic constraints, the momentum equation:

$$\frac{d}{dt}\Big(\langle J^{nhc}(\dot{q}), \xi^{q(t)} \rangle\Big) = \Big\langle \frac{\partial L}{\partial \dot{q}}, \frac{d}{dt}(\xi^{q(t)})_Q \Big\rangle.$$

The differential equation of the nonholonomic momenta shown above underlies the momentum equations that appear in the BKMM method (3.1.5), as well as the generalization to broken symmetries in Section (3.2).

3.1.3 Principal Bundles & Connections

The configuration spaces of the systems considered in this work are assumed to be trivial principal fiber bundles.

Definition 3.1.9 (Principal Fiber Bundle[65])**.** A principal fiber bundle over M with group G consists of a manifold Q and a free and proper left action of G on Q satisfying the following:

1. M is the quotient space of Q defined by the G-induced equivalence relation, $M = Q/G$, where the canonical projection $\pi : Q \to M = Q/G$ is differentiable.

2. Q is locally trivial. Every point $q \in Q$ has a neighborhood U such that $\pi^{-1}(U)$ is isomorphic to $G \times U$. Thus, there exists a diffeomorphism $\psi : \pi^{-1}(U) \to G \times U$ given by $\psi(q) = (\varphi(q), \pi(q))$, for which $\varphi : \pi^{-1}(U) \to G$ satisfies $\varphi(\Phi_g q) = L_g \varphi(q)$ for all $g \in G$ and $q \in U$.

A principal fiber bundle can locally be described as $Q = G \times M$, however in this work most of the systems of interest will admit a global representation of $Q = G \times M$, as defined by the trivial principal fiber bundle[1].

[1] Many of the results in this work can be extended to principal bundles through the use of local trivializations.

Definition 3.1.10 (Trivial Principal Fiber Bundle [65])**.** A trivial principal fiber bundle is a manifold $Q = G \times M$ such that G acts freely on Q on the left by trivially extending L_g to act on Q. This implies that $\Phi_h(g,r) = (L_h g, r)$ for $h \in G$ and $(g,r) \in G \times M = Q$.

The manifold M is called the base or shape space, which describes the state of a spherical robot's internal actuators or passive mechanisms. The group G describes the position and orientation of the vehicle. Every fiber bundle is equipped with a projection $\pi : Q \to M$. The kernel of this projection's tangent map determines the vertical space, $V_q Q = \ker(T_q \pi)$. A principal connection defines a complementary horizontal space:

Definition 3.1.11 (Principal Connection)**.** A principal connection is an assignment of a horizontal subbundle, $H_q Q \subset T_q Q$, such that for each $q \in Q$,

1. $T_q Q = V_q Q \oplus H_q Q$, $V_q Q \cap H_q Q = \vec{0}$.
2. $T_q \Phi_g H_q Q = H_{g \cdot q} Q$, for every $q \in Q$ and $g \in G$.
3. $H_q Q$ depends smoothly on q.

Definition 3.1.12 (Principal Connection Form)**.** A principal connection form $\mathcal{A} : TQ \to \mathfrak{g}$ is a Lie-algebra valued map with the following properties:

1. $\mathcal{A}(q)$ is linear on TQ.
2. $\mathcal{A}(q)\xi_Q(q) = \xi$ for all $\xi \in \mathfrak{g}$ and $q \in Q$.
3. $\mathcal{A}(\Phi_g(q)) T_q \Phi_g(\dot{q}) = Ad_g \mathcal{A}(q)\dot{q}$ for all $\dot{q} \in T_q Q$ and $g \in G$.

Equivalently, a connection defines a horizontal space of $T_q Q$, $H_q Q = \ker(\mathcal{A}(q))$. While the choice of a horizontal space is not unique, a connection is defined in the next section so that $H_q Q$ represents the allowable system motions and incorporates symmetries using definitions (3.1.11)-(3.1.12). For a fiber bundle $Q = G \times M$, one can express the principal connection form acting on $\dot{q} \in T_q Q$ in local coordinates as follows,

$$\mathcal{A} \cdot \dot{q} = \mathcal{A}_g(g,m)\dot{g} + \mathcal{A}_m(g,m)\dot{m} = Ad_g(g^{-1}\dot{g} + \mathcal{A}^{loc}(m)\dot{m}), \tag{3.2}$$

where $\mathcal{A}^{loc} \equiv \mathcal{A}_m(e,m)$. The forthcoming reconstruction process will be formulated in terms of a principal connection where the Lie group G is a semidirect-product group. This process provides a means to understand how actuation and momenta contribute to inertial motion, which in turn leads to an improved understanding of control and motion-planning issues as in [35],[75].

3.1.4 Semi-Direct Product Space

The Lie group G of a spherical robot's configuration space often has the following structure, which is assumed from this point forward. G is a semidirect product space,

$$G = H \circledS \mathcal{V},$$

where $H \subset G$ is a Lie subgroup and $\mathcal{V}$ is a vector space. The group H acts on the space $\mathcal{V}$ linearly from the left, and on Q via a left-action. The symbol Ⓢ denotes the semi-direct product, which defines the multiplication of group members as follows:

$$(h_1, v_1) \cdot (h_2, v_2) = (h_1 h_2, h_1 v_2 + v_1),$$

and the inverse of $(h,v) \in G$ is given by $(h^{-1}, -h^{-1}v)$. The identity element for the group is given by $(e,0) \in G$. Lie algebra elements take the form,

$$\xi = (h^{-1}\dot{h}, h^{-1}\dot{v}) \in \mathfrak{g},$$

where $\mathfrak{g} = \mathfrak{h} \times T\mathcal{V} \simeq \mathfrak{h} \times \mathcal{V}$. An arbitrary tangent vector is denoted as $(\dot{h}, \dot{v}) \in TG$. In coordinates, the left action of $g = (h,v) \in G$ on $(l,p,m) \in H \circledS \mathcal{V} \times M$ is given by,

$$\Phi_g(l,p,m) = (hl, hp + v, m),$$

and the lifted action is given by,

$$T_q\Phi_g(\dot{l}, \dot{p}, \dot{m}) = (h\dot{l}, h\dot{p}, \dot{m}).$$

For a Lie algebra element $\xi = (\xi_h, \xi_v) \in \mathfrak{g}$, with $\xi_h \in \mathfrak{h}$ and $\xi_v \in T\mathcal{V}$, the infinitesimal generator applied to $(l,p,m) \in Q$ can be written as,

$$\xi_Q(l,p,m) = (\xi_h l, \xi_h p + \xi_v, 0),$$

which will be used to define the nonholonomic momenta in what follows. Lastly, the adjoint operation $Ad : G \times \mathfrak{g} \to \mathfrak{g}$ follows via,

$$Ad_g\xi = (Ad_h(\xi_h), h\xi_v - Ad_h(\xi_h)v) \in \mathfrak{g},$$

where $g = (h,v) \in G$ and $Ad_h(\cdot) = h(\cdot)h^{-1}$.

3.1.5 BKMM Method

Bloch et. al [45] developed a method to reduce and reconstruct nonholonomic mechanical systems with symmetries whose configuration spaces are principal fiber bundles. Their mechanical systems are characterized by a Lagrangian, constraint distribution, and external forces (Definition 2.6.2) that are left-invariant with respect to a common symmetry group G, a finite-dimensional Lie group. For these systems, the equations of motion reduce to the form:

$$\xi = g^{-1}\dot{g} = -\mathbb{A}(r)\dot{r} + \mathbb{I}^{-1}(r)\vec{p}, \tag{3.3}$$

$$\dot{p}_i = \dot{r}\cdot\alpha_i(r)\dot{r} + \dot{r}\cdot\beta_i(r)\vec{p} + \vec{p}\cdot\gamma_i(r)\vec{p}, \quad \forall i = [1,n], \tag{3.4}$$

$$M(r)\ddot{r} = -C(r,\dot{r}) + N(r,\dot{r},\vec{p}) + \tau. \tag{3.5}$$

The structure of these equations follows from a reduced variational principle with an extended base space consisting of the nonholonomic momenta $\vec{p} = (p_1,\ldots,p_n)$ and shape-space variables $(r,\dot{r})$. The momentum differential equation (3.4) follows from Theorem 3.1.1, where the basis vectors of $\mathcal{S}_q$ have been expressed in body coordinates. Equation (3.5) governs motion in the base space, and this equation can be derived from a reduced variational principle [65]. The quantities $M(r)$, $C(r,\dot{r})$, and $N(r,\dot{r},\vec{p})$ represent the mass-matrix, Coriolis forces, and potential forces such as gravity, respecitvely. Actuator forces are assumed to occur along the base directions[2] and are represented by the vector τ.

The reconstruction equation (3.3) describes motion along the fibers as the flow of a left-invariant vector field. Operators $\mathbb{A}(r)$ and $\mathbb{I}^{-1}(r)$ are the *nonholonomic connection* and *locked inertia tensor*, respectively. As will explained in Chapter 4, equations (3.3) and (3.4) provide intuitive insight into the controllability of constrained multibody dynamical systems. The G-invariance of these equations also alleviates the need to explicitly parameterize the group G, which is convenient when $SO(3) \subseteq G$. In practice, these features have facilitated insight into a range of practical control issues. For example, the reconstruction equation (3.3) that maps base motions to fiber motions is naturally applicable to robotic gait-planning [64, 67], while structure in the reconstruction and momentum equations leads to necessary conditions for controllability and optimality [44, 63]. Ostrowski [62, 66] showed that the reduced equations can be computed by inspecting the reduced Lagrangian, which has led to applications on a variety of vehicle platforms [56, 76].

[2] External forces (including dissipative forces) can be incorporated into the momentum and shape-space differential equations (3.4)-(3.5) as well [66].

Unfortunately, the BKMM method does not readily apply to systems with "broken" symmetries, since it reduces by the largest symmetry group shared by the kinetic energy, potential energy, and nonholonomic constraints. In these cases, it is not possible to reduce by the kinetic energy's symmetry group due to the presence of the external parameter. In the presence of broken symmetries, the BKMM method requires a separable parameterization of the kinetic energy's symmetry group that is compatible with the parameter's isotropy group. For groups such as $SO(3)$, the complexity incurred by this parameterization obscures insight into practical control issues. The use of an *advected parameter* in the reduction process, however, enables one to maintain the appealing structure developed by Bloch et. al [45] in the presence of broken symmetries, thereby simplifying the analysis of many multibody dynamical systems of interest.

3.1.6 Reduction Using Advected Parameters

In the context of rigid body mechanical systems, an advected parameter is defined as follows.

Definition 3.1.13 (Advected Parameter)**.** An advected parameter is a vector $a(t) \in \mathcal{V}$ expressed in a body frame that satisfies the differential equation,

$$\Big(\frac{d}{dt} + g^{-1}(t)\dot{g}(t)\Big)a(t) = 0,$$

where $g \in G$ is a Lie group element.

An advected parameter for rigid body mechanical systems is typically defined as $a(t) = R^T(t)a_0$, where $R \in SO(3)$ and $a(t)$ models a vector a_0 that is constant in inertial space, e.g. $a_0 = e_3$ represents the direction of gravity where $a(t)$ represents the direction of gravity expressed in a body frame. More general notions of advected parameters have been applied to the study of fluid mechanics [21, 38].

To illustrate how advected parameters simplify the reduction process, consider again the simple system with a broken symmetry introduced in (3.1.1): A mechanical system with $Q = G$, Φ_g-invariance of the kinetic energy, and a potential $V(g, a_0)$ that depends upon a parameter $a_0 \in \mathbb{R}^n$.

Define an augmented Lagrangian $\bar{L} : TG \times \mathbb{R}^n \to \mathbb{R}$ that incorporates a_0 as an additional state. If the augmented Lagrangian is Φ_g-invariant, where G acts on $\mathbb{R}^n$ from the left, then the augmented Lagrangian function can be reduced to $l = L(\xi, \Gamma)$ over the space $\mathfrak{g} \times \mathbb{R}^n$, where

$$\Gamma \triangleq g^{-1}a_0,$$

denotes an advected parameter. An advection equation governs the advected parameter,

$$\dot{\Gamma} = -\xi\Gamma,$$
$$\Gamma(t_0) = g^{-1}(t_0)a_0,$$

which follows from Definition (3.1.13). Applying the Lagrange-d'Alembert principle to the reduced Lagrangian yields a modified form of the Euler-Poincaré equations.

Theorem 3.1.2. [21] Let $\bar{L}\colon TG\times\mathbb{R}^n \to \mathbb{R}$ be left-invariant with respect to Φ_g. For a curve $g(t) \in G$, where $\xi(t) = g^{-1}(t)\dot{g}(t)$, the following are equivalent:

(i) $g(t)$ satisfies the Euler-Lagrange equations for L on G.

(ii) With a_0 constant, the variational principle

$$\delta \int_a^b L(g(t), \dot{g}(t), a_0)\, dt \;=\; 0$$

holds for all variations $\delta g(t)$ with fixed endpoints, $\delta g(a) = \delta g(b) = 0$.

(iii) The modified Euler-Poincaré equations hold:

$$\frac{d}{dt}\frac{\delta l}{\delta \xi} - ad^*_\xi \frac{\delta l}{\delta \xi} = \frac{\delta l}{\delta \Gamma} \diamond \Gamma, \text{ where } \dot{\Gamma} = -\xi\Gamma$$

where the operator $\diamond$ is defined by $\langle \eta\Gamma, v\rangle = -\langle v \diamond \Gamma, \eta\rangle$, and $\Gamma, v \in \mathbb{R}^n$, $\eta \in \mathfrak{g}$.

(iv) The constrained variational principle

$$\delta \int_a^b l(\xi(t), \Gamma(t))\, dt \;=\; 0$$

holds on $\mathfrak{g}\times\mathbb{R}^n$, using variations ξ and Γ of the form

$$\delta\xi = \dot{\eta} + [\xi, \eta], \quad \delta\Gamma = -\eta\Gamma,$$

where $\eta(t) \in \mathfrak{g}$ vanishes at the endpoints a and b.

Essentially, reduction by the Lie group is occurring on a larger-dimensional augmented configuration space (due to the incorporated advected parameter) at the expense of an additional advection equation in the resulting equations of motion. Often, the simplification gained by reduction of G is worth the cost of introducing the advection equation, whose dynamics are particularly simple.

Building upon the advected parameter method demonstrated above, Schneider [74] develops a reduction process for mechanical systems with broken symmetries governed by nonholonomic constraints. Schneider's "General Theorem" applies to systems defined over semidirect product spaces, i.e. $Q = H \circledS \mathcal{V}$, where advected parameters are elements of $\mathcal{V}$. Constraints of the following form[3] are assumed:

$$\dot{v} = \theta(h, v, a_0)\dot{h}, \tag{3.6}$$

where $(v, \dot{v}) \in T\mathcal{V}$ and $(h, \dot{h}) \in TH$. To reduce the dynamics to the space $\mathfrak{h} \circledS \mathcal{V} \times W$, where $W = G/G_{a_0} \simeq \mathcal{V}$, an invariance condition must hold for both the constraints and Lagrangian (and any external forces). The constraint distribution must satisfy the following invariance condition for all $(f, y) \in H \circledS \mathcal{V}$ and $a_0 \in \mathcal{V}$,

$$f\theta(h, v, a_0) = \theta(fh, fv + y, ha_0)f\dot{h}. \tag{3.7}$$

If the constraints satisfy this invariance condition, then v can be shown to be cyclic by choosing $(f, y) = (e, -v)$. This enables the reduced constraints to have the form $\xi_v = \theta(\Gamma)\xi_h$, where $\theta(\Gamma) : \mathfrak{h} \to \mathcal{V}$ and the reduced variables are defined by,

$$(\xi_h, \xi_v) = (h^{-1}\dot{h}, h^{-1}\dot{v}),\ \Gamma \triangleq h^{-1}a_0.$$

Similarly, the Lagrangian must be invariant with respect to the following transformation where for $(f, y) \in H \circledS \mathcal{V}$,

$$(f, y) \cdot (h, \dot{h}, v, \dot{v}, a) = (fh, f\dot{h}, fv + y, f\dot{v}, fa), \tag{3.8}$$

which again implies that the Lagrangian is cyclic in v. Then,

Theorem 3.1.3. [74] Under the aforementioned constraints (3.6) and invariances (3.7)-(3.8), the following are equivalent:

(i) $(h(t), v(t)) \in H \circledS \mathcal{V}$ satisfy the Euler-Lagrange equations for L on Q.

(ii) The curve $(h(t), v(t)) \in Q$ satisfies the constrained Lagrange-d'Alembert principle. That is, $(\dot{h}, \dot{v}) \in \mathcal{D}$ and,

$$\delta \int_a^b L(h(t), \dot{h}(t), \dot{v}(t))dt = 0,$$

where $\delta h(t)$ is an independent variation that vanishes at the endpoints and $\delta v = \theta(h, a_0)\delta h$.

[3] Although this constraint form encompasses commonly encountered constraints (rolling, skating, etc.), it is formalized and generalized in Section (3.2).

(iii) The curve $(\eta(t), \xi_v(t), \Gamma(t))$, where $\dot{\Gamma} = -\xi_h(t)\Gamma(t)$, satisfies the following constrained principle on $\mathfrak{h} \circledS \mathcal{V} \times W$. With the reduced constraints $\xi_v(t) = \theta(\Gamma(t))\xi_h(t)$ the following variational principle holds:

$$\delta \int l(\xi_h(t), \xi_v(t), \Gamma(t))dt = 0.$$

Variations along the curve take the form,

$$\begin{aligned}
\delta\xi_h &= \dot{\eta} + ad_{\xi_h}\eta, \\
\delta\Gamma &= -\eta\Gamma, \\
\delta\xi_v &= \frac{d}{dt}(\theta(\Gamma)\eta) + \xi_h\theta(\Gamma)\eta - \eta\theta(\Gamma)\xi_h,
\end{aligned}$$

where $\theta(\Gamma) : \mathfrak{h} \to \mathcal{V}$ and $\eta(t)$ is an independent variation vanishing at the endpoints.

Note that the reduced Lagrange-d'Alembert principle summarized above gives rise to Euler-Poincaré equations with additional forcing terms arising from the constraints. Unfortunately, these additional nonlinear terms often obstruct insight into the controllability of multibody dynamical systems. Our approach will utilize the reduced variational principle presented above, but express the resulting equations of motion in the framework of BKMM [45].

Schneider's reduction process has been used to study dynamic stabilization [43], local controllability [77], motion planning [78], and equilibria [29] of rolling systems similar to Moball. Although Schneider's approach achieves maximal reduction, a reconstruction equation that emphasizes and isolates the geometry underlying a multibody system's controllability and motion-planning was not developed.

3.2 Reduction & Reconstruction of Nonholonomic Mechanical Systems with Broken Symmetries

This section synthesizes the reduction method of Bloch et. al [45] with the use of advected parameters to yield reduction/reconstruction for nonholonomic mechanical systems with broken symmetries. Reduced equations are developed for systems with some common constraint forms and potential-energy dependencies. The most generic case is presented first, followed by special cases.

3.2.1 Generic Advected Parameter Reduction Theorem

Here reduction is developed for systems whose configuration spaces have the structure of a trivial principal bundle, $Q = G \times M$, where $G = H \circledS \mathcal{V}$ is a semidirect-

product space and H acts on $\mathcal{V}$ from the left. Smooth manifold M denotes the shape space. Advected parameters are assumed to be elements of the space $\mathcal{V}$, where H acts on $\mathcal{V}$ from the left[4]. Suppose that the constraints depend on an advected parameter a_0[5] as well as the group variables $y \in \mathcal{V}$. Similar to Subsection (3.1.6), nonholonomic constraints are assumed of the form,

$$\dot{y} = \dot{h}A(h, y, a_0, r) + B(h, y, a_0, r)\dot{r}, \tag{3.9}$$

where $\dot{q} = (h, \dot{h}, y, \dot{y}, r, \dot{r}) \in TQ$, $A(\cdot)$ is a $T\mathcal{V}$-valued function and $B(\cdot) : TM \to T\mathcal{V}$. This constraint distribution is assumed to have an invariance,

$$\pi\dot{y} = \pi\dot{h}A(\pi h\pi y, \pi a_0, r) + B(\pi h, \pi y, \pi a_0, r)\dot{r}, \quad \forall \pi \in H.$$

This invariance condition leads to reduced constraints of the form,

$$\xi_v = \xi_h A(\Pi, \Gamma, r) + B(\Pi, \Gamma, r)\dot{r}, \tag{3.10}$$

where $(\xi_h, \xi_v) = (h^{-1}\dot{h}, h^{-1}y) \in \mathfrak{h} \times \mathcal{V}$, and

$$\Gamma(t) \triangleq h^{-1}(t)a_0 \in \mathcal{V},$$
$$\Pi(t) = h^{-1}(t)y(t) \in \mathcal{V},$$

define a constant norm and variable norm advected parameter. Note that $\Pi(t)$ is simply the state variable y pulled back to the identity. Each advected parameter evolves according to its respective advection equation,

$$\dot{\Gamma} = -\xi_h\Gamma,$$
$$\dot{\Pi} = -\xi_h\Pi + \xi_h A(\Pi, \Gamma, r) + B(\Pi, \Gamma, r)\dot{r}.$$

The following theorem reduces the dynamics to the space $\mathfrak{h} \times \mathcal{V} \times TM$ and reconstructs the equations according to the geometric framework of [45].

Theorem 3.2.1. Consider the Lagrangian of a nonholonomic mechanical system (2.6.2) subject to the invariant constraints (3.9). Suppose that the Lagrangian's kinetic energy is cyclic in its $\mathcal{V}$-coordinate and can be expressed as a function of reduced variables: $l(\xi_h, \xi_v, \Pi, \Gamma, r, \dot{r})$. Letting $\{b_i\}$ denote a basis of the set $\mathcal{S}$, the equations of motion can be written as:

[4]Most of these results can be generalized to the slightly more general case where the advected parameter lies in space $\mathcal{P}$, with H having a left action on $\mathcal{P}$.

[5]This case can be extended to multiple advected parameters.

$$\begin{pmatrix}\xi_h\\ \xi_v\end{pmatrix} = \begin{pmatrix}-\mathbb{A}(\boldsymbol{z})\dot{r} + \mathbb{I}^{-1}(\boldsymbol{z})\vec{p}\\ \xi_h A(\boldsymbol{z}) + B(\boldsymbol{z})\dot{r}\end{pmatrix},$$

$$\dot{p}_i = \dot{r}\cdot\alpha_i(\boldsymbol{z})\dot{r} + \dot{r}\cdot\beta_i(\boldsymbol{z})\vec{p} + \vec{p}\cdot\gamma_i(\boldsymbol{z})\vec{p} + \left(\Gamma\times\frac{\partial V}{\partial\Gamma} + \left(\Pi - A(\boldsymbol{z})\right)\times\frac{\partial V}{\partial\Pi}\right)\cdot b_i^{\mathfrak{b}},$$

$$M(\boldsymbol{z})\ddot{r} = -C(\boldsymbol{z},\dot{r}) + N(\boldsymbol{z},\vec{p},\dot{r}) + \frac{\partial V}{\partial r} + B^T(\boldsymbol{z})\frac{\partial V}{\partial\Pi},$$

$$\dot{\Gamma} = -\xi_h\Gamma,$$

$$\dot{\Pi} = -\xi_h\Pi + \xi_h A(\boldsymbol{z}) + B(\boldsymbol{z})\dot{r},$$

where $\boldsymbol{z} \triangleq (\Pi,\Gamma,r)$ and $b_i^{\mathfrak{b}}$ denotes the $\mathfrak{b}$-component of b_i.

These equations have a similar structure to the reduced equations developed in BKMM [45], with a few notable differences. The equations are coupled through the advected parameters (Γ,Π), which have associated advection equations. The reconstruction equation remains linear in $\dot{r}$ and $\vec{p}$ and incorporates the reduced constraints. As in [45], the momentum differential equations are still quadratic in $\dot{r}$ and $\vec{p}$, but with additional forcing terms due to the dependence of the constraints and potential energy on (Γ,Π). Similar external forcing terms arise in the shape-space differential equations for the same reasons.

Assuming that the Lagrangian's kinetic energy is cyclic in its $\mathcal{V}$-coordinate is a mild assumption, as nearly all examples of interest share this feature. For many mechanical systems (2.6.2), Lagrangian dependencies on a_0 and $y \in \mathcal{V}$ occur within inner products, which allows the Lagrangian to be expressed in the reduced variables $l(\xi_h,\xi_v,\Pi,\Gamma,r,\dot{r})$. One may notice close similarities between the reduced constraints (3.10) and the advection equation for $\dot{\Pi}$. These equations are not redundant but constrain the augmented system to replicate the dynamics of the original Lagrangian. Lastly, note that much of the complexity in the additional forcing terms arise due to the generic nature of the constraints and potential energy; many realistic examples are much simpler (see Section 3.5).

3.2.2 Proof of Theorem 3.2.1

Below is a proof for Theorem 3.2.1, shown in detail as its construction forms the basis for the following theorems.

Proof of Theorem 3.2.1. The first step is to establish a reduced Lagrange-d'Alembert principle based on the assumed invariances of the constraint distribution and La-

grangian, similar to Theorem 3.1.3 and shown explicitly in [74, 82]. From these sources the following equivalence can be derived:

Theorem 3.2.2. For a Lagrangian defined over $Q = H \circledS \mathcal{V} \times M$ that is subject to the invariant constraints (3.9), and which can be expressed as a function of the reduced variables $l(\xi_h, \xi_v, \Pi, \Gamma, r, \dot{r})$, the following are equivalent:

1. The variational principle,

$$\delta \int L(h, \dot{h}, y, \dot{y}, r, \dot{r}, a_0) dt = 0$$

holds for a curve $(h(t), y(t), r(t)) \in G \times M$ satisfying the constraints with a_0 held constant. Variations $\delta h(t)$, $\delta y(t)$, $\delta r(t)$ vanish at the endpoints and,

$$\delta y(t) = \delta h(t) A(h, y, a_0, r) + B(h, y, a_0, r) \delta r.$$

2. The variational principle,

$$\delta \int l(\xi_h, \xi_v, \Pi, \Gamma, r, \dot{r}) dt = 0$$

holds for a curve $(\xi_h(t), \xi_v(t), \Pi(t), \Gamma(t), r(t))$ satisfying the reduced constraints (3.9). Variations take the form,

$$\begin{aligned}
\delta \xi_h &= \dot{\eta} + ad_{\xi_h} \eta, \\
\delta \Pi &= -\eta \Pi + \eta A(\Pi, \Gamma, r) + B(\Pi, \Gamma, r) \delta r, \\
\delta \xi_v &= -\eta \xi_v + \Big(\frac{d}{dt} + \xi_h \Big) \Big(\eta A(\Pi, \Gamma, r) + B(\Pi, \Gamma, r) \delta r \Big), \\
\delta \Gamma &= -\eta \Gamma,
\end{aligned}$$

where $\eta = h^{-1} \delta h$ and $(\eta, \delta r)$ vanish at the endpoints.

Equivalence of the integrands $L(h, \dot{h}, y, \dot{y}, r, \dot{r}, a_0)$ and $l(\xi_h, \xi_v, \Pi, \Gamma, r, \dot{r})$ follows by the assumption that the Lagrangian is expressible as $l(\xi_h, \xi_v, \Pi, \Gamma, r, \dot{r})$, and by using the definitions of the advected parameters (Γ, Π). Equivalence of the constraint distributions follows from the assumed invariance property and equivalence of the variations is computed explicitly in [74, 82]. Given the equivalence of the variational principles above, the following reduced variational principle holds,

$$\delta \Big(\int_a^b T(\xi_h, \xi_v, r, \dot{r}) dt - \int_a^b V(\boldsymbol{z}) dt \Big) = 0,$$

where $\boldsymbol{z} = (\Pi, \Gamma, r)$. From Corollary (2.6.1), this variational principle is equivalent to,

$$\delta \int_a^b T(\xi_h, \xi_v, r, \dot{r}) dt = \delta \int_a^b dV(\boldsymbol{z}) \cdot \delta q \; dt,$$

where $-dV(\boldsymbol{z})$ represents a conservative force arising from the potential energy. The kinetic energy can now be treated as a Φ_h-invariant system subject to external forcing, with additional variables (Γ, Π). The Φ_h-invariance permits the system's dynamics to be expressed according to the BKMM method.

Conservative Potential Force. The conservative force can be represented as a one-form $-dV(\boldsymbol{z})$, where

$$-dV(\boldsymbol{z}) = -\frac{\partial V}{\partial \Gamma} d\Gamma - \frac{\partial V}{\partial \Pi} d\Pi - \frac{\partial V}{\partial r} dr.$$

However, the action of $-dV(\boldsymbol{z})$ on vectors $\dot{\Gamma} \in \mathcal{V}$ and $\dot{\Pi} \in \mathcal{V}$ must obey the advection differential equations, which results in the equivalent one-form,

$$-dV(\boldsymbol{z}) = \Big(\Gamma \times \frac{\partial V}{\partial \Gamma} + \Big(\Pi - A(\boldsymbol{z})\Big) \times \frac{\partial V}{\partial \Pi}\Big) d\xi_h + \Big(B^T(\boldsymbol{z}) \frac{\partial V}{\partial \Pi} - \frac{\partial V}{\partial r}\Big) dr,$$

where $-dV(\boldsymbol{z})$ is invariant with respect to Φ_h from the invariance of $\boldsymbol{z}$. Ostrowski [65] showed that Φ_h-invariant forces are incorporated by projecting the forces along the allowable momenta directions (i.e., the basis of $\mathcal{S}$) and shape-space. We will use this fact below.

Reconstruction Equation. We first construct a basis for the set $\mathcal{S}$ where symmetry directions are determined by the kinetic energy only (since the potential has been incorporated as a conservative force). Let this basis be denoted by $\{\mathcal{B}_i(h, y, a_0, r)\}_{i=1}^k$. Pulling each vector back to the Lie algebra using a left-action yields a basis $\{b_i(\boldsymbol{z})\}_{i=1}^k$. If $b_i^{\mathfrak{h}}$ denotes the $\mathfrak{h}$-component of b_i, then the $\mathcal{V}$-component is dictated by the constraints (3.10), i.e., $b_i(\boldsymbol{z}) = (b_i^{\mathfrak{h}}, b_i^{\mathfrak{h}} A(\boldsymbol{z}))$ (actuator motions $\dot{r}$ are not contained in $\mathcal{S}$). Following Definition (3.1.8), the nonholonomic momenta are defined as follows:

$$p_i = \Big\langle \frac{\partial l}{\partial \kappa}, b_i(\boldsymbol{z}) \Big\rangle, \; \forall i \in [1, k],$$

where $\kappa \in \mathfrak{g}$ and $k = \dim(\mathfrak{h}) - \dim(\mathcal{S})$. Each of the above equalities can be expressed as one-forms acting on tangent vectors $v_q \in TQ$, which define motion along bases orthogonal to those of $\mathcal{S}$ [65]. Together, the kernels of each synthesized one-form add affine constraints, which when combined with the nonholonomic constraints, fully define motion on $\mathfrak{g}$. Concatenating these new constraints with the

nonholonomic constraints defines a connection on $\mathfrak{h} \times \mathcal{V}$, which can be written as:

$$\begin{pmatrix} \xi_h \\ \xi_v \end{pmatrix} = \begin{pmatrix} -\mathbb{A}(\boldsymbol{z})\dot{r} + \mathbb{I}^{-1}(\boldsymbol{z})\vec{p} \\ \xi_h A(\boldsymbol{z}) + B(\boldsymbol{z})\dot{r} \end{pmatrix}.$$

The reconstruction equation recovers the reduced constraints, expressed as a function of (Γ, Π) due to the dependencies of each $b_i(\boldsymbol{z})$.

Momentum Equation. Recall that Theorem 3.1.1 defines the time-derivative of the nonholonomic momenta in the absence of external forcing and was derived from a reduced variational principle. The set of basis vectors $\{b_i(\boldsymbol{z})\}_{i=1}^k$ define the directions along which the nonholonomic momenta act. Further, when the bases are pulled back to $\mathfrak{g}$ and depend on the shape-space variables r, then the following differential equations govern the nonholonomic momenta [45, 65],

$$\dot{p}_i = \Big\langle \frac{\partial l}{\partial \kappa}, [\kappa, b_i] + \langle \frac{\partial b_i}{\partial r}, \dot{r} \rangle \Big\rangle,$$

again where $\kappa \in \mathfrak{g}$ is an arbitrary Lie algebra element of the fiber. The right-hand side of the inner product describes how the basis vector $b_i(r)$ changes in time. To account for our basis' dependency on $\boldsymbol{z} = (\Pi, \Gamma, r)$, the partial derivative is converted to a full derivative, where we assume no explicit time-dependency. Writing $b_i(\boldsymbol{z}) = (b_i^\flat, b_i^\flat A(\boldsymbol{z})) \in \mathfrak{g} \times \mathcal{V}$ as above, the conservative force $-dV(\boldsymbol{z})$ is incorporated into the momentum differential equation,

$$\dot{p} = \Big\langle \frac{\partial l}{\partial \kappa}, [\kappa, b_i(\boldsymbol{z})] + \frac{d}{dt} b_i(\boldsymbol{z}) \Big\rangle + \Big(\Gamma \times \frac{\partial V}{\partial \Gamma} + \Big(\Pi - A(\boldsymbol{z}) \Big) \times \frac{\partial V}{\partial \Pi} \Big) \cdot b_i^\flat, \ \forall i \in [1, k].$$

Substituting the reconstruction eqaution into the above yields the quadratic form appearing in Theorem 3.2.1, although with a dependency on $\boldsymbol{z}$.

Shape Dynamics. Deriving the reduced shape dynamics differs superficially from the derivation found in [65]. A constrained Lagrange-d'Alembert principle is applied to the Lagrangian yielding the following,

$$\frac{d}{dt}\Big(\frac{\partial l_c}{\partial \dot{r}^i} \Big) - \frac{\partial l_c}{\partial r^i} = -ad^*_\kappa \frac{\partial l}{\partial \kappa} \mathbb{A}(\delta r^i) - \frac{\partial l}{\partial \kappa}(d\mathbb{A}(\dot{r}, \delta r^i) + \frac{\partial I^{-1} p}{\partial r^i} \Big),$$

where l_c denotes the constrained reduced Lagrangian, which is the reduced Lagrangian l with the reduced constraints substituted in for ξ_v, i.e.

$$l_c = l(\xi_h, \xi_h A(\Pi, \Gamma, r) + B(\Pi, \Gamma, r)\dot{r}, \Pi, \Gamma, r, \dot{r}),$$

and $\mathbb{A}(\cdot)$ denotes the nonholonomic connection introduced above. The quadratic base dynamics shown in Theorem 3.2.1 are obtained by substituting l_c and $\mathbb{A}(\cdot) \to \mathbb{A}(\boldsymbol{z})$. The reader is encouraged to see [65] for further detail. This completes the proof of Theorem 3.2.1. □

3.3 Constant-Norm Advected Parameter Dependency

Many systems of interest are characterized by simpler constraints and invariances than those presented in Theorem 3.2.1. Consider a system with configuration space $Q = H\circledS\mathbb{R}^3 \times M$, and whose Lagrangian is invariant with respect to the transformation,

$$(h_2, x) \cdot (h, \dot{h}, y, \dot{y}, r, \dot{r}) = (h_2 h, h_2 \dot{h}, h_2 y + x, h_2 \dot{y}, r, \dot{r}),\ (h_2, x) \in H\circledS\mathbb{R}^3. \quad (3.11)$$

In contrast to Theorem 3.2.1, the invariance condition (3.11) implies that the Lagrangian is cyclic in $y \in \mathcal{V}$. Assume that the potential $V(r, h^{-1}a_0) = V(r, \Gamma)$ is a function of a constant-norm advected parameter a_0, where $\Gamma \triangleq h^{-1}a_0$. Suppose that the constraint distribution $\mathcal{D}$ is defined by,

$$\dot{y} = \dot{h}A(h^{-1}a_0, r), \quad (3.12)$$

where $A(\cdot)$ is a smooth vector-valued function. These constraints are encountered for mechanical systems that roll, slide, or skate along flat planes (where a_0 is the direction of gravity in an inertial frame). Schneider's "Intermediate Theorem" [74] establishes a reduced Lagrange-d'Alembert principle over $\mathfrak{h} \times \mathcal{V}$ for this case. This reduction principle allows the dynamics to be expressed in the BKMM framework as follows.

Theorem 3.3.1. Under the invariance (3.11) and constraints (3.12), where $\{b_i\}$ is any basis of $\mathcal{S}$, the equations of motion can be expressed as follows:

$$\begin{aligned}
\begin{pmatrix} \xi_h \\ \xi_v \end{pmatrix} &= \begin{pmatrix} -\mathbb{A}(z)\dot{r} + \mathbb{I}^{-1}(z)\vec{p} \\ \xi_h A(z) \end{pmatrix} \\
\dot{p}_i &= \dot{r} \cdot \alpha_i(z)\dot{r} + \dot{r} \cdot \beta_i(z)\vec{p} + \vec{p} \cdot \gamma_i(z)\vec{p} + \left(\Gamma \times \frac{\partial V}{\partial \Gamma}\right) \cdot b_i^{\mathfrak{h}}, \\
M(z)\ddot{r} &= -C(z, \dot{r}) + N(z, \dot{r}, \vec{p}) + \frac{\partial V}{\partial r}, \\
\dot{\Gamma} &= -\xi_h \Gamma,
\end{aligned}$$

where $z = (r, \Gamma)$ and $b_i^{\mathfrak{h}}$ denotes the $\mathfrak{h}$-component of b_i.

Having invoked the "Intermediate Theorem" from [74], the proof for these equations follows identically to Theorem 3.2.1 and will be omitted here. Note that these equations are identical to Theorem 3.2.1 with simpler additional forcing terms in the momentum and shape-space differential equations. An example of these equations in use can be found in the rolling, actuated disk presented in Section (3.5).

3.4 Position Dependency in the Potential

A nonholonomic mechanical system that travels over undulating terrains cannot be reduced with the reduction principles used in Theorem 3.3.1 due to a dependency on position, $y \in \mathcal{V}$, in the potential energy. Again suppose a constraint distribution defined by (3.12), where a_0 is an advected parameter (that represents the surface normal for rolling vehicles on undulating terrain). Where $\Gamma \triangleq g^{-1}a_0$ and $\Pi \triangleq g^{-1}y$, the following theorem reduces to $\mathfrak{h} \times \mathcal{V} \times TM$, similar to Theorem 3.2.1.

Theorem 3.4.1. Consider a nonholonomic mechanical system subject to constraints (3.12) with a potential energy dependent on the $\mathcal{V}$-coordinate, i.e., $V(y)$. Suppose that the Lagrangian can be expressed in the reduced variables $l(\xi_h, \xi_v, \Pi, \Gamma, r, \dot{r})$. Letting $\{b_i\}$ denote any basis of $\mathcal{S}$, the equations of motion can be expressed as follows:

$$\begin{aligned}
\begin{pmatrix} \xi_h \\ \xi_v \end{pmatrix} &= \begin{pmatrix} -\mathbb{A}(z)\dot{r} + \mathbb{I}^{-1}(z)\vec{p} \\ \xi_h A(\Gamma) \end{pmatrix} \\
\dot{p}_i &= \dot{r} \cdot \alpha_i(z)\dot{r} + \dot{r} \cdot \beta_i(z)\vec{p} + \vec{p} \cdot \gamma_i(z)\vec{p} + \left(\Gamma \times \frac{\partial V}{\partial \Gamma} + \left(\Pi - A(z)\right) \times \frac{\partial V}{\partial \Pi}\right) \cdot b_i^{\mathfrak{h}}, \\
M(z)\ddot{r} &= -C(z, \dot{r}) + N(z, \dot{r}, \vec{p}) + \frac{\partial V}{\partial r}, \\
\dot{\Gamma} &= -\xi_h \Gamma, \\
\dot{\Pi} &= -\xi_h (\Pi - A(z)),
\end{aligned}$$

where $z = (r, \Gamma)$ and $b_i^{\mathfrak{h}}$ denotes the $\mathfrak{h}$-component of b_i.

The proof of this theorem follows from the proof of Theorem 3.2.1. Note that when the constraints are not a function of internal actuation $\dot{r}$, the additional forcing term affecting the shape space is simpler. Furthermore, when the constraints are not a function of y, the equations are only coupled through the advected parameter Γ, rather than through both (Γ, Π).

3.5 Examples of Reduction

The dynamics of the BallBot [47] and an actuated rolling-falling disk are analyzed in this section. Each system features a potential energy with a dependence on the direction of gravity, which breaks the $SO(3)$ symmetry that would otherwise be possessed by these systems.

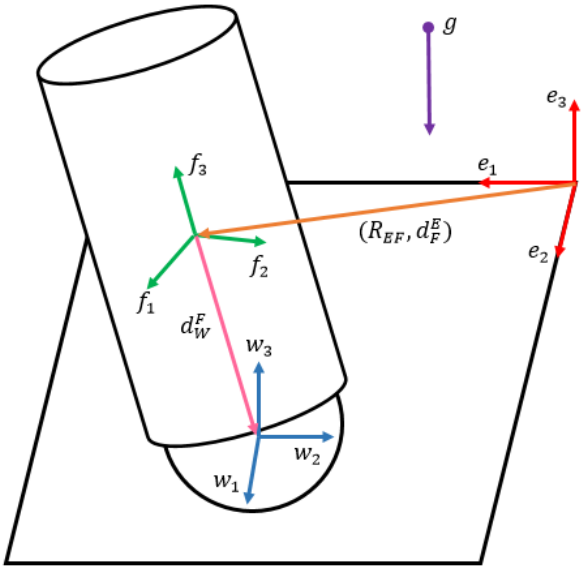

Figure 3.1: BallBot Rolling on a Flat Plane.

3.5.1 BallBot

Consider a homogeneous sphere rolling on a flat plane with frame $W = \{w_1, w_2, w_3\}$ fixed to the center of rotation (Fig. 3.1). A homogeneous cylinder sits atop the sphere with frame $F = \{f_1, f_2, f_3\}$ fixed to the center of mass. Frame $E = \{e_1, e_2, e_3\}$ is fixed to the plane. This system well approximates the BallBot [47].

Let $(R_{EF}, d_F^E) \in SE(3)$ describe the position and orientation of the cylinder, where d_F^E is a vector extending from frame E's origin to F's origin. The BallBot is actuated by controlling the orientation of the sphere. Thus, the shape space is chosen to correspond to the state of the fully-actuated sphere, $(r, \dot{r}) = (R_{FW}(\vartheta), \omega_F^W)$, expressed from frame F. Let $(\dot{d}^b, \omega^b)$ denote the body velocities of the cylinder. Let (M_s, M_c, M_T) denote the sphere, cylinder, and total system masses respectively. Further, let J correspond to the homogeneous sphere's moment of inertia, (I_1, I_2) to the principal moments of the cylinder where I_1 is the moment about f_1 and f_2, and let Θ correspond to the net moment of inertia of the system about F. Then, the reduced Lagrangian can be written as,

$$l(\dot{d}^b, \omega^b, \omega_F^W, e_3) = \frac{1}{2} \begin{bmatrix} \dot{d}^b \\ \omega^b \\ \omega_F^W \end{bmatrix}^T \begin{bmatrix} M_T & -M_s \hat{d}_W^F & 0 \\ M_s \hat{d}_F^W & \Theta & J \\ 0 & J & J \end{bmatrix} \begin{bmatrix} \dot{d}^b \\ \omega^b \\ \omega_F^W \end{bmatrix} + M_c g (R_{EF} d_W^F) \cdot e_3,$$

where the map $\widehat{(\cdot)}$ takes vectors in $\mathbb{R}^3$ to 3×3 skew-symmetric matrices. The Lagrangian is invariant with respect to $SO(2) \times \mathbb{R}^3$ (the position variable d^b is cyclic),

where $SO(2)$ is the isotropy subgroup of e_3. A natural choice for the advected parameter is the e_3 axis (opposite the direction of gravity) viewed from the body frame:

$$\Gamma \triangleq R_{EF}^T e_3.$$

The sphere is assumed to role on a plane without slip, leading to constraints

$$\dot{d}_W^E = r\hat{\omega}_W^E e_3,$$

where $\dot{d}_W^E$ and ω_W^E denote the translational and rotational velocities of the sphere, as viewed in frame E. Noting that $\dot{d}_W^E = \dot{d}_F^E + \dot{R}_{EF} d_W^F$, the constraints are written in the form $\dot{y} = \dot{h}A(h,y,a_0,r) + B(h,y,a_0,r)\dot{r}$, as in Theorem 3.2.1, which can be reduced by R_{EF} to obtain:

$$\dot{d}^b = -r\hat{\Gamma}\dot{\vartheta} + \hat{d}_W^F \omega^b. \tag{3.13}$$

The constraints (3.13) share the invariance principle in Theorem 3.2.1 and the reduced Lagrangian can be expressed as a function $l(\dot{d}^b, \omega^b, \omega_F^W, \Gamma)$. Noting that $d_F^W = -lf_3$ where f_3 is a standard basis vector along the third dimension, the basis vectors for the reduced constraint distribution are:

$$\mathcal{D} = \text{span}\left\{ \begin{bmatrix} -r\hat{\Gamma} f_3 \\ 0_{3\times 1} \\ f_3 \end{bmatrix}, \begin{bmatrix} -r\hat{\Gamma} f_2 \\ 0_{3\times 1} \\ f_2 \end{bmatrix}, \begin{bmatrix} -r\hat{\Gamma} f_1 \\ 0_{3\times 1} \\ f_1 \end{bmatrix}, \begin{bmatrix} 0_{3\times 1} \\ f_3 \\ 0_{3\times 1} \end{bmatrix}, \begin{bmatrix} lf_1 \\ f_2 \\ 0_{3\times 1} \end{bmatrix}, \begin{bmatrix} -lf_2 \\ f_1 \\ 0_{3\times 1} \end{bmatrix} \right\}.$$

Note that the first three basis vectors of $\mathcal{D}$ correspond to rotations of the actuated sphere, with the cylinder held fixed relative to the sphere, and the corresponding translations that arise from the no-slip constraints. The last three basis vectors of $\mathcal{D}$ correspond to rotations of the cylinder about the actuated sphere, with the actuated sphere held fixed, and the corresponding translations of the frame F as it rotates about the actuated sphere. From this basis set, one can extract basis vectors satisfying the constraints and along the symmetry directions of the kinetic energy:

$$\mathcal{S} = \text{span}\left\{ \begin{bmatrix} 0_{3\times 1} \\ f_3 \\ 0_{3\times 1} \end{bmatrix}, \begin{bmatrix} lf_1 \\ f_2 \\ 0_{3\times 1} \end{bmatrix}, \begin{bmatrix} -lf_2 \\ f_1 \\ 0_{3\times 1} \end{bmatrix} \right\}.$$

The reconstruction equation can be constructed from the procedure demonstrated in the proof of Theorem 3.2.1:

$$\begin{pmatrix} \omega^b \\ \dot{d}^b \end{pmatrix} = \begin{pmatrix} -\mathbb{A}(\Gamma)\dot{\vartheta} + \mathbb{I}^{-1}\vec{p} \\ -r\hat{\Gamma}\dot{\vartheta} + \hat{d}^F_W \omega^b \end{pmatrix},$$

where,

$$\mathbb{A}(\Gamma) = \begin{bmatrix} \frac{(J+M_c r l \Gamma_3)}{J+I_1+l^2 M_c} & 0 & -\frac{M_c r l \Gamma_1}{J+I_1+l^2 M_c} \\ 0 & \frac{(J+M_c r l \Gamma_3)}{J+I_1+l^2 M_c} & -\frac{M_c r l \Gamma_2}{J+I_1+l^2 M_c} \\ 0 & 0 & \frac{J}{J+I_2} \end{bmatrix},$$

$$\mathbb{I}^{-1} = \begin{bmatrix} (J+I_1+l^2 M_c)^{-1} & 0 & 0 \\ 0 & (J+I_1+l^2 M_c)^{-1} & 0 \\ 0 & 0 & (J+I_2)^{-1} \end{bmatrix}.$$

Recall that the BallBot's potential energy is $V = -M_c g (R_{EF} d^F_W) \cdot e_3$. After introducing the advected parameter, the potential energy can be written $V(\Gamma) = M_c g l f_3 \cdot \Gamma$. Following the proof of Theorem 3.2.1, the gravitational force can be computed from the negated differential of the potential, $-dV = -M_c g l f_3 d\Gamma$. The advection equation $\dot{\Gamma} = \hat{\Gamma}\omega^b$ constrains $\dot{\Gamma}$ such that,

$$\langle -dV, \dot{\Gamma} \rangle = \langle M_c g l \hat{\Gamma} f_3, \omega^b \rangle.$$

Thus, the gravitational potential produces a torque that can be expressed by the one-form $M_c g l \hat{\Gamma} f_3 d\omega^b$. Gravity manifests itself as a torque about the physical connection between the sphere and the cylinder, given by $T_g = l f_3 \times (-M_c g \Gamma)$, which is recovered from this one-form. Using the basis vectors of $\mathcal{S}$ and the procedure contained in the proof of Theorem 3.2.1, the following nonholonomic momenta equations can be derived:

$$\begin{aligned} \dot{p}_1 &= M_c l (\dot{d}^b_x \omega^b_z - \dot{d}^b_z \omega^b_x) + (I_1 - I_2)\omega^b_y \omega^b_z + J(\dot{\vartheta}_2 \omega^b_z - \dot{\vartheta}_3 \omega^b_y) + M_c g l \Gamma_2, \\ \dot{p}_2 &= M_c l (\dot{d}^b_y \omega^b_z - \dot{d}^b_z \omega^b_y) - (I_1 - I_2)\omega^b_x \omega^b_z + J(\dot{\vartheta}_3 \omega^b_x - \dot{\vartheta}_1 \omega^b_z) - M_c g l \Gamma_1, \\ \dot{p}_3 &= M_s l (\dot{d}^b_x \omega^b_x + \dot{d}^b_y \omega^b_y) + J(\dot{\vartheta}_1 \omega^b_y - \dot{\vartheta}_2 \omega^b_x). \end{aligned}$$

The quadratic form shown in Theorem 3.2.1 can be realized by substituting for $\dot{d}^b$ and ω^b using the reconstruction equation. With the actuated shape space,

$$\ddot{\vartheta} = \vec{u},$$

and the advection differential equation $\dot{\Gamma} = \hat{\Gamma}\omega^b$, the system's dynamics are complete.

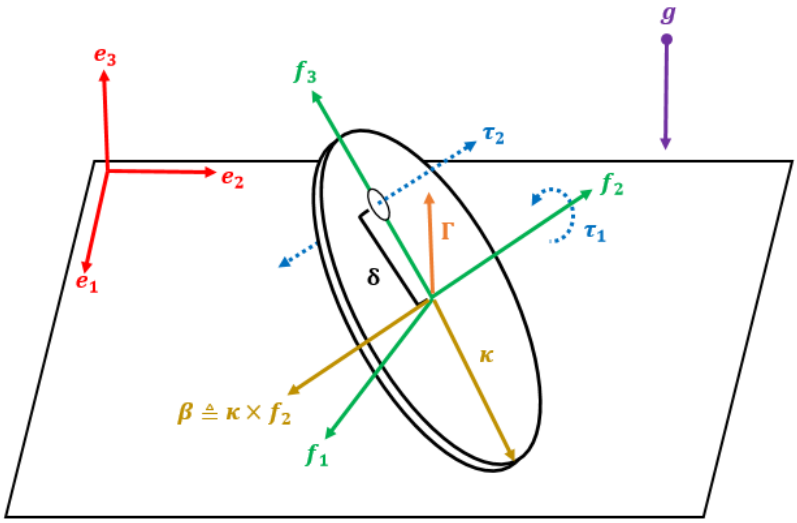

Figure 3.2: Actuated Rolling-Falling Disk.

3.5.2 Actuated Rolling-Falling Disk

Consider a thin disk rolling on a flat plane with frame $F = \{f_1, f_2, f_3\}$ attached to the center of rotation and frame E denoting a fixed spatial frame (Fig. 3.2). The principal moment about f_1 and f_3 is given by J_1 and the principal moment about f_2 is J_2. The disk mass is given by M_d and r is the disk radius. Rotation matrix R_{EF} describes the orientation of F with respect to the inertial frame. A bidirectional thruster with thrust value $\tau_2 \in \mathbb{R}$ acts parallel to f_2 and is located a distance δ along the f_3 axis. Furthermore, a torque $\tau_1 \in \mathbb{R}$ acts about f_2.

It is more natural to describe the dynamics of this sytem with respect to a moving frame D defined by basis vectors $\{f_2, \kappa, \beta\}$, where κ is a unit vector pointing from the disk's center to the contact point and $\beta \triangleq \kappa \times f_2$. Rotational and translational velocities expressed with respect to D will be denoted by $\omega^b = \{\omega_2^b, \omega_k^b, \omega_\beta^b\}$ and by $\dot{d}^b = \{\dot{d}_2^b, \dot{d}_\kappa^b, \dot{d}_\beta^b\}$. Expressed in this moving frame, the reduced Lagrangian can be written as:

$$l(\dot{d}^b, \omega^b, e_3) = \frac{1}{2} M_d ||\dot{d}^b||^2 + \frac{1}{2}\Big(J_1\Big((\omega_\kappa^b)^2 + (\omega_\beta^b)^2\Big) + J_2(\omega_2^b)^2\Big) - M_d g r ||f_2 \times R_{EF}^T e_3||.$$

The Lagrangian is invariant with respect to $SO(2)\times\mathbb{R}^3$, where $SO(2)$ corresponds to rotations about e_3. This invariance motivates an advected vector $\Gamma \triangleq R^T e_3$, which corresponds to the fixed e_3 axis viewed with respect to frame D. The corresponding advection equation is given by $\dot{\Gamma} = \hat{\Gamma}\omega^b$. The disk's no-slip rolling constraints take

the form:

$$\dot{d}^b = r\hat{\kappa}\omega^b = r\beta\omega_2^b - rf_2\omega_\beta^b.$$

The vectors that satisfy the constraints and lay along symmetry directions of the kinetic energy are,

$$X_2 = \begin{pmatrix} r\beta \\ f_2 \end{pmatrix},\ X_\kappa = \begin{pmatrix} 0 \\ \kappa \end{pmatrix},\ X_\beta = \begin{pmatrix} -rf_2 \\ \beta \end{pmatrix},$$

where the first component denotes translational velocity followed by rotational velocity. Using these vectors, the reconstruction equation (excluding the constraints) can be written as[6]:

$$\begin{pmatrix} \omega_2^b \\ \omega_\kappa^b \\ \omega_\beta^b \end{pmatrix} = \begin{pmatrix} \frac{1}{J_2+r^2M_d} & 0 & 0 \\ 0 & \frac{1}{J_1} & 0 \\ 0 & 0 & \frac{1}{J_1+r^2M_d} \end{pmatrix} \begin{pmatrix} p_2 \\ p_\kappa \\ p_\beta \end{pmatrix}.$$

The gravitational potential can be expressed as $V(\Gamma) = M_d g r ||\hat{f}_2\Gamma||$, after introducing the advected parameter Γ. The advection differential equation $\dot{\Gamma} = \hat{\Gamma}\omega^b$ constrains $\dot{\Gamma}$ such that,

$$\langle -dV, \dot{\Gamma} \rangle = \left\langle \frac{M_d g r}{\sqrt{\Gamma_1^2 + \Gamma_3^2}} \begin{pmatrix} \Gamma_2\Gamma_3 \\ 0 \\ -\Gamma_1\Gamma_2 \end{pmatrix}, \omega^b \right\rangle,$$

and hence the gravitational torque can be expressed with respect to a body frame as,

$$T_g = \frac{M_d g r}{\sqrt{\Gamma_1^2 + \Gamma_3^2}} \begin{pmatrix} \Gamma_2\Gamma_3 \\ 0 \\ -\Gamma_1\Gamma_2 \end{pmatrix}.$$

Geometrically, Γ and the unit vector κ are related via $\kappa_1 = \frac{-\Gamma_1}{\sqrt{\Gamma_1^2+\Gamma_3^2}}$ and $\kappa_3 = \frac{-\Gamma_3}{\sqrt{\Gamma_1^2+\Gamma_3^2}}$. Using this result, the gravity torques projected along the κ, β, and f_2 directions are:

$$\begin{pmatrix} T_{g,2} & T_{g,\kappa} & T_{g,\beta} \end{pmatrix} = \begin{pmatrix} 0 & 0 & M_d g r \Gamma_2 \end{pmatrix}.$$

[6]Note: There is no shape space in this example

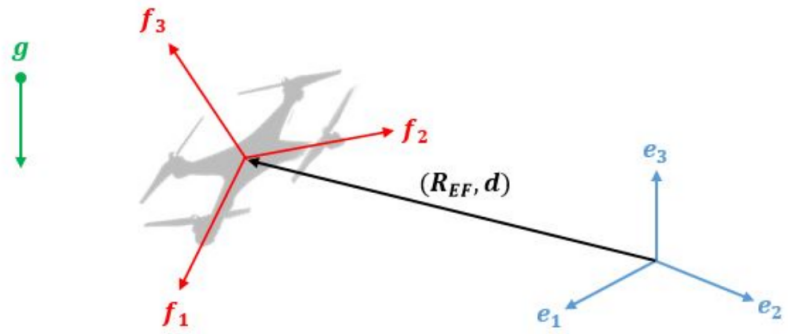

Figure 3.3: Basic Frame Definitions for Multirotor Vehicles.

Using the procedure outlined in the proof of Theorem 3.2.1 and the basis vectors $\{X_2, X_\kappa, X_\beta\}$, the nonholonomic momentum differential equations can be written as:

$$\begin{aligned}
\dot{p}_2 &= r^2 M_d \omega_\beta^b \omega_\kappa^b + \tau_1, \\
\dot{p}_\kappa &= \omega_2^b \left(p_\beta - r^2 M_d \omega_\beta^b \right) - \kappa_1 \delta \tau_2, \\
\dot{p}_\beta &= -\omega_2^b \left(p_\kappa + r^2 M_d \omega_\kappa^b \right) + M_d g r \Gamma_2 + \tau_2 (\kappa_3 \delta - 1).
\end{aligned}$$

Substituting in the reconstruction equation and the identities for κ_1 and κ_3 yields:

$$\begin{aligned}
\dot{p}_2 &= \frac{p_\beta p_\kappa r^2 M_d}{J_1 (J_1 + r^2 M_d)} + \tau_1, \\
\dot{p}_\kappa &= \frac{p_2 p_\beta J_1}{(J_1 + r^2 M_d)(J_2 + r^2 M_d)} + \delta \tau_2 \cdot \frac{\Gamma_1}{\sqrt{\Gamma_1^2 + \Gamma_3^2}}, \\
\dot{p}_\beta &= -\frac{p_2 p_\kappa (J_1 + r^2 M_d)}{J_1 (J_2 + r^2 M_d)} + M_d g r \Gamma_2 - \tau_2 \cdot \frac{\Gamma_3 \delta + \sqrt{\Gamma_1^2 + \Gamma_3^2}}{\sqrt{\Gamma_1^2 + \Gamma_3^2}}.
\end{aligned}$$

Since there is no shape space and thus no shape space dynamics for this example, the nonholonomic momenta, reconstruction equation, and advection equation $\dot{\Gamma} = \hat{\Gamma} \omega^b$ fully define the disk's motion under the influence of control forces τ_1 and τ_2.

3.5.3 Multirotor Vehicles

As an example illustrating the generality of the reduction/reconstruction approach, the dynamics of a multirotor vehicle (see Fig. 3.3) will now be derived in the framework of [45]. Similar to the previous examples, the potential energy of this system is nontrivial and a dependency on gravity prevents full $SO(3)$ reduction. An interesting characteristic of this example is the lack of nonholonomic constraints.

As before, let $E = \{e_1, e_2, e_3\}$ and $F = \{f_1, f_2, f_3\}$ denote an inertial and body-fixed frame, respectively where (R_{EF}, d) relates the orientation of position of frame F with respect to E. Let the body-frame be affixed to the vehicle's center of mass and assume that the f_1-f_2 plane is orthogonal each rotor's axis of rotation[7], i.e. each rotor spins about the f_3 axis. The Lagrangian of the multirotor vehicle will now be derived from first principles.

Let the mass and inertia of all fixed components on the vehicle be denoted by (M_s, I_s), respectively. To forgo modeling the orientation of each rotor (the rotor's angle is not as important as its speed), each rotor is modelled as a homogeneous thin cylinder of mass and inertia (M_r, I_r), respectively, where J is the principal moment about the rotation axis. Each of n total rotors are assumed to be identical. To obtain the kinetic energy of an individual rotor, let (G_i, σ_i) denote the orientation and location of a frame fixed to the center of the i^{th} rotor (modelled as a cylinder) with respect to F. Then, the position of an arbitrary mass element on the i^{th} cylinder is given by,

$$x^s_{r,i} = d + R_{EF}\sigma_i + R_{EF}G_i r,$$

where r is a vector extending to an arbitrary mass element in frame G_i. The kinetic energy of the i^{th} rotor is then,

$$\begin{aligned} T_{r_i} &= \frac{1}{2}\int_V \rho ||\dot{d} + \dot{R}_{EF}\sigma_i + \dot{R}_{EF}G_i r + R_{EF}\dot{G}_i r||^2 dV, \\ &= \underbrace{\frac{1}{2}\int_V \rho ||\dot{d} + \dot{R}_{EF}\sigma_i||^2 dV}_{\text{translational KE}} + \underbrace{\frac{1}{2}\int_V \rho ||\dot{R}_{EF}G_i r + R_{EF}\dot{G}_i r||^2 dV}_{\text{rotational KE}} \\ &+ \underbrace{\int_V \rho \langle \dot{d} + \dot{R}_{EF}\sigma_i, \dot{R}_{EF}G_i r + R_{EF}\dot{G}_i r\rangle dV}_{\emptyset}, \end{aligned}$$

where ρ and V are the density and volume of the cylinder. The third term in this expression is zero as a result of the fact that $\int_V \rho r dV = 0$, which follows since the frame G_i is placed at the cylinder's center of mass. Then, the kinetic energy of the rotor can be written as,

$$T^t_{r_i} = \frac{1}{2}\int_V \rho ||\dot{d}^b + \hat{\omega}^b \sigma_i||^2 dV,$$

[7] These assumptions can easily be relaxed, leading only to more cumbersome notation.

where $\dot{d}^b = R_{EF}^T \dot{d}$. Expanding this term and using the fact that $M_r = \int_V \rho dV$ yields,

$$T_{r_i}^t = \frac{1}{2} \begin{bmatrix} \dot{d}^b \\ \omega^b \\ \varpi_i \end{bmatrix}^T \begin{bmatrix} M_r & -M_r \hat{\sigma}_i & 0 \\ -M_r \hat{\sigma}_i & -M_r \hat{\sigma}^2 & 0 \\ 0 & 0 & 0 \end{bmatrix} \begin{bmatrix} \dot{d}^b \\ \omega^b \\ \varpi_i \end{bmatrix},$$

where ϖ_i is the angular velocity of the i^{th} rotor. Similarly, using the properties of skew-symmetric matrices and the identity $-\int_V \rho \hat{r}^2 dV = I_r$, the rotational kinetic energy of the i^{th} rotor can be expressed,

$$T_{r_i}^r = \frac{1}{2} \begin{bmatrix} \dot{d}^b \\ \omega^b \\ \varpi_i \end{bmatrix}^T \begin{bmatrix} 0 & 0 & 0 \\ 0 & I_r & J e_3 \\ 0 & J e_3^T & J \end{bmatrix} \begin{bmatrix} \dot{d}^b \\ \omega^b \\ \varpi_i \end{bmatrix}.$$

Now, define $\Theta \triangleq \begin{bmatrix} \sigma_1 & \sigma_2 & \dots & \sigma_n \end{bmatrix}$ as the rotor placement matrix, which contains as columns the positions to the center of each rotor with respect to frame F. Then, including the kinetic energy of the vehicle's body yields the total kinetic energy,

$$T = \frac{1}{2} \begin{bmatrix} \dot{d}^b \\ \omega^b \\ \varpi \end{bmatrix}^T \begin{bmatrix} M_T & -M_r \widehat{\Theta \mathbf{1}} & 0 \\ M_r \widehat{\Theta \mathbf{1}} & \Phi & J e_3 \mathbf{1}^T \\ 0 & J \mathbf{1} e_3^T & J \end{bmatrix} \begin{bmatrix} \dot{d}^b \\ \omega^b \\ \varpi \end{bmatrix},$$

where $\varpi = \{\varpi_i\}_{i=1}^n$, $\mathbf{1} = \{1\}_{i=1}^n$, the total mass is given by $M_T = M_s + n M_r$ and,

$$\Phi = I_s + n I_r - M_r \sum_{i=1}^{n} \hat{\sigma}_i^2,$$

is the net rotational inertia (which is constant). To write the potential energy, introduce two advected parameters $\gamma \triangleq R_{EF}^T e_3$ and $\xi \triangleq R_{EF}^T d$, satisfying advection differential equations,

$$\dot{\gamma} = \hat{\gamma} \omega^b,$$
$$\dot{\xi} = \hat{\xi} \omega^b + \dot{d}^b.$$

The advection parameters γ and ξ are simply the inertial z-axis, and the vector extending from frame E to F, viewed in a body frame. Then, the potential can be written as $V(\gamma, \xi) = g M_T \langle \gamma, \xi \rangle + M_r g \langle \gamma, \Theta \mathbf{1} \rangle$, and the resulting conservative force is given by,

$$-dV = \underbrace{-g M_T \gamma \cdot d(\dot{d}^b)}_{\text{force of gravity}} + \underbrace{M_r g \hat{\gamma} \Theta \mathbf{1} \cdot d(\omega^b)}_{\text{torque of gravity}}.$$

Note that the torque due to gravity arises due to asymmetrical placement of the rotors about the frame F, i.e. if the rotors are arranged in a classical symmetric

quadrotor layout then $\Theta\mathbf{1} = \emptyset$ and gravity will not impose a torque about F. Finally the Lagrangian can be written in the variables $L(\dot{d}^b, \omega^b, \varpi, \gamma, \xi)$ as,

$$L = \frac{1}{2}\begin{bmatrix} \dot{d}^b \\ \omega^b \\ \varpi \end{bmatrix}^T \begin{bmatrix} M_T & -M_r\widehat{\Theta\mathbf{1}} & 0 \\ M_r\widehat{\Theta\mathbf{1}} & \Phi & Je_3\mathbf{1}^T \\ 0 & J\mathbf{1}e_3^T & J \end{bmatrix} \begin{bmatrix} \dot{d}^b \\ \omega^b \\ \varpi \end{bmatrix} - gM_T\langle\gamma, \xi\rangle - M_r g\langle\gamma, \Theta\mathbf{1}\rangle \,. \quad (3.14)$$

The kinetic energy is a pure function of body velocities $(\dot{d}^b, \omega^b, \varpi)$, and as such it is invariant with respect to constant transformation of $SE(3)$. Since the constraint distribution is unrestrictive, i.e. $\mathcal{D}(q) = T_qQ$, the vectors that span the space $\mathcal{S}$ can be chosen to be any convenient basis that spans $\mathfrak{se}(3)$[8]. For our purposes it will be most convenient to choose the standard basis vectors $e_i \in \mathbb{R}^6$. Following the procedure outlined in the proof of Theorem 3.2.1, the reconstruction equation can be written as,

$$\begin{bmatrix} \dot{d}^b \\ \omega^b \end{bmatrix} = \begin{bmatrix} M_r\widehat{\Theta\mathbf{1}} & \Phi \\ M_T & -M_r\widehat{\Theta\mathbf{1}} \end{bmatrix}^{-1} \left(\begin{bmatrix} \vec{l} \\ \vec{p} \end{bmatrix} - \begin{bmatrix} J\langle\mathbf{1}, \varpi\rangle e_3 \\ 0_{3\times 1} \end{bmatrix} \right),$$

where $\vec{l}$ are the nonholonomic angular momenta and $\vec{p}$ are the nonholonomic linear momenta. Note that the term $J\langle\mathbf{1}, \varpi\rangle e_3$ is a reaction moment due to the cumulative rotation of the rotors, i.e. in a stable hover, when each rotor spins at the same speed in alternating directions, this term vanishes. The momentum differential equations are given by,

$$\begin{aligned} \dot{\vec{l}} &= \vec{p} \times \dot{d}^b + \vec{l} \times \omega^b + M_r g\gamma \times \Theta\mathbf{1}, \\ \dot{\vec{p}} &= \vec{p} \times \omega^b - gM_T\gamma. \end{aligned}$$

When the vehicle is designed such that $\Theta\mathbf{1} \equiv 0$, the equations of motion simplify considerably to,

$$\begin{aligned} \begin{bmatrix} \dot{d}^b \\ \omega^b \end{bmatrix} &= \begin{bmatrix} \frac{1}{M_T}\vec{p} \\ \Phi^{-1}(\vec{l} - J\langle\mathbf{1}, \varpi\rangle e_3) \end{bmatrix}, \\ \dot{\vec{l}} &= \vec{l} \times \Phi^{-1}(\vec{l} - J\langle\mathbf{1}, \varpi\rangle e_3\rangle, \\ \dot{\vec{p}} &= \vec{p} \times \Phi^{-1}(\vec{l} - J\langle\mathbf{1}, \varpi\rangle e_3) - gM_T\vec{\gamma} \end{aligned}$$

Of course, the above only incorporates the conservative forces due to gravity–the nonconservative actuator forces must now be included. Following a standard con-

[8] In all of the examples contained in this work, it is typically easier to choose the basis of $\mathcal{S}$ in the Lie algebra.

vention [52], the thrust due to the sum of the spinning rotors can be modeled by

$$F_a = \Big(c_T \sum_{i=1}^{n} \varpi_i^2\Big) e_3,$$

where c_T is a lumped parameter depending on the air density, rotor disk area, rotor radius and profile. Similarly, the torques imparted on the vehicle via the rotors can be modelled,

$$\tau_a = \sum_{i=1}^{n} \varpi_i^2 \Big(\sigma_i \times c_T e_3 - \phi_i c_Q e_3\Big),$$

where $\phi_i \in \{-1, 1\}$ denotes the direction of rotor i's rotation, and c_Q is a lumped parameter that describes the degree of resistive torque due to each spinning rotor. Following Ostrowski [66], these actuator forces can be projected along the momentum directions in which they act, and since the symmetry directions are a simple basis of $\mathfrak{se}(3)$, the momentum equations simply become,

$$\dot{\vec{l}} = \vec{l} \times \Phi^{-1}(\vec{l} - J\langle \mathbf{1}, \varpi \rangle e_3 \rangle + \sum_{i=1}^{n} \varpi_i^2 \Big(\sigma_i \times c_T e_3 - \phi_i c_Q e_3\Big),$$

$$\dot{\vec{p}} = \vec{p} \times \Phi^{-1}(\vec{l} - J\langle \mathbf{1}, \varpi \rangle e_3) - g M_T \vec{\gamma} + \Big(c_T \sum_{i=1}^{n} \varpi_i^2\Big) e_3,$$

for the vehicle modeled as $\Theta \mathbf{1} \equiv 0$. And, of course, the advection equation

$$\dot{\gamma} = \gamma \times \Phi^{-1}(\vec{l} - J\langle \mathbf{1}, \varpi \rangle e_3),$$

must be simultaneously satisfied. This completes the dynamics of a generic multirotor vehicle. These dynamics are equivalent to the standard quadrotor dynamics [52], except that the equations are written in body coordinates and in most works the reaction torques from spinning the rotors (i.e. including the term $J\langle \mathbf{1}, \varpi \rangle e_3$ in the reconstruction equation) are neglected. However, the reconstruction equation emphasizes the momenta, $\vec{l}$ and $\vec{p}$, which may play an important role in acrobatic flight maneuvers, and this formulation is easily generalizable to more complex multirotor systems (e.g. quadrotors with articulated arms for manipulation, etc.).

This chapter introduced a method to derive the reduced equations of motion for nonholonomic dynamical systems with broken symmetries, based on a synthesis of advected parameters and the reconstruction process of BKMM [45]. The equations of motion were presented for a variety of commonly-encountered constraint distributions and potential energy forms. To illustrate the generality of the approach, several examples were detailed including the BallBot, a rolling-falling disk, and a multirotor vehicle.

Chapter 4

CONTROLLABILITY OF SPHERICAL ROBOTS

Controllability of spherical robots on complex terrains must be rigorously understood before these vehicles can be confidently deployed. However, a thorough investigation of controllability on arbitrary smooth terrains has yet to be completed. This chapter provides a general, but surprisingly simple, approach to the analysis of small time local controllability (STLC). Broadly speaking, a dynamic system is small time locally controllable at a given state if feasible inputs exist that enable the system to move in a neighborhood about the initial state, in finite time. The simplicity of the controllability test developed in this chapter is enabled by the use of geometric mechanics, introduced in Chapter 3. A reconstruction equation is derived, which describes the role of momenta and internal actuation in generating inertial motions of the body. Importantly, the reconstruction equation exposes the steering matrix, which is a mathematical structure that is present for all rolling spherical robots. STLC conditions are then derived from a direct inspection of the steering matrix and are applicable to a wide class of spherical robots.

Local controllability conditions are well-established for spherical robots rolling on flat planes. In [28, 77, 78], Lagrangian reduction and symmetric products are used to derive the equations of motion and dynamic controllability results for various spherical vehicles. Stabilizability and STLC results are derived in [43, 58] for a rotor-controlled sphere as well. Local controllability of a sphere rolling on smooth terrains has been considered at the kinematic level in [50, 53]. Controllability results for spherical vehicles with constant potential energy can be found in [45].

4.1 Mathematical Preliminaries

Before introducing STLC conditions for generic spherical robots, the controllability of dynamical systems with drift and the differential geometry of surfaces will be briefly reviewed.

4.1.1 Controllability of Dynamical Systems with Drift

Consider an n-dimensional mechanical system evolving on a configuration space Q, with state $q \in Q$. The equations of motion can almost always be written in

control-affine form:

$$\dot{q} = f_0(q) + \sum_{i=1}^{m} h_i(q)u_i, \tag{4.1}$$

where $\{u_1, \ldots, u_m\}$ are the control inputs, $f_0(q)$ is the drift vector field, and $\{h_i(q)\}_{i=1}^m$ are control vector fields.

Definition 4.1.1 (Reachable Set [14])**.** The reachable set $\mathcal{R}^V(q_0, T)$ contains points that can be reached from starting configuration q_0 by any trajectory satisfying (4.1), at time T, for feasible controls, and which remain in some local neighborhood V. Let $\mathcal{R}^V(q_0, \leq T)$ denote points reachable in time up to and including T.

Definition 4.1.2 (Small-Time Locally Accessible (STLA))**.** System (4.1) is small-time locally accessible (STLA) from q_0 if $\dim(\mathcal{R}^V(q_0, \leq T)) = n$ for all neighborhoods V and times $T > 0$.

Definition 4.1.3 (Small-Time Locally Controllable (STLC))**.** System (4.1) is small-time locally controllable (STLC) if each reachable set $\mathcal{R}^V(q_0, \leq T)$ contains a neighborhood about q_0 for all neighborhoods V and times $T > 0$.

The STLA property implies that the system can maneuver in some n-dimensional subset of Q but not necessarily in any direction surrounding q_0, whereas STLC enables system (4.1) to maneuver locally in any direction about q_0 with feasible controls. Recall the matrix Lie bracket introduced in Chapter 2. For two vector fields $f_1(q), f_2(q) \in \mathcal{X}(Q)$, the Lie bracket can be similarly defined by,

$$[f_1(q), f_2(q)] = \frac{\partial f_2(q)}{\partial q} f_1(q) - \frac{\partial f_1(q)}{\partial q} f_2(q).$$

Physically, the Lie bracket $[f_1(q), f_2(q)]$ measures how the vector field $f_2(q)$ changes along the flow induced by $f_1(q)$. Lie brackets can be iterated to form Lie brackets of a higher degree, where the degree of a Lie bracket denotes the number of vector fields present, e.g. $[[f_1, f_2], f_1]$ is a Lie bracket of the third degree [24].

Definition 4.1.4 (Good & Bad Lie Brackets [24])**.** For a control-affine system (4.1), a bad Lie bracket is any iterated Lie bracket in which the drift field, $f_0(q)$, appears an odd number of times and each control field present, $f_i(q)$, appears an even number of times. Any Lie bracket that is not bad is good.

Definition 4.1.5 (Lie Algebra of Vector Fields)**.** The Lie algebra of vector fields $\{f_0(q), f_1(q), \ldots, f_m(q)\} \in \mathcal{X}(Q)$ is the span of all possible iterated Lie brackets of the $f_i(q)$ and is denoted by $\overline{\text{Lie}}(\{f_0, \ldots, f_m\})(q)$.

Theorem 4.1.1 (Lie Algebra Rank Condition (LARC) [17])**.** The Lie algebra rank condition (LARC) establishes that system (4.1) is STLA at q_0 if and only if,

$$\overline{\text{Lie}}(\{f_0, h_1, \ldots, h_m\})(q) = T_{q_0}Q.$$

For systems without drift, the LARC is sufficient to establish both STLA and STLC, which are equivalent in that case. For systems with drift, Sussmann's condition can be used.

Theorem 4.1.2 (Sussmann's Condition [81])**.** System (4.1) is STLC at an equilibrium point when the LARC is satisfied by good Lie brackets of degree k and each bad Lie bracket of degree $j \leq k$ can be written as a linear sum of good Lie brackets of degree less than j.

The following STLC theorems will require identifying good Lie brackets from the drift and control vector fields of the spherical robot's dynamics.

4.1.2 Differential Geometry of Surfaces

Terrain will be modeled as a regular surface S, which implies the existence of a local chart (U, φ) at each point in S, where $\varphi(u,v) : U \to S \subset \mathbb{R}^3$ is a homeomorphism and $U \subset \mathbb{R}^2$. A normalized Gauss map is defined by basis vectors $\{\frac{\varphi_u}{||\varphi_u||}, \frac{\varphi_v}{||\varphi_v||}, n\}$, where subscripts denote partial differentiation and $n(u,v) \triangleq \varphi_u/||\varphi_u|| \times \varphi_v/||\varphi_v||$ denotes the surface normal. The Gauss map provides a local frame at each point in S, and for regular surfaces, a chart can be found such that the Gauss frame is orthogonal [19]. A surface's properties can locally be described by its metric tensor, $M(u,v)$, curvature tensor, $K(u,v)$, and torsion form, $T(u,v)$,

$$\begin{aligned} M(u,v) &= \begin{bmatrix} ||\varphi_u|| & 0 \\ 0 & ||\varphi_v|| \end{bmatrix}, \\ K(u,v) &= \begin{bmatrix} \frac{\langle \varphi_u, n_u \rangle}{||\varphi_u||^2} & \frac{\langle \varphi_u, n_v \rangle}{||\varphi_u|| \cdot ||\varphi_v||} \\ \frac{\langle \varphi_v, n_u \rangle}{||\varphi_u|| \cdot ||\varphi_v||} & \frac{\langle \varphi_v, n_v \rangle}{||\varphi_v||^2} \end{bmatrix}, \\ T(u,v) &= \begin{bmatrix} \frac{\langle \varphi_v, \varphi_{vv} \rangle}{||\varphi_u||^2 \cdot ||\varphi_v||} & \frac{\langle \varphi_v, \varphi_{uv} \rangle}{||\varphi_v||^2 \cdot ||\varphi_u||} \end{bmatrix}, \end{aligned} \tag{4.2}$$

which can be used to describe how the Gauss frame changes with time [59]. Imagine a time-parameterized path on S that corresponds to a path in (u,v)-space via $\varphi(\cdot)^{-1}$. A Gauss frame is defined for each point on the path. The normalized Gauss

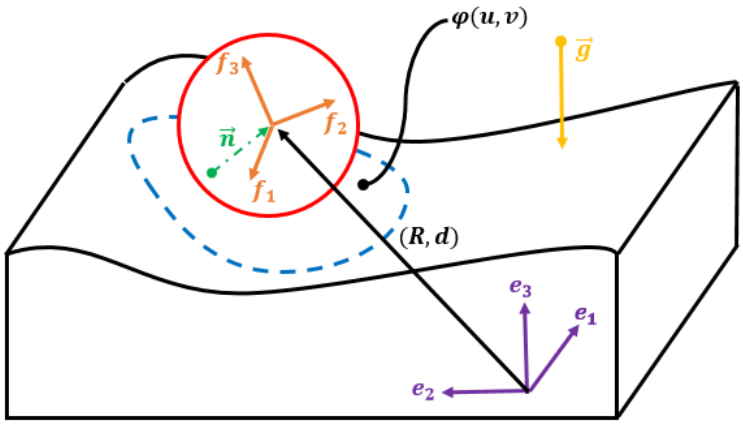

Figure 4.1: Model of a Generic Spherical Robot on Generic Terrain.

Symbol	Description
$E = \{e_1, e_2, e_3\}$	Inertial frame.
$F = \{f_1, f_2, f_3\}$	Body frame fixed to sphere's COR.
(R, d^s)	Rotation/displacement between E and F, expressed in E.
$(\omega^s, \dot{d}^s)$	Angular/linear velocities expressed in E.
$(\omega^b, \dot{d}^b)$	Angular/linear velocities expressed in F.
r_b	Sphere radius
M_T	Total mass
$(r, \dot{r}) \in \mathbb{R}^{2m}$	Generic internal actuators, e.g. the state of an internal pendulum or the states of MoBall's internal magnets.

Table 4.1: Generic Spherical Vehicle Parameters.

frame's angular velocity along this path, when viewed in the inertial frame E, is given by,

$$\omega_G^s = -\frac{\varphi_u}{||\varphi_u||}\left\langle KM\begin{pmatrix}\dot{u}\\ \dot{v}\end{pmatrix}, e_2\right\rangle + \frac{\varphi_v}{||\varphi_v||}\left\langle KM\begin{pmatrix}\dot{u}\\ \dot{v}\end{pmatrix}, e_1\right\rangle + n \cdot TM\begin{pmatrix}\dot{u}\\ \dot{v}\end{pmatrix}, \tag{4.3}$$

where e_i is a standard basis vector in $\mathbb{R}^2$.

A surface's principal curvatures are the values of the maximum and minimum normal curvatures among all paths passing through a point $p \in S$. Without loss of generality, let $|\kappa_1| \geq |\kappa_2|$. In this work, it is assumed that the surface satisfies the following constraint:

$$|\kappa_1| < \frac{1}{r_b}, \tag{4.4}$$

where r_b is the radius of the spherical vehicle. This surface constraint ensures that a unique contact point exists between the robot and the surface at all times.

4.2 Dynamics & Controllability of Spherical Vehicles

The dynamics of a generic spherical robot will now be derived on flat, sloped, and arbitrary smooth terrain using the reduction/reconstruction procedure in Chapter 3. The equations of motion will then be written in control-affine form in preparation for invoking Sussmann's STLC condition. Consider a generic spherical robot rolling on a smooth surface (see Fig. 4.1 and Table 4.1 for parameters). Expressing the system velocities as the tuple $\dot{q} = (\dot{d}^b, \omega^b, \dot{r}) \in TQ$ leads to a Lagrangian,

$$L(q,\dot{q}) = \frac{1}{2}\dot{q}^T \mathcal{M}_b \dot{q} - V(q), \text{ where } \mathcal{M}_b = \begin{bmatrix} m_{11} & \hat{m}_{12} & m_{13} \\ -\hat{m}_{12} & m_{22} & m_{23} \\ m_{13}^T & m_{23}^T & m_{33} \end{bmatrix} \in \mathbb{R}^{(6+m)\times(6+m)},$$

and where $V(q)$ represents a potential energy that is assumed to be derived from a potential field. The $m_{11} = M_T \cdot I$ entry of matrix $\mathcal{M}_b$ encodes the total system mass, $\hat{m}_{12} \neq 0$ when the COM is noncollocated with the COR, and $m_{22}(r)$ represents the effective moment of inertia of the sphere and its internal actuators. The entries (m_{13}, m_{23}) depend on the actuator configuration and m_{33} expresses the actuators' inertial properties.

No-slip and no-spin conditions constrain the ball's motion. Physically, the no-slip condition mandates that "skidding" is not allowed. The no-spin constraint prohibits rotations of the sphere about the terrain's surface normal, i.e. spinning in place is prohibited. These constraints are physically reasonable with sufficient contact friction, which is often provided by the robot's weight and the terrain's surface texture. The no-spin and no-slip constraints define the constraint distribution $\mathcal{D} \subset TQ$, which contains all allowable velocities that satisfy these constraints. The constraint distribution is given by,

$$\mathcal{D}(q) = \{(\dot{d}^b, \omega^b, \dot{r}) \mid \dot{d}^b = r_b \hat{\omega}^b R^T n(t),\ \langle \omega^b, R^T n(t) \rangle = 0\}, \tag{4.5}$$

where $n(t)$ is the surface normal expressed in an inertial frame and $\langle \cdot, \cdot \rangle$ denotes the standard inner product.

4.2.1 Dynamics on a Flat Plane

When the terrain is flat, the vehicle is constrainted by (4.5) and gravity acts opposite of the surface normal, $n(t) = e_3$. Let $\{e_1, e_2, e_3\}$ denote the standard basis for $\mathbb{R}^3$ and $\{e_i\}_{i=1}^m$ the standard basis for $\mathbb{R}^m$. Introduce the following advected parameters:

$$\alpha \triangleq R^T e_1,\ \beta \triangleq R^T e_2,\ \gamma \triangleq R^T e_3, \tag{4.6}$$

where $R \in SO(3)$ denotes the orientation of the sphere. Variables (α, β, γ) track the basis vectors of the inertial frame E with respect to the body frame F, and satisfy the following advection equations,

$$\dot{\alpha} = \hat{\alpha}\omega^b,\ \dot{\beta} = \hat{\beta}\omega^b,\ \dot{\gamma} = \hat{\gamma}\omega^b.$$

Consider spherical vehicles whose potential energy is dependent on the vector e_3 via inner products, which includes all BSR vehicles[1]. An augmented dynamical system is formed by including (α, β, γ) as additional states in the Lagrangian and constraints, e.g. the following variable substitutions are made to the no-slip constraints and potential,

$$\dot{d}^b \propto \hat{\omega}^b R^T e_3 \rightarrow \dot{d}^b \propto \hat{\omega}^b \gamma,$$
$$V(q) \propto \langle d^s, e_3 \rangle \rightarrow V(q) \propto \langle d^b, \gamma \rangle.$$

The rotation group $SO(3)$ acts on (α, β, γ) from the left. By introducing γ as an additional state, and the assumption that the advected parameter appears in $V(q)$ through inner products, the augmented Lagrangian system satisfies the invariant condition (3.1.4) with respect to $SO(3)$. Furthermore, the vehicle's position, d^b, is cyclic for all spherical robots rolling on the plane. Thus, the augmented system is now invariant with respect to $SE(3)$. Introducing γ is alone sufficient to achieve $SE(3)$-invariance (since γ models the gravity vector), whereas advected parameters (α, β) will be convenient when considering undulating terrain. With velocities described in local coordinates as $\dot{q} = (\dot{d}^b, \omega^b, \dot{r})$, the directions of motion that satisfy the no-slip rolling constraints are given by:

$$X_\alpha = \begin{pmatrix} -r_b\beta^T & \alpha^T & 0_{1\times m} \end{pmatrix}^T,\ X_\beta = \begin{pmatrix} r_b\alpha^T & \beta^T & 0_{1\times m} \end{pmatrix}^T. \tag{4.7}$$

The vectors (4.7) form a basis for the constraint distribution (4.5). Physically, the vector fields (X_α, X_β) correspond to angular velocities tangent to the plane and the translational velocities that result from the no-slip constraints. Having defined an augmented system that satisfies the invariance condition (3.1.4) with respect to $SE(3)$, it is now possible to decompose the equations of motion geometrically, as

[1] This assumption includes rotor-actuated spherical vehicles and more general potential energy dependencies can be easily generalized

in equations (3.3)-(3.5). From (3.1.8), the nonholonomic momenta are defined by,

$$\begin{aligned} p_\alpha \triangleq& \langle \mathcal{M}_b X_\alpha, v_q \rangle \\ =& (-r_b m_{11}\beta + \hat{m}_{12}\alpha)\cdot \dot{d}^b + (r_b \hat{m}_{12}\beta + m_{22}\alpha)\cdot \omega^b + (-r_b m_{13}^T\beta + m_{23}^T\alpha)\cdot \dot{r}, \\ p_\beta \triangleq& \langle \mathcal{M}_b X_\beta, v_q \rangle \\ =& (r_b m_{11}\alpha + \hat{m}_{12}\beta)\cdot \dot{d}^b + (-r_b \hat{m}_{12}\alpha + m_{22}\beta)\cdot \omega^b + (r_b m_{13}^T\alpha + m_{23}^T\beta)\cdot \dot{r}, \end{aligned} \tag{4.8}$$

where $v_q = (\dot{d}^b, \omega^b, \dot{r}) \in T_eQ$ is an arbitrary velocity. The nonholonomic momenta represent the combination of the angular and linear momenta along the directions defining X_α and X_β. Equation (4.8) can be treated as a constraint on T_eQ, which by construction is independent from the kinematic constraints [45]. Concatenating the constraints (4.5) and (4.8) into a single equation yields,

$$\begin{bmatrix} I & -r_b\hat{\gamma} \\ -r_b\beta^T m_{11} - \alpha^T \hat{m}_{12} & -r_b\beta^T \hat{m}_{12} + \alpha^T m_{22} \\ r_b\alpha^T m_{11} - \beta^T \hat{m}_{12} & r_b\alpha^T \hat{m}_{12} + \beta^T m_{22} \\ 0 & \gamma^T \end{bmatrix} \begin{pmatrix} \dot{d}^b \\ \omega^b \end{pmatrix} + \begin{bmatrix} 0 \\ -r_b\beta^T m_{13} + \alpha^T m_{23} \\ r_b\alpha^T m_{13} + \beta^T m_{23} \\ 0 \end{bmatrix} \dot{r} = \begin{bmatrix} 0 \\ p_\alpha \\ p_\beta \\ 0 \end{bmatrix}, \tag{4.9}$$

where the first and last equations impose the no-slip/no-spin constraints and the middle equations are the nonholonomic momenta (4.8). These constraints fully define motion on the Lie group G. Equation (4.9) is equivalent to the reconstruction equation (3.3) and can be written as,

$$\begin{pmatrix} \omega_\alpha^b \\ \omega_\beta^b \end{pmatrix} = \mathbb{A}(\alpha,\beta,\gamma,r)\dot{r} + \mathbb{I}^{-1}(\alpha,\beta,\gamma,r)\vec{p}, \tag{4.10}$$

where $(\omega_\alpha^b, \omega_\beta^b)$ denote the α and β components of ω^b,

$$\mathbb{I}^{-1}(\alpha,\beta,\gamma,r) \triangleq \frac{1}{\det(\mathbb{I})} \begin{bmatrix} r_b^2 m_{11} - 2r_b\langle m_{12},\gamma\rangle + \langle \beta, m_{22}\beta\rangle & -\langle \alpha, m_{22}\beta\rangle \\ -\langle \alpha, m_{22}\beta\rangle & r_b^2 m_{11} - 2r_b\langle m_{12},\gamma\rangle + \langle \alpha, m_{22}\alpha\rangle \end{bmatrix}$$

denotes the constrained locked inertia tensor, and

$$\mathbb{A}(\alpha,\beta,\gamma,r) \triangleq \mathbb{I}^{-1}(\alpha,\beta,\gamma,r) \begin{bmatrix} r_b\beta^T m_{13} - \alpha^T m_{23} \\ -r_b\alpha^T m_{13} - \beta^T m_{23} \end{bmatrix}$$

denotes the nonholonomic connection. $\mathbb{A}(\alpha,\beta,\gamma,r)$ maps actuator velocities to body velocities, while $\mathbb{I}^{-1}(\alpha,\beta,\gamma,r)$ maps nonholonomic momenta to body velocities. As an inertia tensor, $\mathbb{I}(\alpha,\beta,\gamma,r)$ is always invertible and thus $\det(\mathbb{I}) > 0$. Generating inertial motions from the actuator velocities is dependent on the rank of the following matrix,

Definition 4.2.1 (Steering Matrix)**.** The matrix,

$$\mathbb{B}(\alpha,\beta,\gamma,r) \triangleq \begin{bmatrix} r_b\beta^T m_{13} - \alpha^T m_{23} \\ -r_b\alpha^T m_{13} - \beta^T m_{23} \end{bmatrix},$$

is called the steering matrix.

The steering matrix maps actuator velocities to nonholonomic momenta. The entries m_{13} and m_{23} map actuator velocities to linear and angular momenta, respectively, and both generally depend on the internal structure of the vehicle (e.g. the locations of actuators within the robot). If the matrices m_{13} and m_{23} were both null, then actuator velocities would not be kinematically related to angular velocities $(\omega^b_\alpha, \omega^b_\beta)$ via the reconstruction equation. Thus, one can see that $\mathbb{B}(\alpha,\beta,\gamma,r)$ represents the ability to instantaneously generate inertial motion through actuator velocities. The steering matrix will play an important role in the controllability conditions that follow.

The nonholonomic momentum differential equations (3.4) can be derived from a Lagrange-d'Alembert principle [45] and take the following form,

$$\dot{p}_i = \left\langle \frac{\partial L}{\partial \xi}, [\xi, X_i] + \frac{d}{dt} X_i \right\rangle + \tau(V), \tag{4.11}$$

where $i = (\alpha,\beta)$, $\xi = (\dot{d}^b, \omega^b) \in \mathfrak{se}(3)$ is a body-velocity, $[\cdot,\cdot]$ is the Lie bracket, and $\tau(V)$ is an external force arising from gravity. For a generic spherical robot with a Lagrangian and constraints as described above, the nonholonomic momenta differential equations can be expressed as,

$$\begin{aligned} \dot{p}_\alpha &= r_b\omega^b_\alpha(\omega^b_\beta\langle m_{12},\alpha\rangle - \omega^b_\alpha\langle m_{12},\beta\rangle + \langle\gamma, m_{13}\dot{r}\rangle) + \hat{\gamma}V_\gamma\cdot\alpha, \\ \dot{p}_\beta &= r_b\omega^b_\beta(\omega^b_\beta\langle m_{12},\alpha\rangle - \omega^b_\alpha\langle m_{12},\beta\rangle + \langle\gamma, m_{13}\dot{r}\rangle) + \hat{\gamma}V_\gamma\cdot\beta, \end{aligned} \tag{4.12}$$

where $V_\gamma = \partial V/\partial\gamma$. The dynamical equations governing the internal actuators $\ddot{r}$ can be obtained using a standard reduced Euler-Lagrange approach. But for controllability calculations, which are the focus of this chapter, it is assumed that $\ddot{r}$ is directly controlled, i.e. $\ddot{r} = u$.

Notice that (α,β,γ) define columns of the rotation matrix R^T, which relates vectors in the world frame to their body frame equivalents. Thus, the differential equations for (α,β,γ) can be expressed as,

$$\dot{R}^T = -\hat{\omega}^b R^T = -\omega^b_\alpha R^T\hat{e}_1 - \omega^b_\beta R^T\hat{e}_2. \tag{4.13}$$

Equations (4.10)-(4.13), in addition to $\ddot{r} = u$ and the constraints (4.5), fully determine motion on $SO(3) \times \mathbb{R}^2 \times \mathbb{R}^m$ for any spherical robot rolling on flat terrain without slip and spin about the normal to the plane.

4.2.2 STLC on Flat Planes

Although STLC conditions for actuated spheres on flat planes have previously been derived [28, 77, 78], conditions derived using the framework of Section 4.2 are reviewed, as this forms the basis for our novel analysis of STLC on undulating terrain. Before expressing the dynamics in control-affine form, a physically-motivated coordinate change is made. Changing coordinates from $(p_\alpha, p_\beta) \to (\tilde{p}_\alpha, \tilde{p}_\beta)$ via,

$$\begin{pmatrix} \tilde{p}_\alpha \\ \tilde{p}_\beta \end{pmatrix} = \begin{pmatrix} p_\alpha \\ p_\beta \end{pmatrix} + \mathbb{B}(\alpha, \beta, \gamma, r)\dot{r}, \tag{4.14}$$

converts the nonholonomic momenta to the total angular momenta along coordinates defined by (X_α, X_β). This coordinate change is a natural choice for these problems since the control inputs directly affect the total moments $(\dot{\tilde{p}}_\alpha, \dot{\tilde{p}}_\beta)$. The mass matrix terms m_{13} and m_{23} from the Lagrangian are assumed to be time-invariant, which is reasonable for many practical examples (rotor-actuated, Moball, etc.) and can easily be generalized[2]. Applying the coordinate change (4.14) leads to new momentum differential equations,

$$\begin{pmatrix} \dot{\tilde{p}}_\alpha \\ \dot{\tilde{p}}_\beta \end{pmatrix} = \begin{pmatrix} r_b \omega^b_\alpha (\omega^b_\beta \langle m_{12}, \alpha \rangle - \omega^b_\alpha \langle m_{12}, \beta \rangle) + \hat{\gamma} V_\gamma \cdot \alpha - \omega^b_\beta \langle \gamma, m_{23} \dot{r} \rangle \\ r_b \omega^b_\beta (\omega^b_\beta \langle m_{12}, \alpha \rangle - \omega^b_\alpha \langle m_{12}, \beta \rangle) + \hat{\gamma} V_\gamma \cdot \beta + \omega^b_\alpha \langle \gamma, m_{23} \dot{r} \rangle \end{pmatrix} + \mathbb{B}(R, r)\ddot{r}, \tag{4.15}$$

and a simplified reconstruction equation,

$$\omega^b_{\alpha\beta} = \mathbb{I}^{-1}(R, r)\tilde{p}. \tag{4.16}$$

The advected variables (α, β, γ) were introduced to enable full $SE(3)$-reduction. However, it is clear that $(R, \alpha, \beta, \gamma)$ is a redundant set of variables since (α, β, γ) define R^T. Let the state be $z = (d^b, \tilde{p}_\alpha, \tilde{p}_\beta, r, \dot{r}, R)$ with control inputs $u_i = \ddot{r}$. Then, the dynamical system for a generic spherical robot can be expressed in control-

[2]For example, if m_{13} and m_{23} are dependent on the shape variables r, then an additional term quadratic in $\dot{r}$ would appear in equation (4.15) and would be carried through the forthcoming bracket calculations.

affine form (4.1) where,

$$f(z) = \begin{bmatrix} -r_b R^T e_2 \omega_\alpha^b + r_b R^T e_1 \omega_\beta^b \\ r_b \omega_\alpha^b (\omega_\beta^b \langle Rm_{12}, e_1\rangle - \omega_\alpha^b \langle Rm_{12}, e_2\rangle) + \langle \hat{e}_3 R V_\gamma, e_1\rangle - \omega_\beta^b \langle Rm_{23}\dot{r}, e_3\rangle \\ r_b \omega_\beta^b (\omega_\beta^b \langle Rm_{12}, e_1\rangle - \omega_\alpha^b \langle Rm_{12}, e_2\rangle) + \langle \hat{e}_3 R V_\gamma, e_2\rangle + \omega_\alpha^b \langle Rm_{23}\dot{r}, e_3\rangle \\ \dot{r} \\ 0_{m\times 1} \\ \omega_\alpha^b \hat{e}_1 R + \omega_\beta^b \hat{e}_2 R \end{bmatrix}, \tag{4.17}$$

is the drift vector field and,

$$h_i(z) = \begin{bmatrix} 0_{3\times 1} & \mathbb{B}(R,r)e_i & 0_{m\times 1} & e_i & 0_{3\times 3} \end{bmatrix}^T, \forall i = 1, \dots m, \tag{4.18}$$

are the control vector fields where e_i is a standard basis vector of $\mathbb{R}^m$. Equilibrium points occur when the ball is at rest $(\omega_\alpha^b, \omega_\beta^b, \tilde{p}_\alpha, \tilde{p}_\beta) = 0$ and when the internal actuators cancel torques due to gravity, i.e. $\hat{\gamma} V_\gamma \cdot \alpha = 0$ and $\hat{\gamma} V_\gamma \cdot \beta = 0$. Denoting an equilibrium state z^*, an application of the LARC yields the following theorem about spherical robot accessibility.

Theorem 4.2.1 (LARC, Flat Terrain)**.** At equilibrium point z^* of the control affine system (4.17)-(4.18) with inputs $u = \ddot{r}$, if the steering matrix $\mathbb{B}(R,r)$ is surjective and $\dim(r) \geq 2$ then the system (4.17)-(4.18) is STLA.

Proof of Theorem 4.2.1. Upon evaluation at the equilibrium point z^*, the Lie bracket $[f(z), h_i(z)]$ is given by

$$[f(z), h_i(z)]|_{z=z^*} = \begin{bmatrix} r_b \langle e_1, \mathbb{A} e_i\rangle R^T e_2 - r_b \langle e_2, \mathbb{A} e_i\rangle R^T e_1 \\ 0_{2\times 1} \\ -e_i \\ 0_{n\times 1} \\ -\langle e_1, \mathbb{A} e_i\rangle \hat{e}_1 R - \langle e_2, \mathbb{A} e_i\rangle \hat{e}_2 R \end{bmatrix}.$$

Clearly, $\{h_i(z), [f(z), h_i(z)]\}$ spans the input space $(r, \dot{r})$. Further, if $\mathbb{B}(R,r)$ is surjective, then the nonholonomic connection $\mathbb{A}(\cdot)$ is full-rank, which implies that the above first-order bracket spans two DOF along the $\dot{d}^b$ coordinate and two DOF along $T_q SO(3)$. In addition, $\mathbb{B}(R,r)$ being surjective implies that $h_i(z)$ spans the momenta space. To complete the proof, all that remains is to find proper brackets to span the third rotational DOF, which is obtained by the fourth-degree bracket

$[[[f(z), h_i(z)], f(z)], h_j(z)]$. Evaluated at the equilibrium point z^*, where $(\star)$ denotes a possible nonzero entry that does not affect the analysis, the $T_qSO(3)$ coordinate of the fourth degree Lie bracket $[[[f(z), h_i(z)], f(z)], h_j(z)]|_{z=z^*}$ is given by,

$$(\star)\hat{e}_1 R + (\star)\hat{e}_2 R + \Big(\langle e_1, \mathbb{A}e_j\rangle\langle e_2, \mathbb{A}e_j\rangle - \langle e_2, \mathbb{A}e_j\rangle\langle e_1, \mathbb{A}e_i\rangle\Big)\hat{e}_3 R.$$

The scalar multiplying the $\hat{e}_3 R$ term is the $(i,j)^{th}$ component of matrix,

$$\mathbb{A}^T(e_2 e_1^T - e_1 e_2^T)\mathbb{A}. \tag{4.19}$$

Since the nonholonomic connection $\mathbb{A}(R,r)$ has full row-rank, $\mathbb{A}^T e_1$ and $\mathbb{A}^T e_2$ are linearly independent. From this, one can show that the matrix (4.19) must have at least one nonzero off-diagonal entry, which will then span the remaining third DOF of $T_qSO(3)$. □

Theorem 4.2.1 establishes LARC for the control-affine system (4.17)-(4.18) using Lie brackets up to the fourth degree. From Sussmann's condition, STLC can be established at equilibrium points of this dynamical system if the LARC is satisfied by good Lie brackets up to the fourth degree and each bad Lie bracket of degree $j \leq 4$ can be written as a linear sum of good Lie brackets of degree less than j.

Theorem 4.2.2 (STLC, Flat Terrain)**.** The good Lie brackets from Theorem 4.2.1 ensure STLC from an equilibrium point z^* provided that $\mathbb{B}(R,r)$ is surjective and $\dim(r) \geq 2$.

Proof of Theorem 4.2.2. From the proof of Theorem 4.2.1, good Lie brackets up to the fourth degree were used to demonstrate STLA. To prove STLC, Sussmann's condition requires that any bad bracket of degree $j \leq 4$ must be expressible as a linear combination of good Lie brackets of degree $k < j$. The only bad bracket to consider is the third-order bracket, $[[f(z), h_i(z)], h_i(z)]$. Evaluated at the equilibrium point z^*, this Lie bracket is written as:

$$[[f(z), h_i(z)], h_i(z)]|_{z=z^*} = \begin{bmatrix} \star \\ \star \\ \star \\ \star \\ 0_{m\times 1} \\ 0_{3\times 3} \end{bmatrix},$$

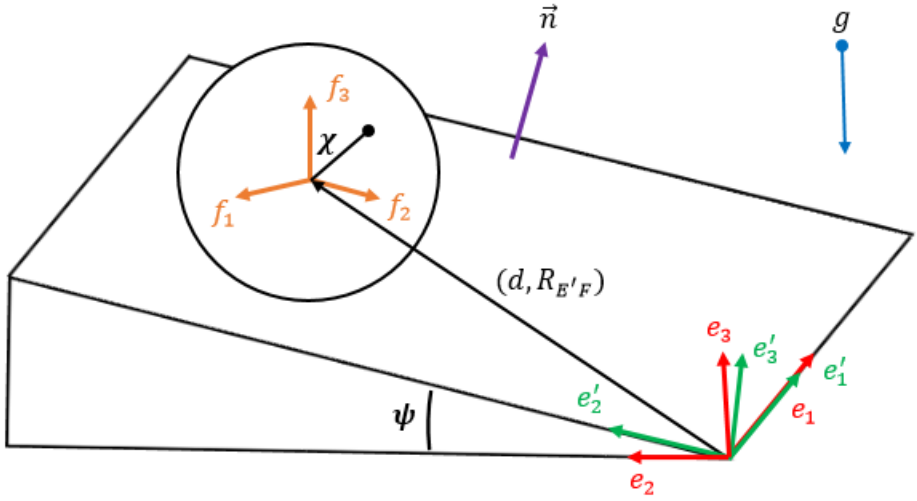

Figure 4.2: Model of a Generic Spherical Robot on Sloped Terrain.

where $(\star)$ denotes possibly nonzero terms that do not affect the analysis. This Lie bracket does not contain components along $T_qSO(3)$ since the $T_qSO(3)$-component of $[f(z), h_i(z)]$ is *not* a function of $\tilde{p}$ or $\dot{r}$. Each of the possible nonzero components above can be neutralized using first or second degree Lie brackets given by Theorem 4.2.1, thus establishing STLC by Sussmann's condition. □

Physically, requiring $\mathbb{B}(R,r)$ to be surjective enables the control system to select inputs $\ddot{r}$ that generate changes in $(\dot{r}, \tilde{p})$ which, when propogated through the momenta equations (4.15), permit control of motion in the two directions along the supporting plane orthogonal to the surface normal.

4.2.3 Dynamics on a Sloped Plane

This brief subsection considers a generic spherical robot on sloped terrain, as shown in Fig. 4.2. Frames E and F are defined as in Subsection 4.2.1. Frame $E' = \{e_1', e_2', e_3'\}$ denotes a rotated inertial frame such that e_2' points up the slope with angle of inclination ψ and basis vector e_3' is parallel with the surface normal. The mass of the vehicle is distributed according to the following definition,

Definition 4.2.2. Let M_s denote the vehicle's "structure" mass, which consists of the mass of those components that produce a COM centered at the COR, i.e. the robot's shell and any symmetrical internal support structures. Let the "actuator" mass, M_a, denote the mass of any mechanism used to displace the COM and internal eccentricities arising from fixed components.

Vectors (α, β, γ) are now defined with respect to frame E'. Two new advected parameters are introduced to enable $SE(3)$-reduction:

$$\kappa \triangleq R^T e_3,\ \zeta \triangleq R^T d^s, \tag{4.20}$$

where κ represents the direction of gravity and ζ represents d^s in the body frame F. Although the vehicle's position is no longer cyclic as in Subsection 4.2.1, an augmented system including ζ and κ will enable $SE(3)$-invariance using the reduction scheme of Section 3.4. The kinetic energy does not change from the flat plane case when expressed in frame E', but the potential energy is now given as,

$$V = (M_s + M_a)g\langle\zeta, \kappa\rangle + M_a g\langle\chi(r), \kappa\rangle, \tag{4.21}$$

where $\chi(r)$ denotes the COM location of M_a expressed in frame F. Choosing to express $\chi(r)$ along the basis $\{\alpha, \beta, \gamma\}$, the net torque on the spherical robot due to gravity can be written as,

$$T_g = g\hat{\kappa}\Big((M_a + M_s)r_b\gamma + M_a(\chi_\alpha(r)\alpha + \chi_\beta(r)\beta + \chi_\gamma(r)\gamma)\Big).$$

The net torque must equal zero at equilibrium, i.e. the ball remains fixed on the slope. An equilibrium point may not exist for every vehicle and every inclination angle ψ. Suppose that the actuator's center of mass can be moved a maximum distance of $\rho \cdot r_b$, where $\rho \leq 1$ is a system specific constant, e.g. a pendulum-actuated design may have $\rho = l/r_b$ where $l \leq r_b$ is the pendulum's length. Then, equilibrium points will not exist when the angle of inclination exceeds a critical value:

$$\psi > \sin^{-1}\Big(\rho\frac{M_a}{M_s}\Big). \tag{4.22}$$

Equation (4.22) exposes the importance of the ratio (M_a/M_T) in designing barycentric spherical robots (BSR). For example, suppose that a pendulum-actuated BSR is designed with $l = r_b/2$ and must maintain stability on a 20° incline. To satisfy these requirements the pendulum's mass M_a must be nearly 70% of the total system mass.

Only minor changes are needed to derive the sloped-plane dynamics from the flat-plane dynamics derived earlier. Note that (X_α, X_β) are defined with respect to frame E' instead of E. The only other change is to make the following substitutions to the gravity terms found in the momentum differential equations (4.12) for the flat-plane case:

$$\hat{\gamma}\frac{\partial V}{\partial \gamma} \cdot \alpha \to \langle T_g, \alpha\rangle,\ \hat{\gamma}\frac{\partial V}{\partial \gamma} \cdot \beta \to \langle T_g, \beta\rangle.$$

These changes model the modified gravity torque that the vehicle encounters on the sloped plane. With these minor changes, equations (4.10)-(4.13), $\ddot{r} = u$, and the constraints (4.5) fully define the vehicle's motion on the sloped plane.

4.2.4 STLC on Sloped Terrain

Recall from Subsection 4.2.3 that the dynamics for a spherical vehicle on a sloped plane could be easily derived from the dynamics on a flat plane with simple modifications to the potential energy $V(\cdot)$ and the allowable directions of motion (X_α, X_β). Consequently, the theorem establishing STLC is identical.

Theorem 4.2.3 (STLC, Sloped Terrain)**.** At an equilibrium point z^*, STLC for a spherical robot on sloped terrain follows from Theorem 4.2.2.

Proof. Identical to that of Theorem 4.2.2, using the modified dynamics described in Subsection 4.2.3. □

Equivalence of STLC conditions between the flat and sloped-plane cases is intuitive since the sloped plane is dynamically equivalent to the flat-plane case with a rotated gravity vector, which has the effect of simply changing the location of equilibrium points in the configuration space.

4.2.5 Dynamics on Undulating Terrain

Now consider the generic case of a spherical vehicle rolling on undulating terrain (Fig. 4.1). Let,

$$\alpha \triangleq R^T \frac{\varphi_u}{||\varphi_u||},\ \beta \triangleq R^T \frac{\varphi_v}{||\varphi_v||},\ \gamma \triangleq R^T n(t), \tag{4.23}$$

where $\varphi(u, v)$ parameterizes the terrain geometry and subscripts denote partial differentiation. Notice that the basis (α, β, γ) defines the Gauss frame on a regular surface. The allowable directions of motion, (X_α, X_β), can be parameterized as in equation (4.7) but with the modification that the Gauss frame is time-varying whereas the frame $E = \{e_1, e_2, e_3\}$ was stationary.

Advection equations can be derived for (α, β, γ) using equation (4.3), which defines the angular velocity of the Gauss frame, ω^s_G,

$$\dot{\alpha} = \hat{\alpha}\left(\omega^b - R^T\omega^s_G\right),\ \dot{\beta} = \hat{\beta}\left(\omega^b - R^T\omega^s_G\right),\ \dot{\gamma} = \hat{\gamma}\left(\omega^b - R^T\omega^s_G\right).$$

These equations expose the fact that (α, β, γ) vary in time due to the relative angular velocity between the body and Gauss frame. This was not encountered previously

in the flat or sloped terrain case because the Gauss frame of a flat plane is constant, i.e. $\omega_G^s = 0$. As before, (α, β, γ) define a rotation matrix W whose differential equation can be succinctly expressed as:

$$\dot{W} = -\left(\hat{\omega}^b - R^T \hat{\omega}_G^s R\right) W. \tag{4.24}$$

A unique contact point exists between the robot and terrain due to the curvature assumptions made in (4.4). Let $\varphi(u^*, v^*)$ denote the restriction of $\varphi(u, v)$ to the point of contact on the terrain surface. The following relationship describes the Cartesian location of the ball's COR,

$$\varphi(u^*, v^*) + r_b n(u^*, v^*) = d^s, \tag{4.25}$$

where $n(u^*, v^*)$ denotes the surface normal at the point of contact. The no-slip constraint induces a constaint on $(\dot{u}^*, \dot{v}^*)$ via equation (4.25). Differentiating (4.25), and using the constraints (4.5) and regular surface assumption yields,

$$\begin{pmatrix} \dot{u}^* \\ \dot{v}^* \end{pmatrix} = r_b M^{-1} (I + r_b K)^{-1} S_{2\times 2} \begin{pmatrix} \omega_\alpha^b \\ \omega_\beta^b \end{pmatrix}, \; S_{2\times 2} \triangleq \begin{bmatrix} 0 & 1 \\ -1 & 0 \end{bmatrix}, \tag{4.26}$$

where invertibility of $(I + r_b K)$ follows from (4.4). The space $(\dot{u}^*, \dot{v}^*)$ must be spanned by good Lie brackets in order to show STLC in what follows.

As in Subsection 4.2.3, let M_a and M_s denote the vehicle's actuator and structure mass. Existence conditions for an equilibrium point are identical to the sloped-plane case with the exception that the angle of inclination ψ pertains to the local tangent plane. Similar to the sloped-plane case, the advected parameters κ and ζ are necessary to permit full $SE(3)$ reduction. The nonholonomic momenta's differential equation still has the form given by equation (4.11), with dependence on ω_G^s. Let the body angular velocity of the Gauss frame be denoted by $\omega_G^b = R^T \omega_G^s$, with $\{\omega_{G,\alpha}^b, \omega_{G,\beta}^b, \omega_{G,\gamma}^b\}$ its components along (α, β, γ). Evaluating (4.11) produces the following:

$$\begin{aligned} \dot{p}_\alpha &= r_b(\omega_\alpha^b - \omega_{G,\alpha}^b)\left(\omega_\beta^b \langle m_{12}, \alpha\rangle - \omega_\alpha^b \langle m_{12}, \beta\rangle + \langle m_{13}\dot{r}, \gamma\rangle\right) + \omega_{G,\gamma}^b p_\beta + \langle T_g, \alpha\rangle, \\ \dot{p}_\beta &= r_b(\omega_\beta^b - \omega_{G,\beta}^b)\left(\omega_\beta^b \langle m_{12}, \alpha\rangle - \omega_\alpha^b \langle m_{12}, \beta\rangle + \langle m_{13}\dot{r}, \gamma\rangle\right) - \omega_{G,\gamma}^b p_\alpha + \langle T_g, \beta\rangle, \end{aligned} \tag{4.27}$$

Equations (4.10), (4.24)-(4.27), and $\ddot{r} = u$ fully define the motion of a spherical robot on undulating terrain.

4.2.6 STLC on Undulating Terrain

Before writing the dynamics in control-affine form, the coordinate change defined in (4.14), $(p_\alpha, p_\beta) \to (\tilde{p}_\alpha, \tilde{p}_\beta)$, is used to rewrite the momenta differential equations:

$$\begin{pmatrix} \dot{\tilde{p}}_\alpha \\ \dot{\tilde{p}}_\beta \end{pmatrix} = \begin{pmatrix} r_b \bar{\omega}^b_\alpha (\omega^b_\beta \langle m_{12}, \alpha \rangle - \omega^b_\alpha \langle m_{12}, \beta \rangle) + \omega^b_{G,\gamma} \tilde{p}_\beta - \bar{\omega}^b_\beta \langle \gamma, m_{23}, \dot{r} \rangle + T_{g,\alpha} \\ r_b \bar{\omega}^b_\beta (\omega^b_\beta \langle m_{12}, \alpha \rangle - \omega^b_\alpha \langle m_{12}, \beta \rangle) - \omega^b_{G,\gamma} \tilde{p}_\alpha + \bar{\omega}^b_\alpha \langle \gamma, m_{23} \dot{r} \rangle + T_{g,\beta} \end{pmatrix} + \mathbb{B}(R, r)\ddot{r},$$

where $\bar{\omega}^b_\alpha = \omega^b_\alpha - \omega^b_{G,\alpha}$ and $\bar{\omega}^b_\beta = \omega^b_\beta - \omega^b_{G,\beta}$. Controllability calculations are computed on a set of independent variables, of the same number as the system's degrees of freedom, that describe the system's state. Variable redundancy can be eliminated by using the following substitutions.

1. The map, $\Omega(u^*, v^*) \triangleq \varphi(u^*, v^*) + r_b n(u^*, v^*)$, is a *parallel patch* of $\varphi(\cdot, \cdot)$ that inherits regularity from surface S. Thus, $\Omega : (u^*, v^*) \to d^s$ defines a homeomorphism and dependencies on d^s can be replaced by dependencies on (u^*, v^*), i.e. controllability at (u^*, v^*) is equivalent to controllability at d^s modulo the holonomic constraint keeping the vehicle on S.

2. Interestingly, the advected parameter ζ does not appear in the final equations, and κ can be written as a function of R using its definition (4.20). Although the potential energy depends on the ball's position ζ, the resulting potential force does not.

3. The advected parameters (α, β, γ) can be written as functions of (u^*, v^*) and the rotation matrix R from their definitions (4.23).

The minimum set of variables sufficient to establish controllability over the system is then $z = (u^*, v^*, \tilde{p}_\alpha, \tilde{p}_\beta, r, \dot{r}, R)$, which admits the following control-affine form, where

$$f(z) = \begin{bmatrix} r_b (M + r_b K M)^{-1} S_{2\times 2} \omega^b_{\alpha\beta} \\ r_b \bar{\omega}^b_\alpha (\omega^b_\beta \langle R m_{12}, \frac{\varphi_u}{||\varphi_u||} \rangle - \omega^b_\alpha \langle R m_{12}, \frac{\varphi_v}{||\varphi_v||} \rangle) + \omega^b_{G,\gamma} \tilde{p}_\beta - \bar{\omega}^b_\beta \langle R m_{23} \dot{r}, n \rangle + T_{g,\alpha} \\ r_b \bar{\omega}^b_\beta (\omega^b_\beta \langle R m_{12}, \frac{\varphi_u}{||\varphi_u||} \rangle - \omega^b_\alpha \langle R m_{12}, \frac{\varphi_v}{||\varphi_v||} \rangle) - \omega^b_{G,\gamma} \tilde{p}_\alpha + \bar{\omega}^b_\alpha \langle R m_{23} \dot{r}, n \rangle + T_{g,\beta} \\ \dot{r} \\ 0_{m\times 1} \\ \omega^b_\alpha \left(\frac{\varphi_u}{||\varphi_u||} \right)^\wedge + \omega^b_\beta \left(\frac{\varphi_v}{||\varphi_v||} \right)^\wedge \end{bmatrix} \tag{4.28}$$

is the drift vector field and,

$$h_i(z) = \begin{bmatrix} 0_{2\times 1} & \mathbb{B}(\cdot)e_i & 0_{m\times 1} & e_i & 0_{3\times 3} \end{bmatrix}^T, \forall i = 1,\dots,m \tag{4.29}$$

are the control vector fields. Notice that when $\omega_G^b = 0$, the control-affine form reduces to the results previously derived for the flat and sloped plane cases.

An important distinction is the presence of the terms $\varphi_u/||\varphi_u||$ and $\varphi_v/||\varphi_v||$ in the $T_qSO(3)$ coordinate of $f(z)$. Whereas in the flat and sloped plane case a Lie bracket of the fourth degree accomplished rotation about the surface normal as long as $\mathbb{A}(\cdot)$ had full row rank, in this case *some surfaces will prevent rotations about the surface normal regardless of the nonholonomic connection*. For example, when the vehicle rolls over a sphere with matching radius r_b then STLC cannot be achieved because rotations about $n(t)$ will be annihilated in the fourth degree Lie bracket [50].

This effect occurs more generally whenever the local surface $\varphi(\cdot,\cdot)$ is a *specular image* of a sphere with radius r_b at the equilibrium point [53]. Suppose that two surfaces $\varphi(u,v)$ and $\vartheta(u,v)$ share a contact point at $\varphi(\bar{u},\bar{v})$. Let $\bar{G}$ denote the normalized Gauss frame at the point of contact $\varphi(\bar{u},\bar{v})$, and let $\Sigma = \text{diag}(1,1,-1)$. The reflection of $\varphi(u,v)$ about the tangent plane at $(\bar{u},\bar{v})$ is defined by the action of a reflection map $s \circ \varphi(u,v)$.

$$s \circ \varphi(u,v) = \bar{G}\Sigma\bar{G}^T\Big(\varphi(u,v) - \varphi(\bar{u},\bar{v})\Big) + \varphi(\bar{u},\bar{v}).$$

Surface $\vartheta(x,y)$ is a specular image of $\varphi(u,v)$ at the point $(\bar{u},\bar{v})$ if there exists a rigid body motion (R,d), a reflection map s, and a diffeomorphism $\Phi : (x,y) \to (u,v)$ such that the following condition holds,

$$R\vartheta(x,y) + d = s \circ \vartheta \circ \Theta(x,y).$$

Two surfaces are specular when they appear to be reflections of one another in a local neighborhood about the contact point [53]. Local controllability is always prevented when a surface rolls without slip and spin on terrain that is its specular image. Interestingly, this can be interpreted as the Gauss-Bonnet theorem imposing a holonomic constraint [50]. However, the curvature constraints (4.4) imposed on the surfaces in this work prohibit terrains that are specular images of an r_b-radius sphere. Thus, the following theorem holds.

Theorem 4.2.4 (STLC, Smooth Terrain)**.** If the terrain satisfies curvature constraints (4.4), $\mathbb{B}(u^*,v^*,r,R)$ is surjective, and $\dim(r) \geq 2$, then STLC holds from equilibrium point z^* for the system (4.28)-(4.29).

Proof of Theorem 4.2.4. Writing the connection as in (4.16) one can compute the first degree Lie bracket $[f(z), h_i(z)]$ evaluated at an equilibrium point z^* as,

$$[f(z), h_i(z)]|_{z=z^*} = \begin{bmatrix} -M^{-1}(\frac{1}{r_b} + K)^{-1} S_{2\times 2} \mathbb{A}(R,r) e_i \\ 0_{2\times 1} \\ e_i \\ 0_{m\times 1} \\ -\langle e_1, \mathbb{A}(R,r) e_i \rangle \left(\frac{\varphi_u}{||\varphi_u||}\right)^\wedge R - \langle e_2, \mathbb{A}(R,r) e_i \rangle \left(\frac{\varphi_v}{||\varphi_v||}\right)^\wedge R \end{bmatrix}.$$

As in the proof of Theorem 4.2.2, the vectors $\{h_i(z), [f(z), h_i(z)]\}$ span the input space $(r, \dot{r})$. If $\mathbb{B}(\cdot)$ possesses full row rank, the vectors $\{h_i(z)\}$ span the momentum space. Full row rank of the connection $\mathbb{A}(\cdot)$ ensures that the vectors $\{[f(z), h_i(z)]\}$ span two DOF of $T_q SO(3)$ and the space $(\dot{u}, \dot{v})$. Allowing $(\star)$ to denote a possibly nonzero component, the fourth degree Lie bracket $[[[f(z), h_i(z)], f(z)], h_j(z)]$ evaluated at the equilibrium point can be written as:

$$\begin{bmatrix} \star \\ \star \\ \star \\ \star \\ (\star)\left(\frac{\varphi_u}{||\varphi_u||}\right)^\wedge + (\star)\left(\frac{\varphi_v}{||\varphi_v||}\right)^\wedge + \left(e_i^T \mathbb{A}^T (-S + S(\frac{1}{r_b} + K)^{-T} K^T + K(\frac{1}{r_b} + K)^{-1} S) \mathbb{A} e_j\right) \hat{n} R \end{bmatrix}$$

Notice that when rolling on a flat plane, i.e. $K = 0$, the Lie brackets and necessary STLC conditions presented in Theorem 4.2.2 are recovered. Curved terrain introduces extra terms dependent on the curvature tensor K into the $T_q SO(3)$ coordinate corresponding to rotations about the normal. When the terrain is a specular image to a sphere of radius r_b, the curvature tensor is given by $K = \frac{1}{r_b} I_{2\times 2}$, which annihilates the remaining component of the $T_q SO(3)$ coordinate as predicted by [50, 53]. More generally, this third degree of freedom is annihilated by any surface whose Gaussian curvature $K_G = \kappa_1 \kappa_2 = 1/r_b^2$. But note that any surface with this Gaussian curvature would have violated the curvature assumption (4.4). Thus, by the LARC, system (4.28)-(4.29) is accessible using Lie brackets up to the fourth degree. To establish STLC, the "bad" third degree bracket $[[f(z), h_i(z)], h_i(z)]$ must be analyzed and this bracket has no component along $T_q SO(3)$ and all of its nonzero components can be spanned by Lie brackets of lesser order. Thus, the system (4.28)-(4.29) is STLC at equilibrium point z^*. □

Symbol	Description
M_T	Total system mass
M_i	Mass of single magnet
$\Omega \in \mathbb{R}^{3\times n}$	Alignment matrix of internal magnets.
$(\mathcal{X},\mathcal{V}) \in \mathbb{R}^n$	Distance/velocity of magnets along axes.
$I_{m,i}$	Magnet i's inertia tensor measured in a COM-centered frame parallel to body frame F.
$I_{s,cor}$	Structure's inertia tensor measured at sphere's COR measured in body frame F.
$\Phi(\mathcal{X})$	Effective moment of inertia measured about body frame F.

Table 4.2: Variables Used for Moball.

4.3 STLC Examples

Three examples are considered that apply the ideas developed in this chapter: (i) Moball rolling on the plane, (ii) a rotor-powered vehicle rolling on a helicoid, (iii) a common class of multirotor vehicles in flight. The second example demonstrates that the STLC conditions apply to a generic class of vehicles encompassing, but more general than, BSRs. The third example illustrates that the reduced method of dynamics in Chapter 3 enables insight into the STLC of unconstrained dynamical systems as well.

4.3.1 Simplified Moball on Flat Terrain

Moball is a barycentric mechanism (Fig. 1.2) that relies on translating magnets to manipulate its COM position. In general, Moball contains n magnets translating along separate axes $\{q_1, q_2, \ldots, q_n\}$ expressed in the body frame. Let matrix Ω contain unit vectors, collinear with the magnet motions, as columns. Consider the case where Moball has three magnets arranged on orthogonal axes, i.e. $\Omega = I_{3\times 3}$. Table 4.2 describes the variables used in this example. When the Moball moves on a flat plane, the system's Lagrangian can be expressed as,

$$L(q,\dot{q}) = \frac{1}{2}\begin{bmatrix} \dot{d}^b \\ \omega^b \\ \mathcal{V} \end{bmatrix}^T \begin{bmatrix} M_T I_{3\times 3} & -M_i\widehat{\Omega\mathcal{X}} & M_i\Omega \\ M_i\widehat{\Omega\mathcal{X}} & \Phi(\mathcal{X}) & 0 \\ M_i\Omega^T & 0 & M_i I_{n\times n} \end{bmatrix} \begin{bmatrix} \dot{d}^b \\ \omega^b \\ \mathcal{V} \end{bmatrix} - M_i g\langle e_3, R\Omega\mathcal{X}\rangle,$$

$$\Phi(\mathcal{X}) \triangleq M_i||\mathcal{X}||^2 + \sum_{i=1}^{n}\left(I_{m,i} - M_i\mathcal{X}_i^2 f_i f_i^T\right) + I_{s,cor},$$

where $\Phi(\mathcal{X})$ represents the effective moment of inertia. Under the no-slip/no-spin constraints, with advected parameters (α,β,γ) defined as in (4.6), the dynamics can be written compactly using the formalism in Subsection 4.2.1:

$$
\begin{aligned}
\begin{bmatrix}\omega_\alpha^b \\ \omega_\beta^b\end{bmatrix} &= \mathbb{I}^{-1}(\alpha,\beta,\gamma,\mathcal{X})\left(\begin{bmatrix} r_b M_i \beta^T \\ -r_b M_i \alpha^T\end{bmatrix}\mathcal{V} + \begin{bmatrix} p_\alpha \\ p_\beta\end{bmatrix}\right), \\
\dot{p}_\alpha &= r_b M_i \omega_\alpha^b\left(\omega_\alpha^b\langle\mathcal{X},\beta\rangle - \omega_\beta^b\langle\mathcal{X},\alpha\rangle + \langle\gamma,\mathcal{V}\rangle\right) - M_i g\langle\mathcal{X},\beta\rangle, \\
\dot{p}_\beta &= r_b M_i \omega_\beta^b\left(\omega_\alpha^b\langle\mathcal{X},\beta\rangle - \omega_\beta^b\langle\mathcal{X},\alpha\rangle + \langle\gamma,\mathcal{V}\rangle\right) + M_i g\langle\mathcal{X},\alpha\rangle, \\
\ddot{\mathcal{X}} &= \vec{u},
\end{aligned}
\tag{4.30}
$$

where,

$$
\mathbb{I}^{-1}(\alpha,\beta,\gamma,\mathcal{X}) = \frac{1}{\det(\mathbb{I})}\begin{bmatrix} r_b^2 M_T + 2r_b M_i\langle\mathcal{X},\gamma\rangle + \langle\beta,\Phi(\mathcal{X})\beta\rangle & -\langle\alpha,\Phi(\mathcal{X}),\beta\rangle \\ -\langle\alpha,\Phi(\mathcal{X})\beta\rangle & r_b^2 M_T + 2r_b M_i\langle\mathcal{X},\gamma\rangle + \langle\alpha,\Phi(\mathcal{X}),\alpha\rangle\end{bmatrix}
$$

is the locked-inertia tensor (4.10). The steering matrix (4.2.1),

$$
\mathbb{B}(\alpha,\beta) = \begin{bmatrix} r_b M_i \beta^T \Omega \\ -r_b M_i \alpha^T \Omega\end{bmatrix}
$$

is full rank since $\Omega = I_{3\times 3}$ in this example. Therefore, Moball satisfies the conditions of Theorem 4.2.2 in this configuration. Moreover, we expect this configuration to be controllable from *any* equilibrium point on the flat plane since $\mathbb{B}(\alpha,\beta)$ will always maintain full rank. Now, consider $\Omega = [e_1, e_1, e_3]$ representing the case where two magnets slide along a common axis, and no magnet's motion is aligned along the body y-axis. In this case, $\mathbb{B}(\alpha,\beta)$ will certainly fail to be surjective when the vehicle's orientation is such that the body y-axis lies in the e_1, e_2 plane. Physically, when the unactuated axis lies on the plane parallel with the ground, motions cannot be instantaneously achieved in one direction and controllability is unachievable. In nearly all other orientations, one can easily determine from the surjectivity of $\mathbb{B}(\alpha,\beta)$ that the vehicle is controllable.

4.3.2 Tri-Rotor Vehicle Rolling on a Helix

Consider a helicoid surface parameterized by $\varphi(u,v) = (uc_v, us_v, \rho v)^T$, where c_v and s_v denote $\cos(\cdot)$ and $\sin(\cdot)$ functions, and ρ is a constant. This surface's normalized Gauss frame is given by:

$$
\begin{bmatrix} \frac{\varphi_u}{||\varphi_u||} & \frac{\varphi_v}{||\varphi_v||} & n\end{bmatrix} = \begin{bmatrix} c_v & \frac{-us_v}{\sqrt{\rho^2+u^2}} & \frac{\rho s_v}{\sqrt{\rho^2+u^2}} \\ s_v & \frac{uc_v}{\sqrt{\rho^2+u^2}} & \frac{-\rho c_v}{\sqrt{\rho^2+u^2}} \\ 0 & \frac{\rho}{\sqrt{\rho^2+u^2}} & \frac{u}{\sqrt{\rho^2+u^2}}\end{bmatrix}.
$$

Now suppose that a spherical vehicle is placed on the surface as in Fig. 4.3. This vehicle is actuated by three internal rotors placed a distance l along each orthogonal

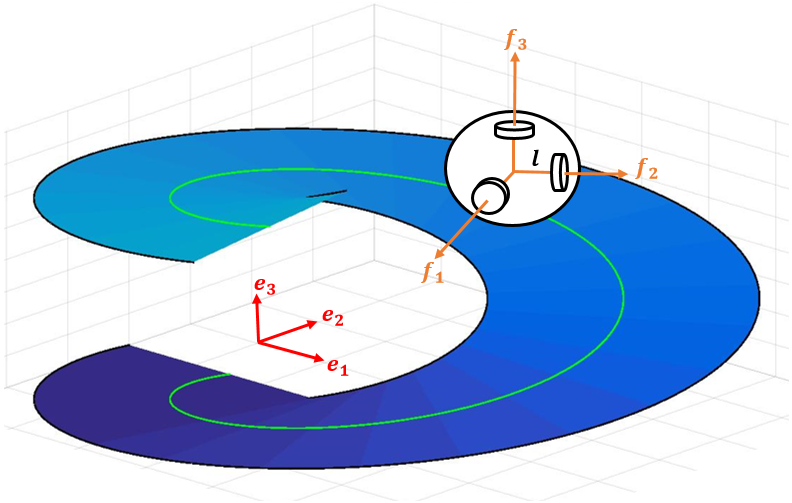

Figure 4.3: Tri-Rotor Spherical Vehicle Rolling on a Helicoid.

Symbol	Description
M_T	Total system mass
M_r	Rotor mass
l	Rotor i's distance along axis f_i.
$I_r \in \mathbb{R}^{3\times3}$	Rotor i's inertia tensor measured at COM with respect to frame F.
I_s	Structure's inertia tensor, measured at COR.
$\Theta \in \mathbb{R}^3$	Rotor angles with positive measured according to frame F.

Table 4.3: Variables Used for Tri-Rotor Spherical Robot.

body axis $\{f_1, f_2, f_3\}$. The vehicle's center of mass lies along the vector $\vec{1} \equiv (1,1,1)$ in the body frame, i.e. the robot's fixed, eccentric COM does not coincide with the geometric COR. Although this vehicle does not displace its COM for propulsion like a BSR (e.g. Moball), it fits within the framework of our theory and we can apply Lagrangian reduction and the STLC conditions previously derived. Table 4.3 lists the variables used in this example.

The existence of static equilibrium points must be established for this vehicle and surface. The maximum angle of inclination of the local tangent plane for which an equilibrium position exists is given as ψ_{max},

$$\psi_{max} = \sin^{-1}\left(\frac{3\sqrt{3}M_r l}{M_T r_b}\right),$$

which follows from (4.22). In this particular example, suppose that $3M_r = (1/2)M_T$ and $l = r_b$, which leads to a maximum inclination angle of 60°. Assume that $\rho = 1$ and that the vehicle sits at $(u,v) = (1,\frac{\pi}{4})$. The local tangent plane's angle

of inclination is 45° at this position. Consequently, static equilibrium exists only for two orientations (e.g. the body vector $\vec{1}$ must point "up" the slope with the center of mass lying on the e_3 axis over the contact point). It is from these points that STLC can be verified. Under the no-slip/no-spin constraints (4.5), the system's Lagrangian can be written as,

$$L = \frac{1}{2}\begin{bmatrix} \dot{d}^b \\ \omega^b \\ \dot{\Theta} \end{bmatrix}^T \begin{bmatrix} M_T & -M_r l\hat{1} & 0 \\ M_r l\hat{1} & \sigma & a \\ 0 & a & a \end{bmatrix} \begin{bmatrix} \dot{d}^b \\ \omega^b \\ \dot{\Theta} \end{bmatrix} - M_r g l \langle R\vec{1}, e_3 \rangle,$$

where a denotes the moment of inertia about the rotation axis for each rotor. A simplifying feature is the constant diagonal structure of the effective moment of inertia. Let $\sigma I_{3\times 3} \triangleq (\mathrm{Tr}(I_r) + 2M_r l^2) I_{3\times 3} + I_s$ denote the effective moment of inertia, where $\mathrm{Tr}(\cdot)$ represents the matrix trace. From inspection of the Lagrangian and constraints, only two advected parameters are necessary to enable $SE(3)$ reduction: $\kappa \triangleq R^T e_3$ and $\gamma \triangleq R^T n(t)$. However, (α, β) are implemented as the local tangent directions as before. The governing dynamics equations can succinctly be expressed as:

$$\begin{aligned}
\omega^b_{\alpha\beta} &= \frac{1}{r_b^2 M_T + 2 r_b M_r l \langle \vec{1}, \gamma \rangle + \sigma} \begin{bmatrix} p_\alpha - a\langle \alpha, \dot{\Theta} \rangle \\ p_\beta - a\langle \beta, \dot{\Theta} \rangle \end{bmatrix}, \\
\dot{p}_\alpha &= -M_r l r_b \bar{\omega}^b_{G,\alpha} (\omega^b_\beta \langle \vec{1}, \alpha \rangle - \omega^b_\alpha \langle \vec{1}, \beta \rangle) + \omega^b_{G,\gamma} p_\beta + M_r g l \hat{\kappa}\vec{1} \cdot \alpha, \\
\dot{p}_\beta &= -M_r l r_b \bar{\omega}^b_{G,\beta} (\omega^b_\beta \langle \vec{1}, \alpha \rangle - \omega^b_\alpha \langle \vec{1}, \beta \rangle) - \omega^b_{G,\gamma} p_\alpha + M_r g l \hat{\kappa}\vec{1} \cdot \beta, \\
\ddot{\Theta} &= \vec{u},
\end{aligned}$$

where again $\bar{\omega}^b_{G,\alpha} = \omega^b_\alpha - \omega^b_{G,\alpha}$ and $\bar{\omega}^b_{G,\beta} = \omega^b_\beta - \omega^b_{G,\beta}$. To complete the dynamical equations the surface can be described by (M, K, T),

$$M = \begin{bmatrix} 1 & 0 \\ 0 & \sqrt{\rho^2 + u^2} \end{bmatrix}, \; K = \begin{bmatrix} 0 & \frac{\rho}{\rho^2+u^2} \\ \frac{\rho}{\rho^2+u^2} & 0 \end{bmatrix}, \; T = \begin{bmatrix} 0 & \frac{u}{\rho^2+u^2} \end{bmatrix},$$

which are sufficient to fully describe the advection differential equations governing (α, β, γ) shown in (4.24), the equations governing (u^*, v^*) shown in (4.26), and the definition of ω^b_G shown in (4.3). Furthermore, the advection equation governing κ can be written easily as $\dot{\kappa} = \hat{\kappa}\omega^b$. The principal curvatures for this surface both have a magnitude of $\rho/(\rho^2 + u^2)$. For this surface to globally satisfy the curvature constraints (4.4), it is enough to require $r_b < \rho$. Otherwise, one must locally determine if the surface satisfies (4.4).

Analogous to the Moball example, the steering matrix,

$$\mathbb{B}(\alpha, \beta) = a \begin{bmatrix} -\alpha^T \\ -\beta^T \end{bmatrix},$$

is full rank since the m_{23} entry of the mass matrix is a nonzero multiple of the identity. As long as the helicoid satisfies the curvature constraints (4.4), we expect this vehicle to maintain STLC from *any* equilibrium point since the steering matrix will always maintain full rank. Rearranging the orientation of the rotors within the vehicle could lead to a loss of STLC as well and these cases can be checked by inspecting the rank of the steering matrix $\mathbb{B}(\alpha, \beta)$.

4.3.3 Multirotor Controllability

The reduced/reconstructed dynamics of multirotors introduced in Subsection (3.5.3) will be used to assert STLC for a broad class of common multirotors. The class of multirotors for which STLC conditions will apply are defined by the following attributes.

Definition 4.3.1 (Common Multirotor Class)**.** Consider a class of multirotors characterized by the following common properties,

1. The multirotor has an even number of rotors (e.g. $2n$ rotors), $n \geq 2$, and each rotor produces a thrust in an upward direction along the f_3 body axis.

2. Rotors are placed in reflected pairs about the x-z and y-z body planes. If $\sigma_i = \begin{pmatrix} \sigma_{i,x} & \sigma_{i,y} & \sigma_{i,z} \end{pmatrix}$ denotes the position of the center of the i^{th} rotor hub in the body frame, then the reflection of σ_i is denoted by $\sigma_{i,r} = \begin{pmatrix} -\sigma_{i,x} & -\sigma_{i,y} & \sigma_{i,z} \end{pmatrix}$. Thus, the complete layout of $2n$ rotors can be enumerated by the vectors $\{\sigma_1, \ldots, \sigma_n\}$.

3. All rotors are placed in the x-y body plane such that $\sigma_{i,z} = 0$ for all $i \in [1, n]$. Furthermore, the set $\{\sigma_i\}$ span the plane.

4. Neighboring rotors spin in an alternating clockwise/counter-clockwise direction. No two neighboring rotors spin in the same direction.

This common class of multirotors describes most commercially available quad, hexi, and optocopters. The assumptions of Definition (4.3.1) were chosen to be as unrestrictive and commonly-encountered as possible. STLC results can certainly

be derived after relaxing some of these assumptions, although the results may be vehicle-specific.

The dynamics for a multirotor characterized by Definition (4.3.1) follow from Subsection (3.5.3):

$$\begin{aligned}
\begin{bmatrix} \dot{d}^b \\ \omega^b \end{bmatrix} &= \begin{bmatrix} \frac{1}{M_T}\vec{p} \\ \Phi^{-1}(\vec{l} - J\langle \mathbf{1}, \varpi \rangle e_3) \end{bmatrix}, \\
\dot{\vec{l}} &= \vec{l} \times \Phi^{-1}(\vec{l} - J\langle \mathbf{1}, \varpi \rangle e_3 \rangle + \Lambda \varpi^2, \\
\dot{\vec{p}} &= \vec{p} \times \Phi^{-1}(\vec{l} - J\langle \mathbf{1}, \varpi \rangle e_3) - g M_T \vec{\gamma} + \Psi \varpi^2, \\
\dot{\gamma} &= \gamma \times \Phi^{-1}(\vec{l} - J\langle \mathbf{1}, \varpi \rangle e_3),
\end{aligned}$$

where the i^{th} column of $\Lambda \in \mathbb{R}^{3\times 2n}$ is given by $c_T \sigma_i \times e_3 - \phi_i c_Q e_3$, the i^{th} column of $\Psi \in \mathbb{R}^{3\times 2n}$ is given by $c_T e_3$, and $\varpi^2 = \{\varpi_i^2\}_{i=1}^{2n}$. The definitions of Λ and Ψ follow from Subsection (3.5.3): Λ and Ψ map rotor velocities squared into moments and forces on the vehicle, respectively. Of course, STLC can only be established at equilibrium points, and the conditions for an equilibrium point of this dynamical system are,

$$g M_T \vec{\gamma} = \Psi \varpi^2, \;\; \vec{l} = J\langle \mathbf{1}, \varpi \rangle e_3, \;\; \Lambda \varpi^2 = \vec{0}. \tag{4.31}$$

Based on the range space of Ψ, the condition $g M_T \vec{\gamma} = \Psi \varpi^2$ implies that $\vec{\gamma} = e_3$, which in turn implies that the vehicle has zero pitch angle, zero roll angle, and an arbitrary yaw angle. The second condition ensures that the total angular momentum, $\Phi \omega^b$, is equal to zero and the third condition ensures that the rotors produce no moment on the vehicle in equilibrium. When the number of rotors exceeds four, the nontrivial nullspaces of Λ and Ψ imply that ϖ may take a range of values in a finite-dimensional space while still satisfying equilibrium. Concatenating the conditions $\Lambda \varpi^2 = 0$ and $\Psi \varpi^2 = g M_T \vec{\gamma}$ together yields,

$$\begin{bmatrix} \Lambda \\ c_T \mathbf{1}^T \end{bmatrix} \varpi^2 = \begin{bmatrix} \vec{0} \\ g M_T \end{bmatrix}.$$

It is reasonable to compute STLC about a selected equilibrium point defined by,

$$\varpi^2 = \begin{bmatrix} \Lambda \\ c_T \mathbf{1}^T \end{bmatrix}^\dagger \begin{bmatrix} \vec{0} \\ g M_T \end{bmatrix} = \mathbf{1} \frac{g M_T}{2 n c_T}, \tag{4.32}$$

where $\dagger$ denotes the pseudoinverse. Use of the pseudoinverse is appropriate as this solution minimizes the component of ϖ^2 in the nullspace of Λ and Ψ, and thus minimizes the energy consumed by the vehicle's motors. Hence, at this equilibrium

point each of the rotors spins at the same rate. Selecting ϖ^2 to have a component in the nullspace at equilibrium is not expected to alter the controllability of a multirotor as STLC depends mostly on the geometry of the rotor layout.

For the controllability calculations to follow, it will be convenient to parameterize the rotation matrix using the standard roll, pitch, yaw angles (θ, ϕ, ψ). Note that this parameterization is used only to simplify the bracketing calculations; the dynamics are not being linearized and nonlinear STLC will still be shown using Sussmann's condition. The roll-pitch-yaw kinematics are given by,

$$\begin{pmatrix} \dot{\theta} \\ \dot{\phi} \\ \dot{\psi} \end{pmatrix} = \begin{bmatrix} 0 & \cos(\phi) & -\sin(\phi) \\ 1 & \sin(\phi)\tan(\theta) & \cos(\phi)\tan(\theta) \\ 0 & \sec(\theta)\sin(\phi) & \cos(\phi)\sec(\theta) \end{bmatrix} \omega^b \triangleq \Xi(\theta, \phi, \psi)\omega^b.$$

Under this parameterization the advected parameter γ can be written as,

$$\gamma = \Gamma(\theta, \phi) = \begin{pmatrix} -\sin(\theta) & \cos(\theta)\sin(\phi) & \cos(\theta)\cos(\phi) \end{pmatrix}^T.$$

The drift vector field can then be written as,

$$f(z) = \begin{bmatrix} \vec{p}/M_T \\ \vec{l} \times \Phi^{-1}(\vec{l} - J\langle \mathbf{1}, \varpi \rangle e_3) + \Lambda \varpi^2 \\ \vec{p} \times \Phi^{-1}(\vec{l} - J\langle \mathbf{1}, \varpi \rangle e_3) - g M_T \Gamma(\theta, \phi) + \Psi \varpi^2 \\ \Xi(\theta, \phi, \psi)\Phi^{-1}(\vec{l} - J\langle \mathbf{1}, \varpi \rangle e_3) \\ 0_{n \times 1} \end{bmatrix}.$$

It is assumed that $\dot{\varpi}$ is directly controlled, i.e. $\dot{\varpi} = \vec{u}$. The control vector fields will be chosen to correspond to pure roll, pitch, yaw, and thrust of the vehicle. Recall that the matrix $\begin{bmatrix} \Lambda & c_t \mathbf{1}^T \end{bmatrix}$ maps ϖ^2 to moments in the first three rows and a thrust in the fourth row,

$$\begin{bmatrix} \Lambda \\ c_T \mathbf{1}^T \end{bmatrix} \varpi^2 \triangleq \bar{\Lambda} \varpi^2. \tag{4.33}$$

Taking a time derivative of the right hand side of (4.33) yields,

$$2\bar{\Lambda}\mathrm{diag}(\varpi)\dot{\varpi},$$

which maps rotor accelerations to the time derivatives of the moments and thrust. Motivated by this, four control vector fields are defined by,

$$\mathrm{diag}(\varpi^{-1})\bar{\Lambda}^{\dagger} e_j, \;\; j \in \{1, 2, 3, 4\},$$

where e_j is a standard basis vector in $\mathbb{R}^4$. These four vector fields correspond to the $\bar{\varpi}$ that generate a pure pitch, roll, yaw, and thrust. Of course, when the number of rotors exceeds four, additional control vector fields will be needed that span the nullspace of $\bar{\Lambda}$, but these will not impact the STLC results to follow. Finally, changing the nonholonomic angular momentum to the total angular momentum, $\tilde{l} = \vec{l} - J\langle \mathbf{1}, \varpi \rangle e_3$ (analogous to the coordinate change (4.14) used in analyzing STLC for spherical robots), yields the following system where the state is $z = (d^b, \tilde{l}, \vec{p}, \theta, \phi, \psi, \varpi)$ and,

$$f(z) = \begin{bmatrix} \vec{p}/M_T \\ (\tilde{l} + J\langle \mathbf{1}, \varpi \rangle e_3) \times \Phi^{-1}\tilde{l} + \Lambda \varpi^2 \\ \vec{p} \times \Phi^{-1}\tilde{l} - gM_T\Gamma(\theta, \phi) + \Psi \varpi^2 \\ \Xi(\theta, \phi, \psi)\Phi^{-1}\tilde{l} \\ 0_{2n \times 1} \end{bmatrix} \tag{4.34}$$

is the drift vector field and

$$h_i(z) = \begin{bmatrix} 0_{3\times 1} & -Je_3\langle \varpi^{-1}, \bar{\Lambda}^\dagger e_j \rangle & 0_{3\times 1} & 0_{3\times 1} & \operatorname{diag}(\varpi^{-1})\bar{\Lambda}^\dagger e_j \end{bmatrix}, \ j \in \{1,2,3,4\} \tag{4.35}$$

are the control vector fields. Let $\{h_r, h_p, h_y, h_t\}$ denote the control vector fields corresponding to pure roll, pitch, yaw, and thrust. Before stating the STLC result, two propositions are established to clarify the forthcoming brackets.

Proposition 4.3.1. For a multirotor belonging to the common class (4.3.1),

$$\langle \mathbf{1}, \bar{\Lambda}^\dagger e_j \rangle = 0, \text{ for } \ j \in [1,2,3],$$

and $\langle \mathbf{1}, \bar{\Lambda}^\dagger e_4 \rangle > 0$. This proposition asserts that the sum of the rotor accelerations that produce a roll, pitch, and yaw are zero, while the sum of accelerations that produce a pure thrust is always nonzero.

Proof. The quantity $\langle \mathbf{1}, \bar{\Lambda}^\dagger e_j \rangle = \langle e_j, (\bar{\Lambda}\bar{\Lambda}^T)^{-T}\bar{\Lambda}\mathbf{1} \rangle$. Then, $\bar{\Lambda}\mathbf{1} = \begin{bmatrix} \mathbf{1}^T\Lambda^T & 2nc_T \end{bmatrix}^T$ and

$$\Lambda\mathbf{1} = \sum_{i=1}^{2n}(c_T\sigma_i \times e_3 - c_Q\phi_i e_3) = c_T\Big(\sum_{i=1}^{n}\sigma_i \times e_3 - \sum_{i=1}^{n}\sigma_i \times e_3\Big) - c_Q\sum_{i=1}^{2n}\phi_i e_3 = \vec{0},$$

which follows from the assumptions of (4.3.1). Thus, $\bar{\Lambda}\mathbf{1} = \begin{bmatrix} 0_{1\times 3} & 2nc_T \end{bmatrix}^T$. Using the result that $\Lambda\mathbf{1} = \vec{0}$, one can write,

$$(\bar{\Lambda}\bar{\Lambda}^T)^{-T} = \begin{bmatrix} (\Lambda\Lambda^T)^{-T} & 0_{3\times 1} \\ 0_{1\times 3} & \frac{1}{2nc_T^2} \end{bmatrix}.$$

Finally, $(\bar{\Lambda}\bar{\Lambda}^T)^{-T}\bar{\Lambda}\mathbf{1} = \begin{bmatrix} 0_{1\times 3} & (1/c_T) \end{bmatrix}^T$ and from this the result follows. □

Proposition 4.3.2. For a multirotor vehicle belonging to the common class (4.3.1), evaluated at the equilibrium defined by (4.32), $\langle \varpi^{-1}, \bar{\Lambda}^\dagger e_3 \rangle$ is always nonzero.

Proof. From the definition of $\bar{\Lambda}$, $\langle \varpi^{-1}, \bar{\Lambda}^\dagger e_3 \rangle = \langle \varpi^{-1}, \Lambda^\dagger e_3 \rangle$. Without a loss of generality, group the columns of Λ such that a rotor at σ_i and its reflection at $-\sigma_i$ are represented in adjacent columns, i.e.,

$$\Lambda = \begin{bmatrix} c_T\sigma_1 \times e_3 - c_Q\phi_i e_3 & -c_T\sigma_1 \times e_3 - c_Q\phi_i e_3 & \dots \end{bmatrix}.$$

Recall that the total number of rotors is $2n$ from (4.3.1). When n is odd, rotors that are paired spin in opposite directions and

$$\Lambda\Lambda^T = \begin{bmatrix} 2c_T^2 \sum_{i=1}^n \sigma_{y,i}^2 & -2c_T^2 \sum_{i=1}^n \sigma_{x,i}\sigma_{y,i} & -2c_T c_Q \sum_{i=1}^n \sigma_{y,i} \\ -2c_T^2 \sum_{i=1}^n \sigma_{x,i}\sigma_{y,i} & 2c_T^2 \sum_{i=1}^n \sigma_{x,i}^2 & 2c_T c_Q \sum_{i=1}^n \sigma_{x,i} \\ -2c_T c_Q \sum_{i=1}^n \sigma_{y,i} & 2c_T c_Q \sum_{i=1}^n \sigma_{x,i} & 2nc_Q^2 \end{bmatrix} \triangleq \begin{bmatrix} A & b \\ b^T & c \end{bmatrix}.$$

From this, $(\Lambda\Lambda^T)^{-1}e_3 = \begin{bmatrix} -(1/k)b^T A^{-T} & (1/k) \end{bmatrix}^T$, where $k = c - b^T A^{-1} b$. Using the equilibrium point characterized by (4.32) we can write,

$$(\varpi^{-1})^T\Lambda^T = \frac{2nc_T}{gM_T}\begin{bmatrix} 2c_T \sum_{i=1}^n \sigma_{y,i} & -2c_T \sum_{i=1}^n \sigma_{x,i} & -2nc_Q \end{bmatrix} = \frac{-2nc_T}{gM_T c_Q}\begin{pmatrix} b^T & c \end{pmatrix}.$$

Finally, $\langle \varpi^{-1}, \Lambda^\dagger e_3 \rangle = \frac{-2nc_T}{gM_T c_Q}(1/k)(c - b^T A^{-1} b) = \frac{-2nc_T}{gM_T c_Q}$, and the result follows since each of the values in the fraction are nonzero. When n is even, rotors that are paired spin in the same direction and $(\Lambda\Lambda^T)^{-1}e_3 = \begin{bmatrix} 0 & 0 & 1/(2nc_Q^2) \end{bmatrix}$. One may also write,

$$(\varpi^{-1})^T\Lambda^T = \frac{2nc_T}{gM_T}\begin{bmatrix} 0 & 0 & -2nc_Q \end{bmatrix},$$

such that again $(\varpi^{-1})^T\Lambda^T(\Lambda\Lambda^T)^{-1}e_3 = \frac{-2nc_T}{gM_T c_Q}$, agreeing with the odd n case and establishing the result. □

Sussmann's condition can be used to establish STLC of a dynamical system with bilateral control inputs u_i. When u_i is unilateral, e.g. $u_i > 0$, Sussmann's condition must be augmented with an additional condition to establish STLC [31]. Recall that the dynamic model (4.34)-(4.35) adopted above treats $\dot{\varpi}_i$ as the system inputs. It is physically reasonable to assume that $\dot{\varpi}_i$ can be driven bilaterally when $|\varpi_i| > 0$. Without loss of generality, suppose that the $\varpi_i > 0$. The dynamics of the rotor can be written as,

$$\dot{\varpi}_i = (1/J)(T_d + T_r),$$

where $T_d > 0$ is the drive torque from the motor and $T_r < 0$ is a passive resistive torque due to air damping and the motor's electromotive force (EMF). At equilibrium, $\dot{\varpi}_i = 0$ and therefore $T_d + T_r = 0$. From this point, T_d can be increased such that $\dot{\varpi}_i > 0$. However, if T_d is decreased from its equilibrium value then $T_d + T_r < 0$ and the rotor will decelerate, $\dot{\varpi}_i < 0$. Hence, the passive resistive torque enables $\dot{\varpi}_i$ to be driven bilaterally even though the drive torque is constrained to be positive. This simple fact enables STLC to be established using Sussmann's condition without modification when $\dot{\varpi}_i$ are chosen as the system inputs. In comparison, the standard approach of modeling a multirotor's inputs as the thrust applied by each rotor leads to a more restrictive and complicated application of Sussmann's condition to establish STLC [72].

Theorem 4.3.1 (Common Multirotor Class, STLA)**.** Any multirotor belonging to the common multirotor class (4.3.1) is small-time locally accessible (STLA) from the equilibrium point defined by (4.31)-(4.32).

Proof. To prove this result, it is necessary to show that

$$\overline{Lie}(\{f, h_p, h_r, h_y, h_t, \ldots, h_{2n}\})(q) = T_q Q,$$

from the equilibrium point defined by (4.31)-(4.32), denoted by z^*. First, note that $\{h_p, h_r, h_y, h_t\}$ span four degrees of freedom in the input space $\dot{\varpi}$, and for $2n > 4$ additional control vector fields can be chosen to completely span the input space. Recalling that the coordinates are arranged as $z = (d^b, \tilde{l}, p, \theta, \phi, \psi, \varpi)$, the Lie brackets corresponding to pitch, roll and yaw are

$$[f, h_i]|_{z=z^*} = \begin{bmatrix} \vec{0} & -2e_i & \vec{0} & 0 & 0 & J\Phi_{33}^{-1}\langle \varpi^{-1}, \bar{\Lambda}^\dagger e_i \rangle & \vec{0} \end{bmatrix}, \; i \in [1,2,3].$$

Note that $[f, h_p]$,$[f, h_r]$, and $[f, h_y]$ together span the $\dot{\tilde{l}}$ dimension, and $[f, h_y]$ spans the dimension $\dot{\psi}$ as guaranteed by Proposition (4.3.2). Similarly,

$$[f, h_t]|_{z=z^*} = \begin{bmatrix} \vec{0} & \vec{0} & 0 & 0 & -2c\langle \mathbf{1}, \bar{\Lambda}^\dagger e_4 \rangle & \vec{0} & \vec{0} \end{bmatrix},$$

where the thrust bracket $[f, h_t]$ spans the $\dot{p}_z$ coordinate as guaranteed by Proposition (4.3.1). Looking at the following higher-order brackets,

$$[[f, h_i], f]|_{z=z^*} = \begin{bmatrix} \vec{0} & \vec{0} & \vec{0} & -2\Xi(0,0,\psi)\Phi^{-1}e_i & \vec{0} \end{bmatrix}, \; i \in [1,2],$$

it is observed that $[[f, h_r], f]$ and $[[f, h_p], f]$ span the $\dot{\theta}$ and $\dot{\phi}$ dimensions. Yaw is spanned by a bracket of lower degree than roll and pitch because the inputs $\dot{\varpi}$ are

related to $\dot{\omega}_{b,z}$ kinematically through the connection, whereas the inputs provide a torque that must be integrated to manifest changes in roll or pitch. Similarly,

$$[[f,h_t],f]|_{z=z^*} = \begin{bmatrix} 0 & 0 & \frac{-2c_T}{M_T}\langle \mathbf{1}, \bar{\Lambda}^\dagger e_4 \rangle & \vec{0} & \vec{0} & \vec{0} & \vec{0} \end{bmatrix},$$

spans the $\dot{d}_z^b$ coordinate as guaranteed by Proposition (4.3.1). Looking further at the brackets,

$$[[[f,h_i],f],f]|_{z=z^*} = \begin{bmatrix} \vec{0} & \vec{0} & 2gM_T(e_3 \times \Phi^{-1}e_i) & \vec{0} & \vec{0} \end{bmatrix}, \ i \in [1,2],$$

it is clear that $[[[f,h_r],f],f]$ and $[[[f,h_p],f],f]$ span the $\dot{p}_x$ and $\dot{p}_y$ dimensions. Finally,

$$[[[[f,h_i],f],f],f]|_{z=z^*} = \begin{bmatrix} 2g(e_3 \times \Phi^{-1}e_i) & \vec{0} & \vec{0} & \vec{0} & \vec{0} \end{bmatrix}, \ i \in [1,2],$$

where it is clear that $[[[[f,h_r],f],f],f]$ and $[[[[f,h_p],f],f],f]$ span the dimension $\dot{d}_x^b$ and $\dot{d}_y^b$. The high degree of the brackets necessary to span the $\dot{d}_x^b$ and $\dot{d}_y^b$ dimensions is due to the the fact that the inputs must be integrated four times to cause a change in horizontal position. Together, these Lie brackets span T_qQ at the equilibrium point defined by (4.31)-(4.32) and STLA is established. □

Theorem 4.3.2 (Common Multirotor Class, STLC)**.** Any multirotor belonging to the common multirotor class (4.3.1) is small-time locally controllable (STLC) from the equilibrium point defined by (4.31)-(4.32).

Proof. Note that each of the brackets used to establish STLA in Theorem 4.3.1 are good Lie brackets and that the highest degree used to span T_qQ at the equilibrium point is five. Then, bad brackets of the fifth degree include,

$$\begin{aligned} &[[[[f,h_i],h_i],h_j],h_j], \\ &[[[[f,h_i],h_j],h_i],h_j], \\ &[[[[f,h_i],h_i],h_i],h_i], \ \ i,j \in [1,2,3,4], \ \ i \neq j, \end{aligned}$$

and each of these brackets is zero except for a potentially nonzero component along the ψ coordinate, which can be annihilated with the good, degree two bracket $[f,h_y]$. In addition, the bad brackets $[[[[f,h_i],f],f],h_i], \ i \in [1,2,3,4]$ and their permutations are zero along the components $\dot{d}_x^b$ and $\dot{d}_y^b$, and thus can be spanned by the good Lie brackets that are less than degree five in Theorem 4.3.1. All other bad brackets of the fifth degree can be written from the fifth degree brackets already mentioned. Hence, all bad fifth degree brackets can be written in terms

of the good Lie brackets of Theorem 4.3.1, which have a smaller degree. There are no bad fourth degree brackets. All bad third degree brackets can be written as $[[f,h_i],h_i],\ \forall i = [1,2,3,4]$, and these brackets may have a nonvanishing entry along the ψ coordinate, which can be neutralized by the degree two bracket $[f,h_y]$. Thus, all bad brackets of degree $k \leq 5$ can be written in terms of good Lie brackets of degree $j \leq k$ and by Sussmann's condition STLC is established for the common multirotor class (4.3.1) at the equilibrium point defined by (4.31)-(4.32). □

In this chapter, the dynamics of spherical vehicles were developed and small-time local controllability (STLC) conditions were established for these vehicles on flat, sloped, and undulating terrain. This chapter introduced the central role played by the steering matrix, which can be obtained from the nonholonomic connection. The steering matrix can be determined from inspection of the Lagrangian and the necessary STLC conditions depend on the steering matrix's surjectivity. Several examples demonstrated the use of these conditions, including Moball on the plane and a rotor-controlled vehicle on a helicoid. In addition, STLC conditions were developed for a class of common multirotor aerial vehicles to show how the dynamics approach of Chapter 3 enables insight into the controllability of a larger class of relevant robotic systems.

Chapter 5

MOBALL CONTROL, PLANNING, SIMULATION

In this chapter, a simulation environment, control architecture, and motion planning scheme are introduced for the Moball. Although the focus of this chapter is specific to the Moball system, many of this chapter's techniques are applicable to the larger class of barycentric spherical robots (BSRs). For example, when a BSR's equations of motion are derived using the reduction and reconstruction scheme of Chapter 3, a geometric integration scheme detailed in this chapter can be employed on the Lie algebra that obviates the need to integrate on $SO(3)$ (which accumulates greater error due to the necessary renormalization of rotation matrices between integration steps). All BSRs may also benefit from the feedback controllers that enable Moball to follow a desired trajectory on generic terrains. Furthermore, a simple motion-planning scheme is introduced that selects a path through a generic terrain that maximizes the vehicle's exposure to external wind fields while satisfying scientific objectives and avoiding environmental hazards; this motion planner is applicable to any spherical vehicle that relies on energy-harvesting to prolong mission life.

First, this chapter introduces the simulation environment, including a Lie algebra integrator and the framework for modeling three-dimensional terrain. Moball's control architecture is then reviewed and two feedback controllers, which are broadly applicable to all BSRs, are introduced. Next, a "ballistic-impulse" magnet position controller and feedforward path controller are demonstrated for Moball. Finally, a motion planning framework is introduced for energy-harvesting spherical vehicles.

5.1 Simulation Environment

The simulation environment used to analyze the Moball consists of the vehicle's dynamical equations of motion[1], a geometric numerical integrator, and a generic terrain model. Each of these key components are now introduced.

[1] Moball's dynamics were introduced in Chapter 3

5.1.1 Geometric Numerical Integration & Adaptive Step-Sizing

Although Moball's dynamics have been reduced and reconstructed in (4.30) using the method of Chapter 3, the rotational kinematics,

$$\dot{R} = R\hat{\omega}^b, \quad t \geq t_0, \quad R(t_0) \in SO(3), \tag{5.1}$$

must be integrated to reconstruct the vehicle's orientation for the purposes of simulation and control. As the integration takes place on $SO(3)$, the solution is required to remain in this Lie group throughout the integration. However, standard integration techniques like Runge-Kutta methods will not satisfy this requirement because $SO(3)$ is a non-Euclidean space, which is not closed under addition. In fact, any integration scheme that propogates the solution forward using addition will fail this requirement and induce unacceptable error into the solution over long time spans. Geometric numerical integration techniques are methods that preserve the geometric properties of the flow of a differential equation [33]. Since (5.1) is a differential equation on a Lie group, it is natural to employ an integration scheme that occurs on the Lie algebra, and that propogates the solution forward using the exponential rather than addition. This is the basis for the Runge-Kutta Munthe-Kaas (RKMK) method.

Definition 5.1.1 (Differential of Exponential [39])**.** The differential of the exponential map is defined as the left-trivialized tangent of the exponential map, i.e. $\text{dexp} : \mathfrak{g} \times \mathfrak{g} \to \mathfrak{g}$ such that,

$$\frac{d}{dt}\exp(A(t)) = \exp(A(t))\text{dexp}_{-A(t)}(\dot{A}(t)),$$

where $\text{dexp}_{-A}(C)$ can be expressed as an analytical function,

$$\text{dexp}_{-A}(C) = \sum_{j=0}^{\infty} \frac{1}{(j+1)!}\text{ad}^j_{-A}C,$$

where the ad operator was defined in Section (2.4). For the Lie algebra $\mathfrak{so}(3)$, this analytical function can be used to explicitly define two key relationships,

$$\text{dexp}_x = I + \frac{\sin^2(\vartheta)}{2\vartheta^2}\hat{x} + \frac{\theta - \sin(\theta)}{\theta^3}\hat{x}^2,$$
$$\text{dexp}_x^{-1} = I - \frac{1}{2}\hat{x} - \frac{\theta\cot(\vartheta) - 2}{2\theta^2}\hat{x}^2$$

where $x \in \mathfrak{so}(3)$ is represented as a vector in $\mathbb{R}^3$, $\theta = ||x||$ and $\vartheta = (\theta/2)$.

The following proposition underlies the RKMK method and its application to Moball.

Proposition 5.1.1 ([39])**.** For small $t \geq t_0$, the solution to (5.1) is given by,

$$R(t) = R_0 \exp(\Theta(t)),$$

where $\Theta(t) \in \mathfrak{so}(3)$ satisfies the differential equation,

$$\dot{\Theta}(t) = \mathrm{dexp}^{-1}_{-\Theta(t)}(\hat{\omega}^b), \quad \Theta(t_0) = 0. \tag{5.2}$$

Proposition (5.1.1) establishes that the differential equation (5.1) can be solved by integrating (5.2), which is a differential equation defined over $\mathfrak{so}(3)$. The Lie algebra $\mathfrak{so}(3)$ is a vector space that *is* closed under addition, allowing standard Runge-Kutta methods to be employed on (5.2). The solution is then reconstructed via exponentiation. Suppose that $\hat{\omega}^b(R)$ is a function solely of $R \in SO(3)$. Then, the RKMK algorithm propogates $R_n \in SO(3)$ to $R_{n+1} \in SO(3)$ using a ν-stage Runge-Kutta method as follows,

$$\begin{aligned}
\Theta_k &= \sum_{l=1}^{\nu} a_{k,l} F_l, \\
\hat{\omega}^b_k &= h\hat{\omega}^b(R_n \exp(\Theta_k)), \\
F_k &= \mathrm{dexp}^{-1}_{-\Theta_k}(\hat{\omega}^b_k), \\
\Theta &= \sum_{l=1}^{\nu} b_l F_l, \\
R_{n+1} &= R_n \exp(\Theta),
\end{aligned} \tag{5.3}$$

where $k \in [1, \ldots, \nu]$, h is the timestep, and $\{a_{k,l}, b_l\}$ are the constants defining the underlying Runge-Kutta integration method. With the analytical expression of dexp^{-1}_x in (5.1.1), the RKMK method has the same order as the underlying Runge-Kutta method. A fourth-order Runge-Kutta method is employed in practice, which differs from (5.3) only in that ω^b is coupled to momenta, and Moball's magnet positions, and magnet velocities.

Previous experiments with a Moball prototype, discussed in Appendix A, demonstrated that placing linear springs at the ends of Moball's inner tubes increased the range of rotational speeds over which the vehicle can harvest energy. Consequently, the magnet dynamics are stiff; the magnet's trajectory qualitatively and abruptly changes as it contacts the linear spring. To cope with the magnet's stiff dynamics, an adaptive step-size algorithm is combined with the RKMK method described above. The adaptive step follows from an embedded Runge-Kutta method.

Symbol	Value
$\{a_{ij}\}$	$\begin{bmatrix} 0 & 0 & 0 & 0 & 0 \\ 1/5 & 0 & 0 & 0 & 0 \\ 3/40 & 9/40 & 0 & 0 & 0 \\ 3/10 & -9/10 & 6/5 & 0 & 0 \\ -11/54 & 5/2 & -70/27 & 35/27 & 0 \\ 1631/55296 & 175/512 & 575/13824 & 44275/110592 & 253/4096 \end{bmatrix}$
$\{c_i\}, O(h^6)$	$\begin{bmatrix} 37/378 & 0 & 250/621 & 125/594 & 0 & 512/1771 \end{bmatrix}$
$\{c_i^*\}, O(h^5)$	$\begin{bmatrix} 2825/27648 & 0 & 18575/48384 & 13525/55296 & 277/14336 & 1/4 \end{bmatrix}$

Table 5.1: Adaptive Runge-Kutta Coefficients

Consider the dynamical equation $\dot{y} = f(t, y)$. In this adaptive integration method, the value of the variable y at time t_{n+1} is derived from y_n using two different Runge-Kutta integrators. Each Runge-Kutta integrator uses the same intermediate dynamic function evaluations, $k_i = f(t_i, y_i)$, but with differing coefficients. The specific coefficients chosen ensure that the integrators have differing orders of accuracy [69], e.g.

$$y_{n+1} = y_n + \sum_{i=1}^{6} c_i k_i + O(h^6), \quad y^*_{n+1} = y_n + \sum_{i=1}^{6} c^*_i k_i + O(h^5),$$

where $\left(\{c_i\}_{i=1}^6, y_{n+1}\right)$ and $\left(\{c_i^*\}_{i=1}^6, y^*_{n+1}\right)$ are a fifth and fourth-order approximation, respectively, and k_i are the variable's dynamics, $f(t, y)$, evaluated at intermediate points within $[t_n, t_{n+1}]$. Only specific sets of coefficients $\{c_i\}_{i=1}^6$ and $\{c_i^*\}_{i=1}^6$ enable this method; the coefficients [20] used in our application are displayed in Table 5.1.

The solution y_{n+1} is used to assess the accuracy of the solution y^*_{n+1}. An error estimate is defined as $\Delta \triangleq y_{n+1} - y^*_{n+1}$, and the step length, h, is adjusted based on this error. In this application, adaptive step-sizing occurs on the magnet's position and the error, Δ, is taken to be the maximum across all of the vector components of $\mathcal{X}$. Then, the step-size is adapted according to,

$$h_2 = h_1 |\Delta_0 / \Delta|^c,$$

where h_1 and h_2 are the initial and final step-sizes, Δ_0 is the desired accuracy, and Δ is the measured error [69]. This adaptive scheme can increase or decrease the step-size until the desired accuracy Δ_0 is achieved, and then the fourth-order approximation y^*_{n+1} is adopted. In our application, this adaptive scheme automatically changes the step size in the RKMK algorithm (5.3) based on the stiffness of the magnet dynamics.

5.1.2 Modeling Three-Dimensional Terrain

Terrain was modeled as a regular surface while deriving the dynamical equations of motion of a spherical vehicle over undulating terrain in Subsection (4.2.5). The surface adopted in simulation is based on the Bicubic B-spline Patch (BBP) [73]. A BBP is a two-dimensional surface that is a cubic interpolation between a 4×4 grid of *control points*. Each control point, $P_{ij} \in \mathbb{R}^3$, is specified by the user. The surface's coordinates are then defined by,

$$P_i(u,w) = \left(\frac{1}{6}\right)^2 \begin{pmatrix} u^3 \\ u^2 \\ u \\ 1 \end{pmatrix}^T M P^i M^T \begin{pmatrix} w^3 \\ w^2 \\ w \\ 1 \end{pmatrix}, \quad i \in \{x,y,z\}, \tag{5.4}$$

where $M \in \mathbb{R}^{4\times4}$ is a matrix of interpolation coefficients that ensure that the surface is C^2 continuous [73], $(u,w) \in \mathbb{R}^2$ are coordinates of the surface's preimage, and $P^i \in \mathbb{R}^{4\times4}$ is a matrix containing the $\{x,y,z\}$ coordinates of the control points P_{ij}. Uniformly spaced control points were chosen, and the user selects the P_{ij} to emulate hills and valleys. Larger terrains are constructed by combining individual BBP patches. Efficient algorithms are readily available to fit BBP surfaces to point clouds. Therefore, modeling terrain using BBPs is advantageous for planetary science missions, since realistic terrains can be reconstructed from topographical measurements taken from satellites or aircraft.

In Subsection (4.2.5), the allowable directions of motion were chosen based on the normalized Gauss frame $R^T \begin{pmatrix} \frac{\varphi_u}{||\varphi_u||} & \frac{\varphi_v}{||\varphi_v||} & n \end{pmatrix}$. There is always a chart such that $\langle \varphi_u, \varphi_v \rangle = 0$ for regular surfaces, which makes the normalized Gauss frame particularly convenient [19]. However, normalizing (5.4) for every patch is cumbersome. Instead of using the normalized Gauss frame to define the allowable directions of motion, the directions $\begin{pmatrix} \frac{\varphi_u}{||\varphi_u||} & n \times \frac{\varphi_u}{||\varphi_u||} & n \end{pmatrix}$ are used in simulation, which is more convenient as this frame remains orthogonal as the vehicle travels across multiple BBP patches. The derivatives of these directions are computed numerically and the momentum equations possess the same form as those in (4.27).

Fig. 5.1 shows Moball rolling uncontrolled (i.e. the magnets move freely due to the noninertial and gravitational forces) over undulating terrain modeled using BBP patches. In Fig. 5.1a, the heatmap denotes heights and depths. Each hill and depression is approximately $1m$ tall or deep, which is equal to the ball's radius. Over time, air damping causes the ball to settle at the center of the valley in Fig. 5.1a.

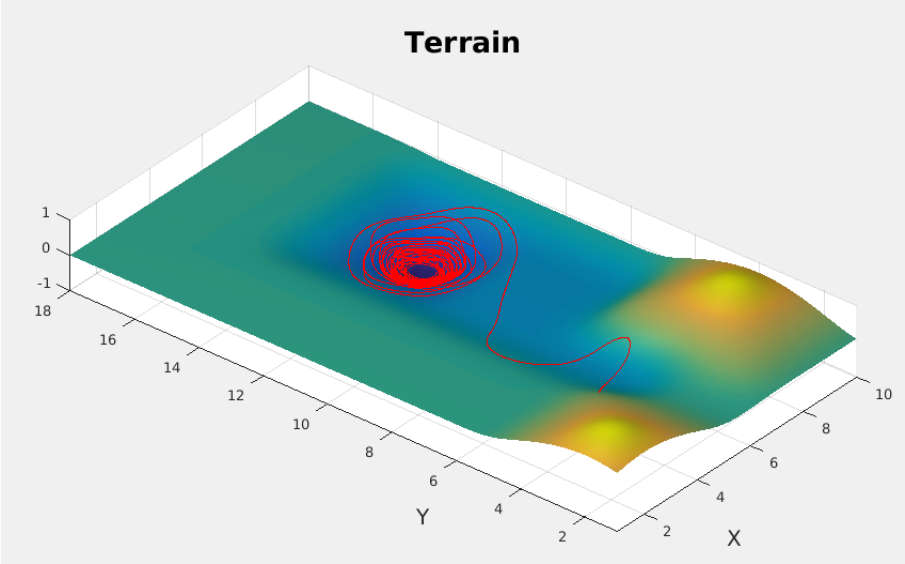

(a) Path of Moball Rolling in Generic Undulating Terrain

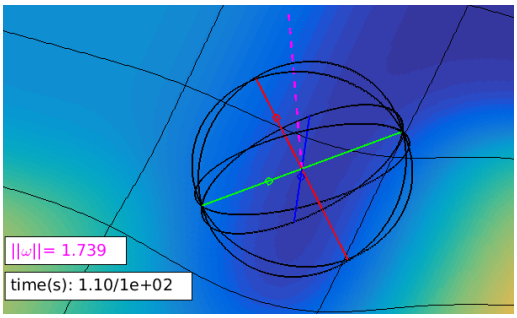

(b) Moball Between Two 1m Tall Hills

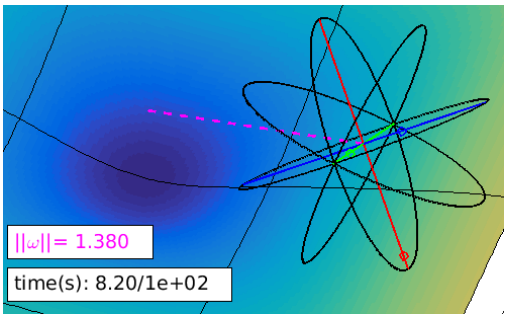

(c) Moball in Local Depression

Figure 5.1: Moball Rolling on Generic B-Spline Terrain. Moball is shown as a wireframe, $\{x, y, z\}$ magnets are along $\{r, g, b\}$ axes, and the surface is colored according to height.

Figs. 5.1b and 5.1c show screenshots of the vehicle travelling along its trajectory. Moball's $\{x, y, z\}$ magnets are depicted as circles moving along $\{r, g, b\}$ axes, and the instantaneous axis of rotation is depicted as a dashed magenta line.

5.2 Moball's Control Architecture

Moball's control architecture is depicted in Fig. 5.2. Moball utilizes a two degree of freedom controller [9], whereby a feedforward controller generates open-loop magnet positions and a feedback controller compensates for errors. The feedforward controller solves a finite-dimensional optimal control problem using a simplified, low-order dynamical model of Moball. A feedback controller corrects for inaccuracies in the low-order system used by the feedforward controller and any unmodeled

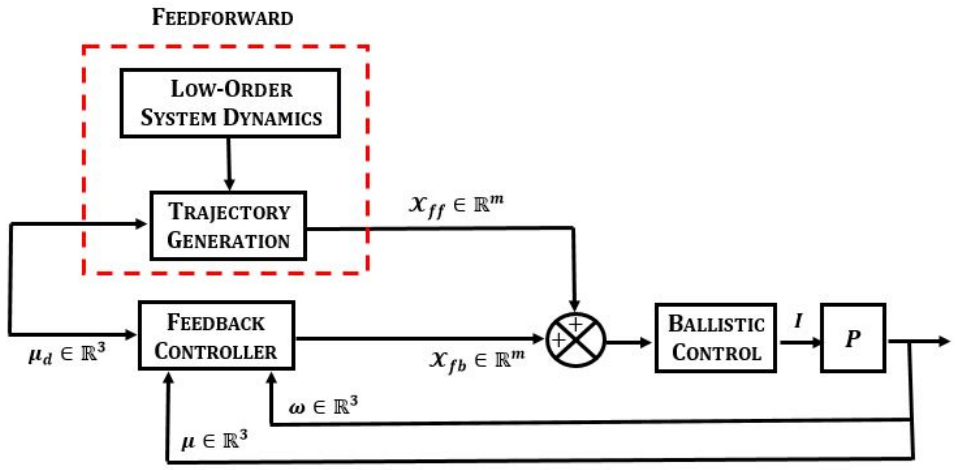

Figure 5.2: Moball's Control Architecture.

disturbances such as wind gusts[2].

As described in Appendix A, sufficient control authority over Moball's magnets is only possible in a small neighborhood about each solenoid. The feedback and feedforward controllers, however, are designed assuming continous control authority along the length of each of Moball's inner tubes. An algorithm is required to map the idealized trajectories of Moball's controllers to a trajectory that is physically possible given the electrodynamics of Moball's actuators. A "ballistic control" scheme is introduced that applies a discrete impulse to a magnet as it passes a solenoid. The magnitude of the impulse is chosen to minimize the tracking error between the idealized and actual magnet trajectory. In this way, the idealized magnet trajectories are approximated.

5.3 Path-Following Feedback Controllers for BSRs

Two feedback controllers are introduced in this section that are applicable to generic BSRs operating on flat or undulating terrains. Each feedback controller is intended to stabilize the vehicle about a desired trajectory, $\mu^s(t) \in \mathbb{R}^3$, defined with respect to an inertial frame. The first controller employs feedback linearization to express the trajectory error dynamics in a standard second-order form, which is then stabilized via pole placement. The second controller uses a cascaded PID structure that directly assigns the vehicle's COM to rectify trajectory errors. Both controllers are validated in simulation.

[2]Ambient air drag *is* modeled in the low-order system dynamics used by the feedforward controller

First, a feedback linearized controller applied to a generic BSR rolling on a flat plane is introduced. Let the path error be defined as

$$\delta(t) \triangleq d^s(t) - \mu^s(t), \tag{5.5}$$

where $d^s(t) \in \mathbb{R}^3$ denotes the position of the BSR's center of rotation , expressed in an inertial frame. The following controller stabilizes the trajectory error dynamics.

Proposition 5.3.1 (Feedback Linearized Controller, Flat Plane)**.** The torque T^c, expressed in a body-fixed frame, stabilizes the trajectory error dynamics of a generic BSR rolling on a flat plane, for (K_p, K_d) chosen via pole placement:

$$T^c = \omega^b \times \mathcal{I}\omega^b + \dot{\mathcal{I}}\omega^b + \mathcal{I}\left(\left(\frac{K_p\delta_2 + K_d\dot{\delta}_2 - \ddot{\mu}_2^s}{r_b}\right)\alpha + \left(\frac{\ddot{\mu}_1^s - K_p\delta_1 - K_d\dot{\delta}_1}{r_b}\right)\beta\right),$$

where $(\mathcal{I}, \omega^b)$ denote the vehicle's inertia tensor and angular velocity expressed in a body-fixed frame, r_b denotes the vehicle's radius, and $\alpha \triangleq R^T e_1$, $\beta \triangleq R^T e_2$.

Proof. Via Euler's equations one may write,

$$\dot{\omega}^b = \mathcal{I}^{-1}(T - \omega^b \times \mathcal{I}\omega^b - \dot{\mathcal{I}}\omega^b),$$

where in general $\dot{\mathcal{I}} \neq 0$ due to the internal actuators within a BSR. Adopting the torque defined in Proposition (5.3.1) leads to,

$$\dot{\omega}^b = \left(\frac{K_p\delta_2 + K_d\dot{\delta}_2 - \ddot{\mu}_2^s}{r_b}\right)\alpha + \left(\frac{\ddot{\mu}_1^s - K_p\delta_1 - K_d\dot{\delta}_1}{r_b}\right)\beta.$$

Taking the time-derivative of the no-slip constraints expressed in an inertial frame yields $\ddot{d}^s = r_b\dot{\omega}^s \times e_3$. Using the relationship $\dot{\omega}^s = R\dot{\omega}^b$, one may write,

$$\ddot{d}^s = \left(\ddot{\mu}_1^s - K_p\delta_1 - K_d\dot{\delta}_1\right)e_1 - \left(K_p\delta_2 + K_d\dot{\delta}_2 - \ddot{\mu}_2^s\right)e_2,$$

where e_i is a standard basis vector of $\mathbb{R}^3$. Recalling the definition of the trajectory error, $\delta(t)$, and decomposing $\ddot{\delta}(t)$ along its first and second components yields,

$$\begin{pmatrix}\ddot{\delta}_1\\ \ddot{\delta}_2\end{pmatrix} = \begin{pmatrix}-K_p\delta_1 - K_d\dot{\delta}_1\\ -K_p\delta_2 - K_d\dot{\delta}_2\end{pmatrix}.$$

The trajectory error dynamics are in a standard second-order form and (K_p, K_d) may be chosen to satisfy a desired percent overshoot and settling time that will stabilize the system. Analyzing the error dynamics along the dimension e_3 is unnecessary as the no-slip constraints prevent the error from changing along this dimension. □

Although Proposition (5.3.1) defines the torque applied to the BSR, the actuator trajectories to realize this torque depend on the vehicle. A map relating the actuator states to the resulting torque must be derived for each vehicle. For example, if Moball's COM lies within a horizontal plane centered at the COR, then,

$$\mathcal{X}(t) = \frac{1}{M_i g} T^c(t) \times \gamma(t), \tag{5.6}$$

where $\gamma(t) = R^T(t)e_3$, M_i is the magnet's mass, and $\mathcal{X}(t)$ are the magnet positions. Moball's magnet dynamics can then be feedback linearized to track the desired magnet locations $\mathcal{X}(t)$, as is done in the following simulations.

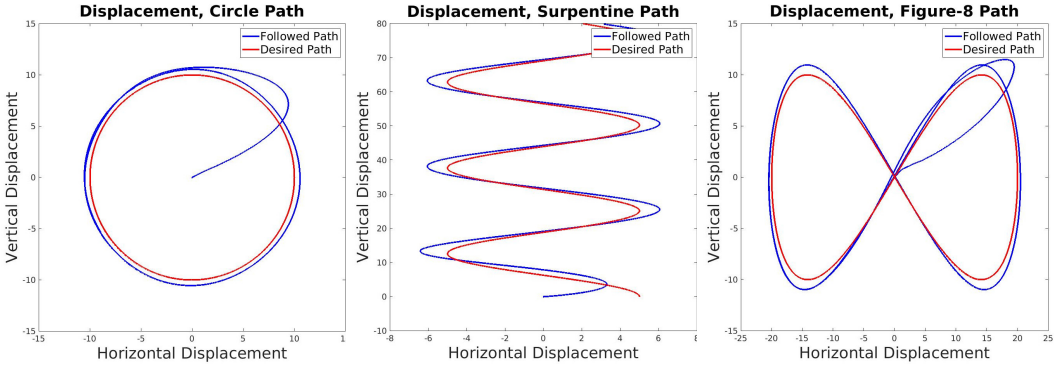

(a) Circle: $\mu^s(t) = 10\begin{pmatrix}\cos(t/20)\\ \sin(t/20))\end{pmatrix}$.

(b) Serpentine: $\mu^s(t) = \begin{pmatrix}5\cos(t/10)\\ 0.4t\end{pmatrix}$.

(c) Figure Eight: $\mu^s(t) = \begin{pmatrix}20\cos(t/30)\\ 10\sin(t/15)\end{pmatrix}$

Figure 5.3: Feedback Linearized Control of Moball on Quickly Varying Paths.

Fig. 5.3 demonstrates the feedback linearized controller from Proposition (5.3.1) guiding Moball along several trajectories on the plane. A circle, serpentine, and figure eight path are tracked in Fig. 5.3. The feedback gains (K_p, K_d) were chosen such that the error dynamics converge to $\delta = 0$ with a settling time of $15s$ and 5% overshoot. The steady state error was less than $1m$, $1.2m$, and $1.3m$ for the circle, figure eight, and serpentine trajectories respectively. The controller of Proposition (5.3.1) is generic and can be applied to solve common control tasks on the plane such as holding a position or following complex trajectories as shown in Fig. 5.3.

Suppose that a moving frame, $E_m = \{T, B, N\}$, is defined on an undulating surface, where T is tangent to the surface, N is the surface normal, and B is the binormal that completes the orthgonal frame. The frame's bases are described with respect to an inertial frame and E_m is centered at the BSR's point of contact with the terrain. Without loss of generality, let $T = \varphi_u/||\varphi_u||$, where $\varphi(u,v) : U \subset \mathbb{R}^2 \to \mathbb{R}^3$ denotes

the map from the surface's two-dimensional pre-image to its embedding in $\mathbb{R}^3$, as described in Subsection (4.1.2). Instead of defining the path trajectory error as in Proposition (5.3.1), let the path error be defined as:

$$\delta = \begin{pmatrix} u \\ v \end{pmatrix} - \begin{pmatrix} \bar{u} \\ \bar{v} \end{pmatrix}, \tag{5.7}$$

where (u, v) and $(\bar{u}, \bar{v})$ denote the contact point and the desired trajectory pulled back to the terrain's pre-image.

Proposition 5.3.2 (Feedback Linearized Controller, Undulating Terrain)**.** The torque T^c, expressed in a body-fixed frame, stabilizes the trajectory error dynamics of a generic BSR rolling on undulating terrain, for (K_p, K_d) chosen via pole placement:

$$T^c = \omega^b \times \mathcal{I}\omega^b + \dot{\mathcal{I}}\omega^b + \mathcal{I}\left(\nu_T t + \nu_B b\right),$$

where (t, b) are the tangent and binormal vectors viewed in a body-fixed frame and (ν_T, ν_N) are chosen to be,

$$\begin{pmatrix} \nu_T \\ \nu_B \end{pmatrix} = \frac{1}{r_b}\left(\nabla(\varphi + r_b N)^\dagger \begin{bmatrix} -B & T \end{bmatrix}\right)^{-1}\left(- K_p\delta - K_d\dot{\delta} + \frac{d^2}{dt^2}\begin{pmatrix} \bar{u} \\ \bar{v} \end{pmatrix}\right),$$

where $(\cdot)^\dagger$ denotes the matrix pseudoinverse.

Proof. Similar to Proposition (5.3.1)'s proof, substituting T_c from Proposition (5.3.2) into Euler's equations yields,

$$\dot{\omega}^b = \nu_T t + \nu_B b. \tag{5.8}$$

Taking a time-derivative of the no-slip constraints in spatial coordinates yields,

$$\ddot{d}^s = \dot{\omega}^s \times N + \omega^s \times \dot{N}. \tag{5.9}$$

However, recall that $\varphi + r_b N = d^s$ such that,

$$\frac{d}{dt}(\varphi + r_b N) = \nabla(\varphi + r_b N) \cdot \begin{pmatrix} \dot{u} \\ \dot{v} \end{pmatrix} = r_b \omega^s \times N. \tag{5.10}$$

Taking the derivative of (5.10) yields,

$$\frac{d}{dt}\Big(\nabla(\varphi + r_b N)\Big) \cdot \begin{pmatrix} \dot{u} \\ \dot{v} \end{pmatrix} + \nabla(\varphi + r_b N)\begin{pmatrix} \ddot{u} \\ \ddot{v} \end{pmatrix} = r_b \dot{\omega}^s \times N + r_b \omega^s \times \dot{N}.$$

One may show that $\frac{d}{dt}(\nabla(\varphi + r_b N)) = \nabla(\frac{d}{dt}(\varphi + r_b N))$ and from Equation (5.10), $\frac{d}{dt}(\varphi + r_b N) = r_b \omega^s \times N$. Thus, the derivative of (5.10) can be expressed as,

$$\nabla(r_b \omega^s \times N) \cdot \begin{pmatrix} \dot{u} \\ \dot{v} \end{pmatrix} + \nabla(\varphi + r_b N) \begin{pmatrix} \ddot{u} \\ \ddot{v} \end{pmatrix} = r_b \dot{\omega}^s \times N + r_b \omega^s \times \dot{N}. \tag{5.11}$$

However, $\nabla(r_b \omega^s \times N) = r_b \hat{\omega}^s \nabla N$ and $\dot{N} = \nabla N \cdot \begin{pmatrix} \dot{u} & \dot{v} \end{pmatrix}^T$. Equation (5.11) can then be written as,

$$\begin{pmatrix} \ddot{u} \\ \ddot{v} \end{pmatrix} = r_b \Big(\nabla(\varphi + r_b N) \Big)^\dagger \dot{\omega}^s \times N.$$

Substituting $\dot{\omega}^s$ using Equation (5.8) into the above yields,

$$\begin{pmatrix} \ddot{u} \\ \ddot{v} \end{pmatrix} = r_b \Big(\nabla(\varphi + r_b N) \Big)^\dagger \begin{bmatrix} -B & T \end{bmatrix} \begin{pmatrix} \nu_T \\ \nu_B \end{pmatrix}.$$

By adopting the values of (ν_T, ν_B) in Proposition (5.3.2), the error dynamics are found to have the form $\ddot{\delta} = -K_p \delta - K_d \dot{\delta}$. Invertibility of the matrix $\nabla(\varphi + r_b N)^\dagger [\, -B \;\; T \,]$ follows from the regularity of φ and the linear independence of B and T. Choosing (K_p, K_d) via pole placement to satisfy a desired percent overshoot and settling time stabilizes the trajectory error dynamics. □

Mapping a body torque to the necessary actuator positions is more complicated on undulating terrain due to the additional torque due to gravity acting on the vehicle's COR. When Moball's magnets are constrained to lie in a plane orthogonal to gravity and centered at the vehicle's COR, this relationship becomes:

$$\mathcal{X}(t) = \frac{1}{M_i g} T^c(t) \times \gamma(t) + \frac{M_T r_b}{M_i} \gamma(t) \times (\gamma(t) \times n(t)), \tag{5.12}$$

where M_T is the total system mass, $\gamma(t) = R^T e_3$, and $n(t)$ is the surface normal at the point of contact viewed in a body-fixed frame. Added to the desired magnet position (5.6) is a term needed to cancel the disturbance torque due to gravity's affect on the vehicle's structure; this term exposes the importance of the relative ratio of the actuator mass and total mass.

Fig. 5.4 shows the controller introduced in Proposition (5.3.2) stabilizing Moball about a circular path on a hill of various heights. The magnet position needed to compensate gravity's torque in Eq. (5.12) is dependent on the relative fraction between Moball's total mass and magnet mass, as well as the surface inclination. If Moball's magnets weigh less or the surface is steeper, then the magnets will need

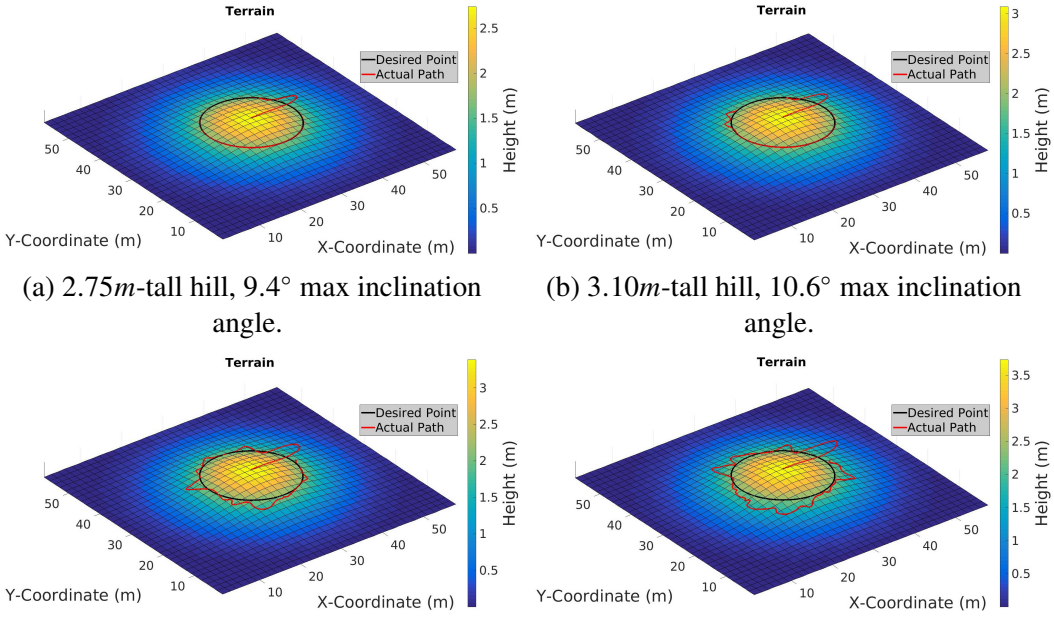

(a) 2.75m-tall hill, 9.4° max inclination angle.

(b) 3.10m-tall hill, 10.6° max inclination angle.

(c) 3.40m-tall hill, 11.6° max inclination angle.

(d) 3.75m-tall hill, 12.8° max inclination angle.

Figure 5.4: Moball Tracking Circular Path on Hills of Various Height.

to be moved further to compensate for the disturbance torque due to gravity. In Fig. 5.4, Moball tracks a circular path centered about the hill's peak[3]. The hills have a height varying from 2.75m-3.75m and maximum angles of inclination ranging from 9.4°-12.8°. Moball is initially centered on the hill's peak and the simulation is run for one revolution about the hill. The controller's tracking error increases with the inclination angle of the surface. A similar decrease in performance would occur if the vehicle's magnet mass was decreased or its structure mass increased. One may use the condition for static equilibrium, Eq. (4.22), as a conservative estimate of the surface slopes a BSR may be able to traverse. In general, steeper terrains can be navigated as the actuator mass increases relative to the vehicle's total mass.

An interesting application of the feedback controller introduced in Proposition (5.3.2) is shown in Fig. 5.5. A common concern of fielded spherical robots is that the vehicle may become trapped in a local depression like a crater or gully. In Fig. 5.5, the controller in Proposition (5.3.2) is used to build up momentum, which enables Moball to escape from a crater that it otherwise would be trapped in. In Fig. 5.5a, a 3m deep crater is simulated and a point outside the crater is the goal. The Moball has a magnet mass of 1.5kg and a structure mass of 20kg, which are close to the

[3]The simulated Moball has a radius $r_b = 1m$, magnet mass, $M_i = 4kg$, and structure mass $M_s = 10kg$. The path being followed is parameterized as $\mu^s(t) = (10\cos(t/40), 10\sin(t/40))$.

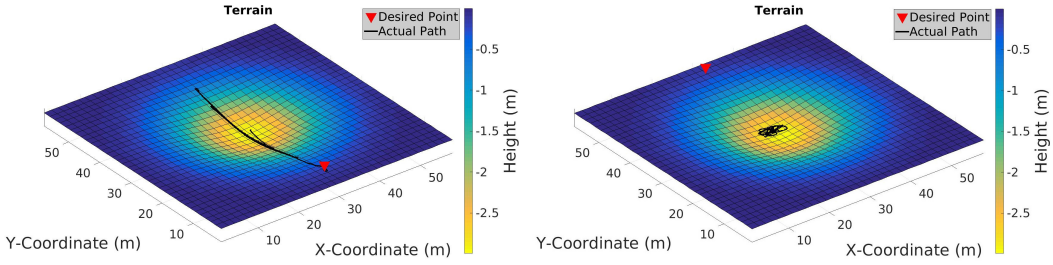

(a) Rocking Back and Forth to Successfully Exit a Crater.

(b) A Direct Attempt to Reach the Desired Point Fails.

Figure 5.5: Feedback Controller "Rocking" a BSR Out of a Crater.

masses of the next Moball prototype. The trace of the vehicle's contact point is shown in black in Fig. 5.5a. The controller works by setting $\mu^s(t)$ to a constant value denoted by the red triangle, which causes Moball to roll towards the desired point. Eventually, the vehicle stops due to the steepness of the crater. At this point, the set point $\mu^s(t)$ is reflected to the other side of the crater and Moball accelerates in the opposite direction, making its way further up the crater wall than the previous attempt. Once the vehicle comes to rest on the opposite side of the crater, $\mu^s(t)$ is reflected again and the process continues until the vehicle escapes the crater. Fig. 5.5b shows the contact path when $\mu^s(t)$ is held constant throughout the simulation; in this case the vehicle does not have sufficient torque to scale the crater wall. The build up of momentum is key to escaping local depressions and the feedback linearizing controller of Proposition (5.3.2) is general enough to enable these maneuvers as well as many others.

A PID controller is now introduced to stabilize a BSR about a desired trajectory. This controller directly manipulates the vehicle's COM as a function of trajectory errors. Understanding how errors contribute to control actions is particularly intuitive. Consider a BSR rolling on the plane as in Fig. 5.6. Frame $E = \{e_1, e_2, e_3\}$ is fixed to the plane and frame $H = \{h_1, h_2, h_3\}$ is a *hybrid* frame, aligned with frame E but anchored to the BSR's center of rotation. The controller outputs the position of the actuator's center of mass, i.e. the center of mass of Moball's magnets is produced. The actuator's COM lies in the $\{h_1, h_2\}$ plane by construction, although this could be offset by any fixed height from the h_3 axis.

The feedback controller takes a cascaded form, with an outer loop regulating the vehicle's rotational velocity and an inner loop controlling the position of the actuator's COM. Let the path error be denoted by $\delta(t)$, as defined in Equation (5.5). The

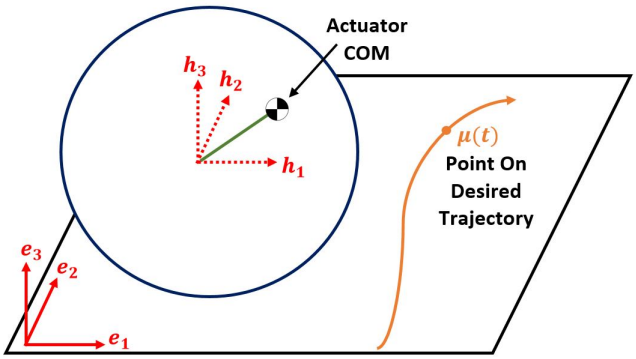

Figure 5.6: Path-Following Feedback Controller for Generic BSR.

outer loop generates a desired angular velocity through a simple PID controller,

$$\bar{\omega}^s(t) = \left(K_p^\omega \delta + K_i^\omega \int \delta \cdot dt + K_d^\omega \dot{\delta}\right) \times e_3, \tag{5.13}$$

where $(K_p^\omega, K_d^\omega, K_i^\omega)$ are PID gains. With a constant error δ, the direction of $\bar{\omega}^s(t)$ guides the vehicle to $\mu^s(t)$. From the desired angular velocity, $\bar{\omega}^s(t)$, the angular velocity error is defined as,

$$e_\omega(t) = \omega^s(t) - \bar{\omega}^s(t), \tag{5.14}$$

where $\omega^s(t)$ is the vehicle's current angular velocity expressed in an inertial frame. The inner loop generates the desired position of the actuator's COM via,

$$\mathcal{X}_{COM} = e_3 \times \left(K_p^\mathcal{X} e_\omega + K_i^\mathcal{X} \int e_\omega \cdot dt + K_d^\mathcal{X} \dot{e}_\omega\right), \tag{5.15}$$

where again $(K_p^\mathcal{X}, K_i^\mathcal{X}, K_d^\mathcal{X})$ are PID gains. With a constant angular velocity error e_ω, the inner loop calculates the COM position that produces a torque to reach to the desired trajectory $\mu^s(t)$. The mapping between $\mathcal{X}_{COM}$ and actuator positions is vehicle specific, e.g. for Moball as described in Subsection (4.3.1), the map between the actuator's COM location and individual magnet positions is,

$$\mathcal{X}_d(t) = 3R^T(t)\mathcal{X}_{COM}. \tag{5.16}$$

The controller, (5.13)-(5.14), is applicable to all BSRs and can easily be adapted to generic undulating terrain. Let the path error be denoted by $\delta(t)$, defined in (5.7). The error $\delta(t)$ is represented as a vector in the surface's pre-image. Then, the outer loop produces the desired angular velocity,

$$\bar{\omega}^s(t) = \nabla\varphi(u,v)\left(K_p^\omega \delta + K_i^\omega \int \delta \cdot dt + K_d^\omega \dot{\delta}\right) \times N(t),$$

Symbol	Value
$(K_p^\omega, K_i^\omega, K_d^\omega)$	$(0.65, 0.02, 0.95)$
$(K_p^\chi, K_i^\chi, K_d^\chi)$	$(0.40, 0.02, 0.00)$

Table 5.2: Feedback Gains, Cascaded Controller Used in Moball Simulations.

where $N(t)$ is the surface normal at the point of contact and $\nabla\varphi : \mathbb{R}^2 \to \mathbb{R}^3$ is the surface's tangent map. The angular velocity error is defined as in (5.14), and the inner loop (5.15) is changed slightly to,

$$\mathcal{X}_{COM} = N(t) \times \Big(K_p^\chi e_\omega + K_i^\chi \int e_\omega \cdot dt + K_d^\chi \dot{e}_\omega \Big).$$

The cascaded PID controller was implemented in simulation on a three-axis Moball, as described in Subsection (4.3.1), rolling on a flat plane. The simulated feedback gains are shown in Table 5.2, and Moball's physical parameters are defined in Table 5.4. Control authority is assumed to be continuously available along the length of Moball's internal tubes, i.e. the solenoid's electromagnetics are unmodeled and the inputs are forces applied to each magnet, denoted by F_i. Once the desired magnet positions are obtained via (5.16), Moball's magnet dynamics are feedback linearized to track $\mathcal{X}_d(t)$. The dynamics governing the i^{th} magnet are given by,

$$\ddot{\mathcal{X}}_i = r_b(\hat{\gamma}\dot{\omega}^b)_i - g\gamma_i + \mathcal{X}_i(\omega^b)^T(I - f_i f_i^T)\omega^b + \frac{D(\dot{\mathcal{X}}_i) + F_i}{M_i}, \tag{5.17}$$

where $\gamma \triangleq R^T e_3$ is an advected parameter, f_i is the body axis along which the i^{th} magnet is aligned, and $D(\dot{\mathcal{X}}_i)$ represents linear damping. The following control,

$$F_i = M_i\Big(\ddot{\mathcal{X}}_d - K_p(\mathcal{X} - \mathcal{X}_d) - K_d(\dot{\mathcal{X}} - \dot{\mathcal{X}}_d) + g\gamma_i - r_b(\hat{\gamma}\dot{\omega}_b)_i - \mathcal{X}_i(\omega^b)^T(I - f_i f_i^T)\omega^b\Big) - D(\dot{\mathcal{X}}_i),$$

feedback linearizes (5.17), where (K_p, K_d) are chosen such that the error dynamics are characterized by a $1s$ settling time and 2% overshoot.

In Fig. 5.7, the cascaded feedback controller stabilizes Moball about a $20m$-diameter circular trajectory. Moball's initial position is in the center of the circle. The trajectory begins at the point $(10, 0)$ with a constant linear velocity of $0.5m/s$. Fig. 5.7a shows the desired trajectory and the trace of the vehicle's motion. After overshooting the desired trajectory by about 3 vehicle diameters, the ball stabilizes to the trajectory in approximately $50s$ with a constant error of less than half a vehicle diameter. A trajectory error less than one vehicle diameter is acceptable for the scientific surveys that Moball is intended for. Figs. (5.7b) and (5.7c) are screenshots from the simulation of this trajectory. Moball's $\{x, y, z\}$ magnets slide along

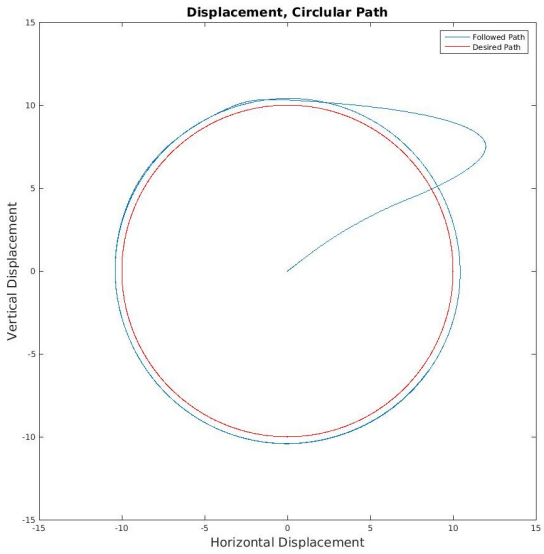

(a) Displacement on the plane.

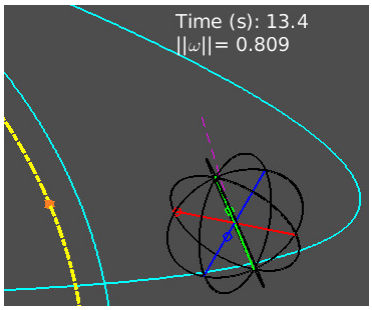

(b) During overshoot, large magnet displacements required for correction.

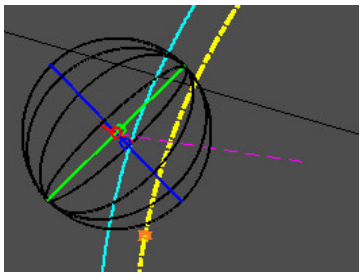

(c) Steady-state, only small displacement of COM required.

Figure 5.7: Feedback Control Simulation of Moball Tracking Circular Path.

axes that are depicted in $\{r, g, b\}$, and their positions are represented by circles. The desired path is shown in yellow, $\mu^s(t)$ is depicted as an orange circle, the vehicle's path is shown in light blue, and the instantaneous axis of rotation is shown in magenta. During the initial transient phase (Fig. 5.7b), large magnet displacements are required to guide the vehicle to the desired trajectory. However, in steady state (Fig. 5.7c) small deviations of the COM suffice for tracking control. In general, if the translational velocity of the desired path is less than $2m/s$, the path can be tracked with COM displacements less than $10cm$ from the vehicle's COR. The ease of controlling a BSR is heavily dependent on the ratio between the total moving actuator mass and the total system mass.

Fig. 5.8 shows the feedback controller guiding Moball along a variety of complicated, quickly varying trajectories on the plane. Fig. 5.8a shows Moball tracking a serpentine path with less than $1m$ of error in steady-state, whereas Fig. 5.8b shows Moball following a figure eight trajectory with less than $1.2m$ error in steady state. In Fig. 5.8c, Moball tracks a four-leaf epitrochoid with less than four meter error in steady state. The constant error in steady state arises from the speed of the trajectories and the choice of the feedback gains in Table 5.2, which were chosen as a

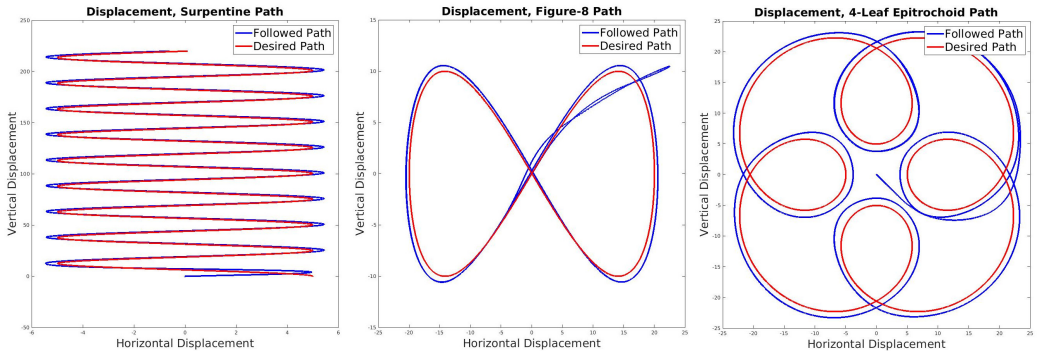

(a) Serpentine. (b) Figure-8. (c) Four-leaf Epitrochoid.

Figure 5.8: Feedback Controlling Moball on Quickly Varying Paths.

compromise between steady state error and settling time. The steady state error is smaller along trajectories with smaller curvatures, i.e. straight-line segments.

5.4 Ballistic Impulse Controller

Moball's internal magnets are controlled by applying currents to solenoids that are placed at regular intervals concentric to each internal tube. In Appendix A, the electromechanical coupling function α provides a relationship between an applied current and the resulting force to a nearby magnet. This coupling function quickly becomes negligible more than 2" from the solenoid's center. However, the coupling function peaks in two locations within approximately 1" of the solenoid's center. Moreover, this peak has been experimentally determined to have a magnitude of $40\frac{N}{A}$, such that a significant force can be applied to a magnet near this peak.

The system's limited control authority along the span of each inner tube stymies any continous control scheme. The isolated peaks of α motivate a "discrete" control approach, whereby impulses are applied to a magnet only when it passes by a local maximum of the electromechanical coupling function. A laser distance sensor accurately measures each magnet's internal position, signifying when an impulse is to be applied. Each impulse's magnitude is selected by solving a quadratic program (QP) that minimizes trajectory error over a finite time horizon, T. After an impulse is imparted, the magnet is free to travel ballistically until it crosses the local maximum of another solenoid's electromechanical coupling function. This approach is termed a ballistic impulse controller.

The force applied to the i^{th} magnet can be written as $F_i(\mathcal{X}_i) = \sum_{j=1}^{n} \alpha(\mathcal{X}_i - \mathcal{X}_{j,c})I_j$, where α is the electromechanical coupling function of Appendix A, $\mathcal{X}_i$ is the position of the magnet within its inner tube, $\mathcal{X}_{j,c}$ is the position to the center of the j^{th}

solenoid, and n is the total number of solenoids. The force can be rewritten as,

$$F_i(\mathcal{X}_i) = \beta(\mathcal{X}_i) \cdot \vec{I},$$

where $\beta(\mathcal{X}_i) = \begin{pmatrix} \alpha(\mathcal{X}_i - \mathcal{X}_{1,c}) & \dots & \alpha(\mathcal{X}_i - \mathcal{X}_{n,c}) \end{pmatrix}$ and $\vec{I} = \begin{pmatrix} I_1 & \dots & I_n \end{pmatrix}$. The applied current is chosen to be,

$$\vec{I} = \frac{\beta(\mathcal{X}_i)}{||\beta(\mathcal{X}_i)||} \cdot \nu,$$

where $\nu \in \mathbb{R}$ is the cumulative current applied over all solenoids. An applied current of this form ensures that current is applied only to the solenoids closest to the magnet, e.g. equal currents are applied to solenoids separated from the magnet by equal distances. Under this control choice, the applied force becomes $F_i(\mathcal{X}_i) = ||\beta(\mathcal{X}_i)|| \cdot \nu$. Then, the magnet dynamics (5.17) can be written as,

$$\ddot{\mathcal{X}}_i = ||\beta(\mathcal{X}_i)|| \cdot \bar{\nu} + \ddot{\mathcal{X}}_{dist}(\mathcal{X}_i, \dot{\mathcal{X}}_i, \vec{p}), \tag{5.18}$$

where $\bar{\nu} = (\nu/M_i)$ and $\ddot{\mathcal{X}}_{dist}(\mathcal{X}, \dot{\mathcal{X}}, \vec{p})$ encompasses the gravity, damping, and inertial acceleration terms, treated as a disturbance.

Impulses are applied at the maxima of α to illustrate the approach. As the magnet crosses the j^{th} peak, the dynamics become,

$$\ddot{\mathcal{X}}_i = \beta_{max} \cdot \bar{\nu} + \ddot{\mathcal{X}}_{dist}(\mathcal{X}_i, \dot{\mathcal{X}}_i, \vec{p}),$$

where $\beta_{max} \in \mathbb{R}$ is α's maximum, e.g. $40\frac{N}{A}$ for the solenoid used in Appendix A. Suppose now that an impulse is applied over a small time period Δ. If $(\mathcal{X}_i^-, \dot{\mathcal{X}}_i^-)$ and $(\mathcal{X}_i^+, \dot{\mathcal{X}}_i^+)$ denote the magnet's state before and after the impulse, then

$$\begin{bmatrix} \mathcal{X}_i^+ \\ \dot{\mathcal{X}}_i^+ \end{bmatrix} = \begin{bmatrix} \mathcal{X}_i^- \\ \dot{\mathcal{X}}_i^- + \Delta(\beta_{max} \cdot \bar{\nu} + \ddot{\mathcal{X}}_{dist}) \end{bmatrix}, \tag{5.19}$$

where $\ddot{\mathcal{X}}_{dist}$ is the acceleration of the magnet measured before the onset of the impulse. An applied impulse can be used to instantaneously change the magnet's velocity. More explicitly, letting

$$\bar{\nu} = \frac{1}{\beta_{max}} \Big(\frac{1}{\Delta} \delta\dot{\mathcal{X}}_i - \ddot{\mathcal{X}}_{dist} \Big), \tag{5.20}$$

implies that $\dot{\mathcal{X}}_i^+ = \dot{\mathcal{X}}_i^- + \delta\dot{\mathcal{X}}_i$. The task then becomes one of identifying a change in velocity, $\delta\dot{\mathcal{X}}_i$, that most optimally tracks a desired magnet trajectory during the

forthcoming ballistic motion phase. Moball is constrained by a maximum current limit, $|\bar{v}| \leq I_{max}$. Via (5.20), the change in velocity is subsequently constrained by,

$$\Delta(\ddot{\mathcal{X}}_{dist} - \beta_{max} \cdot I_{max}) \leq \delta\dot{\mathcal{X}}_i \leq \Delta(\ddot{\mathcal{X}}_{dist} + \beta_{max} \cdot I_{max}).$$

The optimization problem to be solved, then, is given by

$$\begin{aligned} &\min_{\delta\dot{\mathcal{X}}_i} \Big(\int_{t_0}^{T} (\mathcal{X}_i^+(t) - \mathcal{X}_d(t))^2 dt \Big), \\ \text{s.t. } &\ddot{\mathcal{X}}_i^+ = \ddot{\mathcal{X}}_{dist}(\mathcal{X}_i^+, \dot{\mathcal{X}}_i^+, \vec{p}), \\ &\mathcal{X}_i^+(t_0) = \mathcal{X}_i^-, \;\; \dot{\mathcal{X}}_i^+(t_0) = \dot{\mathcal{X}}_i^- + \delta\dot{\mathcal{X}}_i, \\ &\delta\dot{\mathcal{X}}_i \leq \Delta(\ddot{\mathcal{X}}_{dist}(\mathcal{X}_i^+, \dot{\mathcal{X}}_i^+, \vec{p}) + \beta_{max} \cdot I_{max}), \\ &\delta\dot{\mathcal{X}}_i \leq \Delta(\beta_{max} \cdot I_{max} - \ddot{\mathcal{X}}_{dist}(\mathcal{X}_i^+, \dot{\mathcal{X}}_i^+, \vec{p})), \end{aligned} \tag{5.21}$$

where T is a finite horizon, $\mathcal{X}_d(t)$ is a desired continuous magnet trajectory, and the objective function is the squared trajectory error. To simplify the optimization problem, the acceleration $\ddot{\mathcal{X}}_{dist}$ (due to Moball's motion and gravity) measured before the application of the impulse is assumed to be constant throughout the horizon T. This assumption is reasonable as the magnet's acceleration is dominated by gravity and centrifugal forces, and since T is typically less than $1s$, these forces are not anticipated to change significantly. This assumption allows the magnet's trajectory during the ballistic phase, $\mathcal{X}_i(t)$, to be expressed analytically. Letting $\sigma = T - t_0$ and $\tau = (t - t_0)/\sigma$,

$$\mathcal{X}_i^+(\tau) = \ddot{\mathcal{X}}_{dist} \frac{(\sigma\tau)^2}{2} + (\dot{\mathcal{X}}_i^- + \delta\dot{\mathcal{X}}_i)(\sigma\tau) + \mathcal{X}_i^-.$$

By analytically solving for the magnet's trajectory as above, the dynamic constraints in (5.21) are inherently satisfied.

The desired magnet trajectory, $\mathcal{X}_d(\tau)$, is approximated as a quadratic function, i.e,

$$\tilde{\mathcal{X}}_d(\tau) = \sum_{j=0}^{2} \tilde{\mathcal{X}}_{d,j} \tau^i.$$

The trajectory error can be written as,

$$e_{\mathcal{X}}(\tau) = \mathcal{X}_i^+(\tau) - \mathcal{X}_d(\tau) = \Big(\sigma^2 \ddot{\mathcal{X}}_{dist} - 2\tilde{\mathcal{X}}_{d,2}\Big)\frac{\tau^2}{2} + \Big(\sigma(\dot{\mathcal{X}}_i^- + \delta\dot{\mathcal{X}}_i) - \tilde{\mathcal{X}}_{d,1}\Big)\tau + \Big(\mathcal{X}_i^- - \tilde{\mathcal{X}}_{d,0}\Big).$$

Symbol	Description	Value	Units
T	Finite Time Horizon	0.3	s
Δ	Impulse Window	20	ms
I_{max}	Current Limit	8	A
β_{max}	Electromechanical Coupling Maximum	40	(N/A)
$\vec{\mathcal{X}}_c$	Solenoid Positions	$(-0.54, -0.18, 0.18, 0.54)$	m

Table 5.3: Quantities Defined for Ballistic Impulse QP.

The trajectory error squared can then be evaluated analytically, leading to a QP equivalent to (5.21):

$$\begin{aligned}
&\min_{\delta\dot{\mathcal{X}}_i}\left(\frac{\sigma^2}{3}\cdot(\delta\dot{\mathcal{X}}_i)^2+\left((2/3)(\sigma\dot{\mathcal{X}}_i^-\tilde{\mathcal{X}}_{d,1})+(\mathcal{X}_i^-\tilde{\mathcal{X}}_{d,0})+(1/4)(\sigma^2\ddot{\mathcal{X}}_{dist}-\tilde{\mathcal{X}}_{d,2})\right)\cdot\delta\dot{\mathcal{X}}_i\right),\\
&\text{s.t. }\ \delta\dot{\mathcal{X}}_i\le\Delta(\ddot{\mathcal{X}}_{dist}+\beta_{max}\cdot I_{max}),\\
&\qquad\delta\dot{\mathcal{X}}_i\le\Delta(\beta_{max}\cdot I_{max}-\ddot{\mathcal{X}}_{dist}).
\end{aligned}\tag{5.22}$$

This simple QP can be solved with knowledge of the magnet and vehicle's state before the impulse (the vehicle's state is necessary to estimate $\ddot{\mathcal{X}}_{dist}$), the desired trajectory $\tilde{\mathcal{X}}(\tau)$, and the electromechanical coupling function α.

To validate the ballistic impulse controller, a set of simulations were conducted by integrating Moball's fully-coupled dynamics, on the plane, while executing the QP each time a magnet crosses a solenoid. The values defining the QP are listed in Table 5.3. Event-detection was incorporated into the RKMK integrator described in Section (5.1) such that an impulse could be applied at each solenoid crossing. The simulated Moball featured four solenoidal coils, symmetrically placed about the ball's center at a distance of $0.36m$. Linear springs with a stiffness of $1000(N/m)$ and an uncompressed length of $10cm$ are attached to the ends of each inner tube.

Fig. 5.9 shows the controller tracking a sinusoidal path, $\mathcal{X}_d(t) = 0.45\sin(t)$, along Moball's body z-axis for $30s$. Moball's initial orientation is aligned with the inertial frame and the magnets along the body x and y axes are commanded to remain at Moball's COR. Moball does not rotate throughout the simulation and the disturbance acceleration on the magnets, $\ddot{\mathcal{X}}_{dist}$, consists only of gravitational and damping terms. It is clear from Fig. 5.9 that the calculated impulses from the QP (5.22) are generating a magnet trajectory that approximates the desired trajectory. Obviously, this ballistic controller may only act when a magnet crosses a solenoid, as can be seen by the error that accumulates over the simulation's first second of duration as the magnet travels ballistically before its first crossing. The average execution time

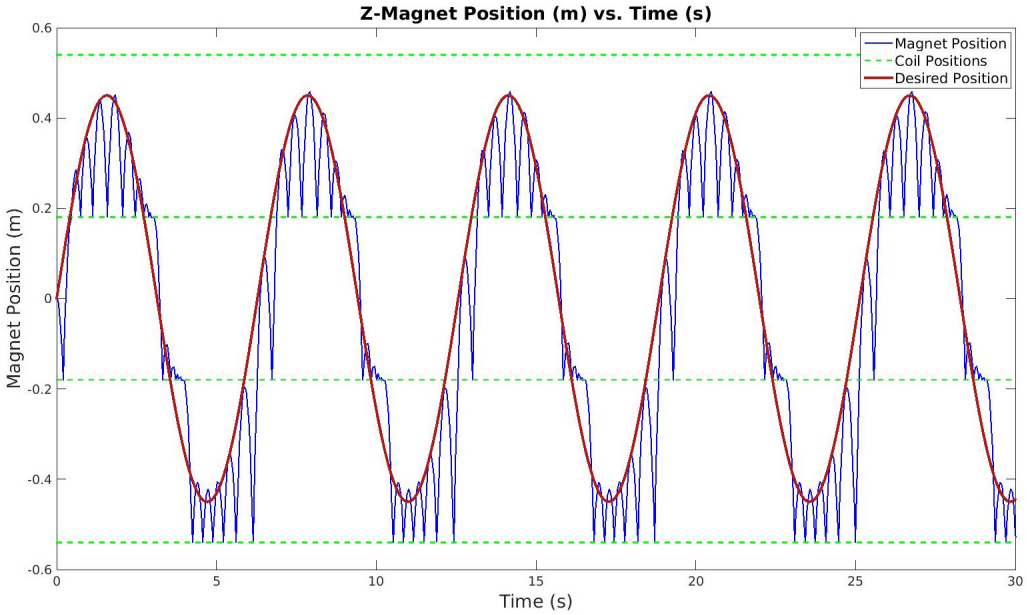

Figure 5.9: Ballistic Controller Tracking Sinusoid Along Vertical z-Axis.

of the QP (5.22) was $3.7ms$, which is a promising sign that the optimal velocity change $\delta\dot{X}$ may be calculated just before each magnet crosses a solenoid.

Fig. 5.10 shows the impulse controller tracking sinusoidal paths along each of Moball's body axes. In this 60 second long simulation, Moball's initial orientation was aligned with the inertial frame but Moball's magnets were placed randomly along each inner tube. The desired trajectories along the (x,y,z) body axes were sinusoids of amplitude $(0.25m, 0.35m, 0.45m)$ and periods $(\pi s, 4\pi s, 2\pi s)$, respectively; these trajectories do not accomplish a specific vehicle motion but were chosen to illustrate the impulse controller's ability to track smooth, sinusoidal trajectories. The QP (5.22) was solved 449 times throughout the simulation with an average execution time of $3.6ms$. Again, the controller is at the whim of the magnet's ballistic motion between subsequent solenoid crossings. For example, the magnet aligned along the x axis remains pinned to the outer edge for $20s$, preventing the controller from following the desired trajectory. Furthermore, the deviations from the desired trajectory along all axes are due to the disturbance acceleration $\ddot{X}_{dist}$ changing significantly outside of the time horizon T. To ensure that the impulse controller can adequately act on the magnet during its ballistic phase, solenoids should be placed close to the ends of each inner tube. Furthermore, increasing the time horizon T and relaxing the assumption that $\ddot{X}_{dist}$ remains constant throughout this window will reduce deviations from the desired trajectory, but care must be taken to ensure

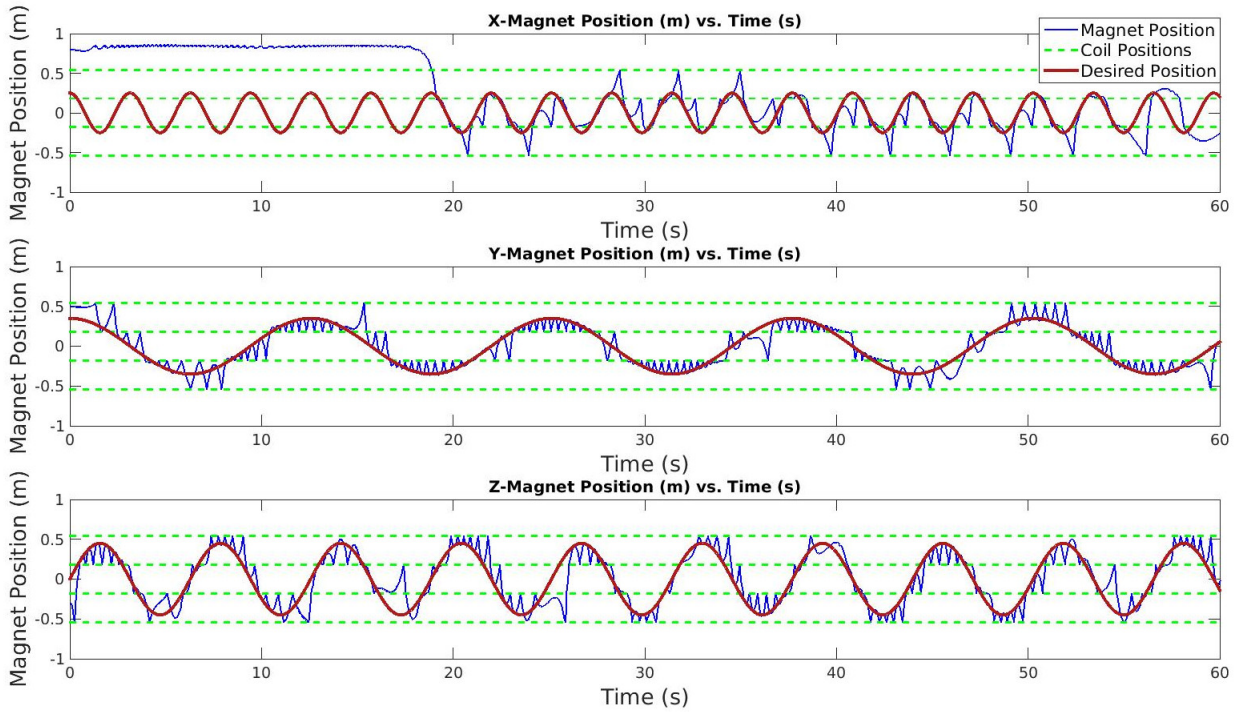

Figure 5.10: Ballistic Controller Tracking Sinusoids Along All Body Axes.

that the QP's execution time remains below $10ms$.

5.5 Feedforward Controller

Moball's feedforward controller is detailed in this section. First, numerical optimal control using the direct collocation method is reviewed. Then, a simplified model of Moball's dynamics is introduced, and direct collocation is applied to this low-order model. Simulations are then presented to validate the feedforward controller.

5.5.1 Optimal Control Using Direct Collocation

A feedforward controller produces actuator inputs, which when propagated through a system's dynamical equations, generate a desired system trajectory. The input to a feedforward controller is a desired trajectory and the outputs are the actuator policies corresponding to the desired trajectory. However, an analytical map between control policies and desired trajectories rarely exists for nonlinear dynamical systems. Furthermore, for a dynamical system with motion and actuator constraints, it may not even be possible to find feasible control policies to follow all desired trajectories, e.g. a car cannot navigate tight turns without slipping at high speeds. Instead of identifying control policies that exactly follow desired trajectories, feedforward controllers for constrained nonlinear systems produce control policies that are *opti-*

mal with respect to a chosen metric, and which respect the vehicle's dynamics and motion constraints. Optimality metrics take the following form,

$$L = \int_{t_0}^{T} J(q, \dot{q}, u)dt + \varphi(q(T)),$$

where $[t_0, T]$ is the time window over which the control is to be applied, $J(q, \dot{q}, u)$ is a positive definite path cost, and $\varphi(q(T))$ is a positive definite terminal state cost. Common path costs include the trajectory error squared $(q_d(t) - q(t))^2$ and energy consumption u^2. The terminal state cost typically penalizes deviations from a desired state, $(q(T), \dot{q}(T))$. As the metric represents penalties for undesired behavior, e.g. large trajectory errors and energy consumption, the optimal control policy minimizes the metric subject to the system dynamics,

$$\begin{aligned} &\min_{u \in \mathcal{U}} \Big(L = \int_{t_0}^{T} J(q, \dot{q}, u)dt + \varphi(q(T)) \Big), \\ &\text{s.t. } \dot{q} = f(q(t), u(t)), \end{aligned} \tag{5.23}$$

where $\mathcal{U}$ is the set of admissible control inputs.

Direct and indirect numerical methods can be used to solve the optimal control problem (5.23). An indirect method solves (5.23) using the calculus of variations and solving the first-order optimality conditions to identify the minimizer u^*. These methods are called indirect because the first-order optimality conditions must be solved before yielding the minimizing solution. Acquiring a solution to the first-order optimality conditions necessitates solving a boundary value problem, e.g. Pontryagin's Maximum Principle is an indirect method. A direct numerical method parameterizes the control $u(t)$ and state $q(t)$ throughout the time domain and uses nonlinear programming (NLP) to identify the optimal parameters. In practice, direct numerical methods have larger radii of convergence as compared to indirect methods; the convergence of a direct method to a minimizer is not nearly as sensitive to the initial guess as compared to indirect methods.

Direct collocation is employed to create Moball's feedforward controller. As a first step, the infinite dimensional optimization problem (5.23) is *transcribed* into a finite-dimensional optimization problem. To accomplish this, the time interval $[0, T]$ is subdivided into smaller, possibly non-uniform, time segments

$$t_0 < t_1 < \ldots < t_m = T.$$

In this work, time is divided into m uniform segments of width $\Delta = (T - t_0)/m$. Let $\{q_i, u_i\}$ denote the state and input at the time t_i. Within each time window $[t_i, t_{i+1}]$,

the state is parameterized using a convenient, finite-dimensional basis. A popular choice [83] adopted here is the use of a cubic polynomial,

$$\bar{q}_i(t) = \sum_{i=0}^{3} a_i \Big(\frac{t - t_i}{\Delta}\Big)^i, \;\; t \in [t_i, t_{i+1}],$$
$$\bar{q}_i(\tau) = \sum_{i=0}^{3} a_i \tau^i, \;\; \tau = \frac{t - t_i}{\Delta}, \;\; \tau \in [0, 1].$$

Other common choices of bases include Chebyshev or Lagrange orthogonal polynomials. The state coefficients $\{a_i\}_{i=1}^3$ are chosen to ensure C^1 continuity between adjacent state representations, i.e.

$$\begin{aligned} \bar{q}_i(0) &= \bar{q}_{i-1}(1) = q_i, \\ \bar{q}_i(1) &= \bar{q}_{i+1}(0) = q_{i+1}, \\ \frac{d}{dt}(\bar{q}_i(0)) &= f(\bar{q}(0), \bar{u}(0)) = f(q_i, u_i), \\ \frac{d}{dt}(\bar{q}_i(1)) &= f(\bar{q}(1), \bar{u}(1)) = f(q_{i+1}, u_{i+1}). \end{aligned} \tag{5.24}$$

These conditions completely determine the coefficients $\{a_i\}_{i=1}^3$, and by (5.24) the state representation $\bar{q}_i(\tau)$ is only dependent on the variables $\{q_i, q_{i+1}, u_i, u_{i+1}\}$. The input $\bar{u}(t)$ is similarly parameterized as a cubic polynomial and the coefficients are chosen to ensure C^1 continuity.

Once the state and inputs have been parameterized, (5.23) is transcribed into a finite-dimensional problem in the variables $\vec{z} = \{q_0, q_1, \ldots, q_n, u_0, u_1, \ldots, u_n\}$. Note that the integral in (5.23) can be rewritten as,

$$\int_{t_0}^{T} J(q, \dot{q}, u) dt + \varphi(q(T)) \approx \sum_{i=0}^{m-1} \int_{t_i}^{t_{i+1}} J(\bar{q}_i(t), \dot{\bar{q}}_i(t), \bar{u}_i(t)) dt + \varphi(q_m) = \tilde{L}(\vec{z}), \tag{5.25}$$

and since $\bar{q}_i(t)$ and $\bar{u}_i(t)$ admit simple parameterized forms, each of sub-integrals in (5.25) can be evaluated analytically as a function of $\{q_i, q_{i+1}, u_i, u_{i+1}\}$. Together, the approximate objective function, $\tilde{L}(\vec{z})$, can be written using the decision variables $\vec{z}$.

Each approximation of the state, $\bar{q}_i(\tau)$, must be constrained to match the true system dynamics at a finite set of points. Although $\bar{q}_i(\tau)$ is consistent with the system dynamics at its endpoints by construction (5.24), it is desirable to have the state representation match the system dynamics at a finite set of *collocation points* within the interval. *Defect constraints* are defined as,

$$\zeta_j = \dot{\bar{q}}_i(\tau_j) - f(\bar{q}_i(\tau_j), \bar{u}_i(\tau_j)), \;\; j \in [1, \ldots, K],$$

where there are K defect constraints and collocation points located at times τ_j. When the defect constraint $\zeta_j \to 0$, the state approximation $\bar{q}_j(\tau)$ is consistent with the system dynamics at time τ_j. A single collocation point at the center of the interval, e.g. $\tau = (1/2)$, is adopted here. The defect constraints are grouped as $\vec{\zeta} = (\zeta_0, \zeta_1, \ldots, \zeta_m)$ and treated as an equality constraint for the minimizer to satisfy. Actuator and path constraints, e.g. limitations on Moball's magnet positions or the ball's position on the plane, can be directly represented as inequality constraints on the decision variables, $\vec{z}_l \leq \vec{z} \leq \vec{z}_r$. Together, the infinite dimensional optimization problem (5.23) is transcribed to the finite-dimensional NLP,

$$\begin{aligned} &\min_{\vec{z}} \tilde{L}(\vec{z}), \\ &\text{s.t.} \begin{bmatrix} \vec{0} \\ \vec{z}_l \end{bmatrix} \leq \begin{bmatrix} \vec{\zeta} \\ \vec{z} \end{bmatrix} \leq \begin{bmatrix} \vec{0} \\ \vec{z}_r \end{bmatrix}. \end{aligned} \tag{5.26}$$

When a minimizer $\vec{z}^*$ is identified, the approximated state and input can be reconstituted using the adopted parameterizations.

Direct collocation is a general tool that has been applied to many engineering and robotic systems. These methods have been used to generate optimal paths for aeronautical applications [16, 40], as well as generating gaits enabling legged locomotion [36, 86]. See [70] for a comprehensive survey of the numerical methods, including direct collocation, used to solve optimal control problems. A feedforward controller based on direct collocation has not been applied to spherical vehicles, to the author's knowledge.

As $\tilde{L}(\vec{z})$ and the constraints are generally nonlinear, analytical or numerical estimates of the objective and constraint Jacobians greatly improve the speed of convergence to a minimizer. Since the direct collocation scheme described above is *local*[4], i.e. the state and inputs are parameterized in local time windows, the Jacobian $\partial\vec{\zeta}(\vec{z})/\partial\vec{z}$ is often sparse. For example, the $(i-1)^{th}$, i^{th}, and $(i+1)^{th}$ time segments are only functions of the variables $\{q_i, q_{i+1}, u_i, u_{i+1}\}$, and therefore the Jacobian $\partial\vec{\zeta}(\vec{z})/\partial\vec{z}$ will tend to be block-diagonal. To take advantage of the natural sparsity inherent in these problems, TOMLAB's Sparse Nonlinear Optimizer (SNOPT) [30] software is used to solve the NLP (5.26). SNOPT is a sequential quadratic programming (SQP) method that solves the generic nonlinear NLP (5.26) by leveraging the sparsity in the constraint Jacobian [30].

[4]Global collocation methods use a single parameterization of the state across the entire time domain and vary the order of the parameterization, whereas local collocation methods fix the order of the parameterization and use multiple representations of the state across $[t_0, T]$.

5.5.2 Simplified Moball Dynamical Model

In this subsection, Moball's dynamics are simplified before applying direct collocation. Although direct collocation applies to generic nonlinear systems, a simplified model of Moball's dynamics allows the Jacobian of the objective function and constraints in (5.26) to be computed analytically, which greatly improves convergence speed. The feedforward controller is developed for the Moball model developed in Subsection (4.3.1). Two modifications are made to the momentum differential equations shown in (4.30). First, a *virtual constraint* is applied whereby control actions are designed to ensure,

$$\langle \mathcal{X}, \gamma \rangle \equiv \text{const.}, \tag{5.27}$$

where the constant is chosen to be zero for the remainder of this work. This constraint on the magnet position physically corresponds to the vehicle's COM being constrained to a horizontal plane at a constant height above the ground plane. When this constraint is enforced, then $\frac{d}{dt}\langle \mathcal{X}, \gamma \rangle = 0$ implies,

$$\langle \mathcal{V}, \gamma \rangle = \omega^b_\beta \langle \mathcal{X}, \alpha \rangle - \omega^b_\alpha \langle \mathcal{X}, \beta \rangle.$$

This equality cancels the quadratic terms in the momentum differential equation (4.3.1), leaving only the gravitational terms. Added to this differential equation are damping terms arising from air resistance as Moball moves through ambient air. Assuming that the resistive force acts horizontal to the plane at the vehicle's COR, the momentum equations can be rewritten as,

$$\begin{bmatrix} \dot{p}_\alpha \\ \dot{p}_\beta \end{bmatrix} = \begin{bmatrix} -M_i g \mathcal{X}_\beta - \text{sign}(\omega^b_\alpha) \frac{\pi \rho r_b^5 (\omega^b_\alpha)^2}{4}, \\ M_i g \mathcal{X}_\alpha - \text{sign}(\omega^b_\beta) \frac{\pi \rho r_b^5 (\omega^b_\beta)^2}{4} \end{bmatrix}, \tag{5.28}$$

where $\mathcal{X}_\alpha = \langle \mathcal{X}, \alpha \rangle$ and $\mathcal{X}_\beta = \langle \mathcal{X}, \beta \rangle$. Note that (5.28) is much simpler than the momentum equation of (4.30) as a result of the virtual constraint. To preserve continuity of the dynamics, the sign$(\cdot)$ function is approximated using a high-order sigmoid function, $\sigma(x) = \tanh(k \cdot x)$, in the following simulations.

Moball's reconstruction equation can be written as,

$$\underbrace{\begin{bmatrix} r_b^2 M_T + 2 r_b M_i \langle \mathcal{X}, \gamma \rangle + \langle \alpha, \Phi(\mathcal{X}) \alpha \rangle & \langle \alpha, \Phi(\mathcal{X}) \beta \rangle \\ \langle \alpha, \Phi(\mathcal{X}) \beta \rangle & r_b^2 M_T + 2 r_b M_i \langle \mathcal{X}, \gamma \rangle + \langle \beta, \Phi(\mathcal{X}) \beta \rangle \end{bmatrix}}_{\triangleq \mathbb{I}(\mathcal{X})} \begin{bmatrix} \omega^b_\alpha \\ \omega^b_\beta \end{bmatrix} = \begin{bmatrix} r_b M_i \dot{\mathcal{X}}_\beta + p_\alpha \\ -r_b M_i \dot{\mathcal{X}}_\alpha + p_\beta \end{bmatrix}, \tag{5.29}$$

where $\dot{\mathcal{X}}_\alpha = \langle \mathcal{V}, \alpha \rangle$ and $\dot{\mathcal{X}}_\beta = \langle \mathcal{V}, \beta \rangle$. The off-diagonal terms are zero when the COM is located at the COR, and have a larger magnitude as the ratio between

the magnet mass, M_i, and total mass M_T, increases. In practice, the matrix $\mathbb{I}(\mathcal{X})$ is found to be diagonally dominant whereby the diagonal entries are one or two orders of magnitude larger than the off-diagonal terms. Based on this observation and the virtual constraint (5.27), the matrix $\mathbb{I}(\mathcal{X})$ is approximated as,

$$\tilde{\mathbb{I}}(\mathcal{X}) = \begin{bmatrix} r_b^2 M_T + M_i(\mathcal{X}_\alpha^2 + \mathcal{X}_\beta^2) + I_{net} & 0 \\ 0 & r_b^2 M_T + M_i(\mathcal{X}_\alpha^2 + \mathcal{X}_\beta^2) + I_{net} \end{bmatrix}, \tag{5.30}$$

where I_{net} is the scalar defining the constant-entry, diagonal matrix $(I_{s,com} + \sum_{i=1}^{3} I_{m,i})$. Upon substituting the no-slip constraints (4.5), the connection can be compactly written as,

$$\begin{bmatrix} \dot{d}_\alpha^b \\ \dot{d}_\beta^b \end{bmatrix} = \frac{1}{r_b^2 M_T + M_i(\mathcal{X}_\alpha^2 + \mathcal{X}_\beta^2) + I_{net}} \begin{bmatrix} -r_b^2 M_i \dot{\mathcal{X}}_\alpha + r_b p_\beta \\ -r_b^2 M_i \dot{\mathcal{X}}_\beta - r_b p_\alpha \end{bmatrix}. \tag{5.31}$$

When the inputs to the system are treated as $(\mathcal{X}_\alpha, \mathcal{X}_\beta)$, the motion of the ball on the plane is independent of the rotation matrix R, thus eliminating the need to parameterize the rotation matrix locally. Physically, this models the relationship between moving the COM in the directions of α and β and the corresponding translations that follow from the no-slip constraints (4.5), irrespective of rotation. Furthermore, since there is no rotation matrix dependency, d^b, p_α and p_β can be locally parameterized using the cubic direct collocation scheme [83].

To determine how valid this simplification is for the Moball parameters in Table 5.4, the following test was conducted. The matrix $\mathbb{I}(\mathcal{X})$ is a function of the orientation through the dependencies on (α, β, γ), and the magnet positions $\mathcal{X}$. First, rotation matrices were sampled from a uniform distribution on $SO(3)$ using the technique described in [6]. For each random orientation, the matrix $\mathbb{I}(\mathcal{X})$ and the error of the approximation, $\delta\mathbb{I}(\mathcal{X}) = \mathbb{I}(\mathcal{X}) - \tilde{\mathbb{I}}(\mathcal{X}))$, were calculated for all possible magnet locations $\mathcal{X}$. The mean of the entries of $\delta\mathbb{I}(\mathcal{X})$ were then computed across all trials. The mean $\bar{\mathbb{I}}(\mathcal{X})$ and absolute value of the mean error $\delta\bar{\mathbb{I}}(\mathcal{X})$ across 10,000 trials was,

$$\bar{\mathbb{I}}(\mathcal{X}) = \begin{bmatrix} 28.7118 & 0.0000 \\ 0.0000 & 28.7116 \end{bmatrix}, \quad |\delta\bar{\mathbb{I}}(\mathcal{X})| = \begin{bmatrix} -0.1400 & 0.0000 \\ 0.0000 & 0.1402 \end{bmatrix}$$

Note that on average, the error of the off-diagonal terms is negligible. The relative absolute error $|\delta\bar{\mathbb{I}}(\mathcal{X})|/\mathbb{I}(\mathcal{X})$ of the diagonal terms is approximately 0.5%. On average, the diagonal terms of the approximation in (5.30) differ by less than 1% of the true value, and these entries are the dominant terms in the locked inertia tensor. For these reasons, the approximation of $\tilde{\mathbb{I}}(\mathcal{X})$ in (5.30) is deemed suitable for the

feedforward controller. Thus, the simplified Moball dynamics used for direct collocation consist of the momenta equation (5.28) with the velocity $\dot{d}^b$ subtituted for ω^b using the no-slip constraints (4.5) and the simplified connection (5.31). An advection differential equation is not included here since the dynamics are independent of rotations, and $(\mathcal{X}_\alpha, \mathcal{X}_\beta)$ are considered inputs.

5.5.3 Moball Direct Collocation

Moball's state includes its position on the plane, (d^b_α, d^b_β), and the nonholonomic momenta, (p_α, p_β), both expressed in a body frame. Within the time segment $[t_i, t_{i+1}]$ let,

$$\tilde{p}(\tau) \triangleq \begin{bmatrix} \tilde{p}_\alpha \\ \tilde{p}_\beta \end{bmatrix} = \sum_{i=1}^{3} \tilde{p}_i \tau^i, \quad \tilde{d}^b(\tau) \triangleq \begin{bmatrix} \tilde{d}^b_\alpha \\ \tilde{d}^b_\beta \end{bmatrix} = \sum_{i=1}^{3} \tilde{d}^b_i \tau^i,$$

where $\{\tilde{p}_i\}, \{\tilde{d}^b_i\} \in \mathbb{R}^2$. As described in Subsection (5.5.1), the coefficients $\{\tilde{p}_i\}$ and $\{\tilde{d}^b_i\}$ are chosen to ensure C^1 continuity between adjacent state representations and therefore $\tilde{p}(\tau)$ and $\tilde{d}^b(\tau)$ are only functions of the momenta and positions at the endpoints. The defect constraints are defined at the midpoint of $[t_i, t_{i+1}]$ using the simplified dynamics (5.28) and (5.31), and the defect Jacobians are computed analytically.

Moball's magnet positions are parameterized as,

$$\tilde{\mathcal{X}}(\tau) \triangleq \begin{bmatrix} \mathcal{X}_\alpha \\ \mathcal{X}_\beta \end{bmatrix} = \sum_{i=1}^{3} \tilde{\mathcal{X}}_i \tau^i.$$

Again, the coefficients $\{\tilde{\mathcal{X}}_i\}$ are chosen to ensure C^1 continuity. Within $[t_i, t_{i+1}]$, the magnet parameterization, $\tilde{\mathcal{X}}(\tau)$, is a function of $(\mathcal{X}_i, \dot{\mathcal{X}}_i, \mathcal{X}_{i+1}, \dot{\mathcal{X}}_{i+1})$, which denotes the magnet's positions and velocities at the endpoints $[t_i, t_{i+1}]$. Hence, the inputs to the NLP are the magnet positions and velocities at ends of each time segment.

The objective function adopted for this feedforward controller is,

$$L = \int_{t_0}^{T} \frac{1}{2} ||\tilde{d}^b(t) - d^b_{des}(t)||^2 dt + c_R \int_{t_0}^{T} ||\ddot{\tilde{\mathcal{X}}}(t)||^2 dt, \tag{5.32}$$

where $d^b_{des}(t)$ is a desired trajectory for Moball to follow on a flat plane, and $\tilde{d}^b(t)$ and $\tilde{\mathcal{X}}(t)$ are the representations of the vehicle and magnet positions, respectively. The first term in the objective function is a simple trajectory error penalty. The second term of the objective function is a regularizer that achieves two aims: (1) Due to the cubic approximations of the state $\mathcal{X}(\tau)$, without regularization the chosen

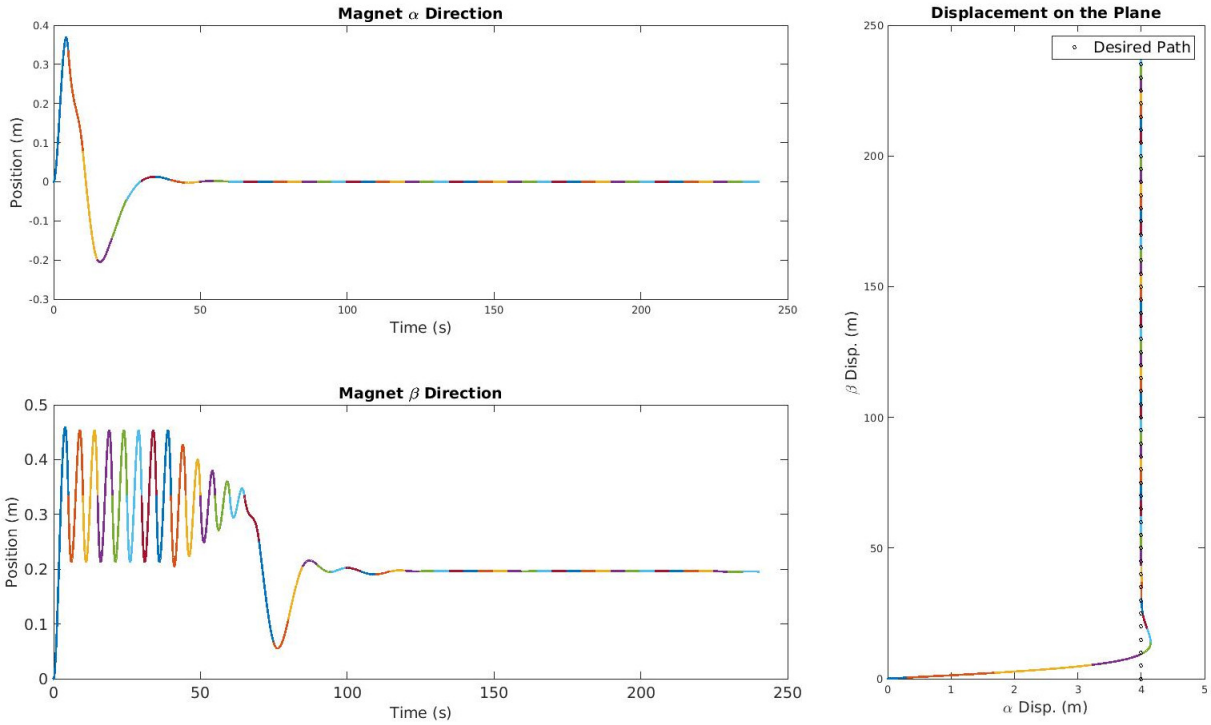

Figure 5.11: Feedforward Control, Straight Line Starting from Offset.

trajectory exhibits undesirable high-frequency oscillations. Penalizing the magnet accelerations minimizes this tendency and (2) Moball's physical control inputs are currents applied to solenoids, which in turn generate forces on the internal magnets. Minimizing the magnet accelerations leads to a minimum-energy solution as the work applied to the magnets is minimized. The relative importance of the regularizer versus the trajectory error is modulated via a constant $c_R \in \mathbb{R}$. As in Subsection (5.5.1), the objective function can be transcribed as a function of the state and inputs at the endpoints $[t_i, t_{i+1}]$. Due to the dynamics model adopted in (5.5.2), the Jacobian of the objective function can be calculated analytically.

5.5.4 Moball Feedforward Simulation Results

Moball's physical parameters are defined in Table 5.4 for the following simulations. As in Subsection (4.3.1), three magnets are assumed to travel along orthogonal axes that intersect at the vehicle's COR. Collisions are unmodeled, i.e. the magnets are allowed to travel through one another at the COR. While solving the NLP, constraints are emplaced such that $(\mathcal{X}_\alpha, \mathcal{X}_\beta) \leq (1/3) \cdot r_b$ and $(\mathcal{V}_\alpha, \mathcal{V}_\beta) \leq 0.25\ m/s$ at the endpoints $[t_i, t_{i+1}]$, where r_b is Moball's radius. These constraints are in place to ensure that $\tilde{\mathcal{X}}(\tau)$ (i.e. the approximate magnet positions) remain within the ve-

Symbol	Description	Value	Units
M_T	Total mass	21.5	kg
M_s	Structure mass	20.0	kg
M_i	Magnet mass	0.5	kg
r_b	Ball radius	1	m
g	Gravitational constant	9.81	m/s^2
ρ	Air density	1.225	kg/m^3
I_{net}	Net inertia	7.002	$kg \cdot m^2$

Table 5.4: Physical Values Used in Moball Simulations.

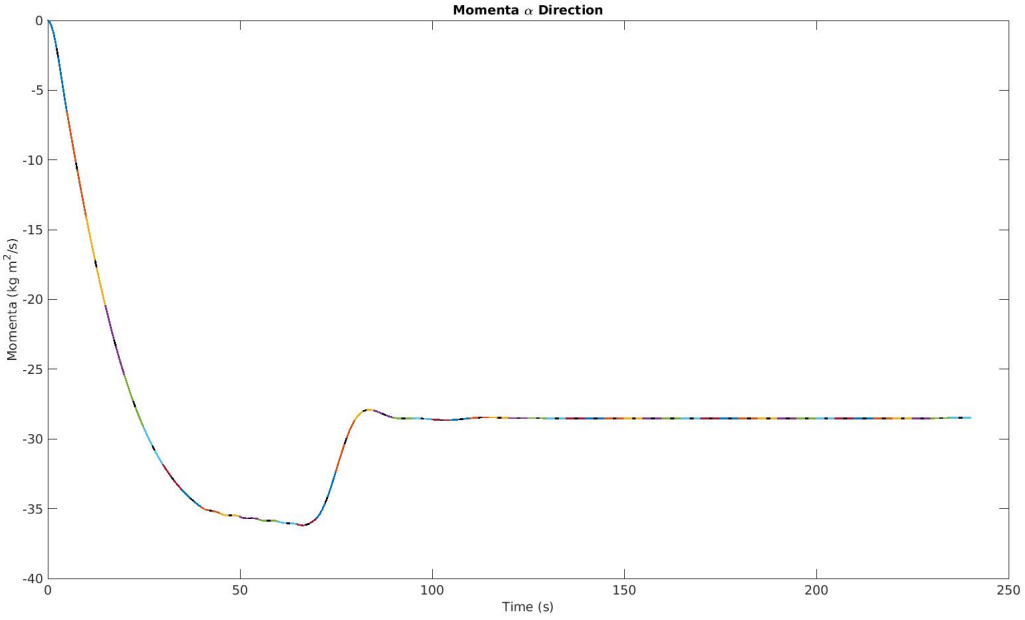

Figure 5.12: Feedforward Control, Straight Line. α Momenta Showing Defects.

hicle for all τ, and therefore the controls are physically realizable. The vehicle's translational velocity is constrained to be less than 4.0 m/s, and the momenta is subsequently constrained by this maximum velocity. The position of the vehicle on the plane is constrained to lie within a bounding box that extends 10 m around the desired trajectory. Time segments are defined to have width $\Delta = 5$ s. The NLP is seeded with a trajectory derived from a simple feedback controller, although convergence is typically observed with an initial guess of zeros, albeit at a slightly slower rate. Lastly, the regularizing constant c_R is set to 500 in each simulation.

In Fig. 5.11, the desired trajectory is a straight line with a velocity of 1 m/s, which is offset 4 m along the x-axis from Moball's starting location. Initially, Moball's

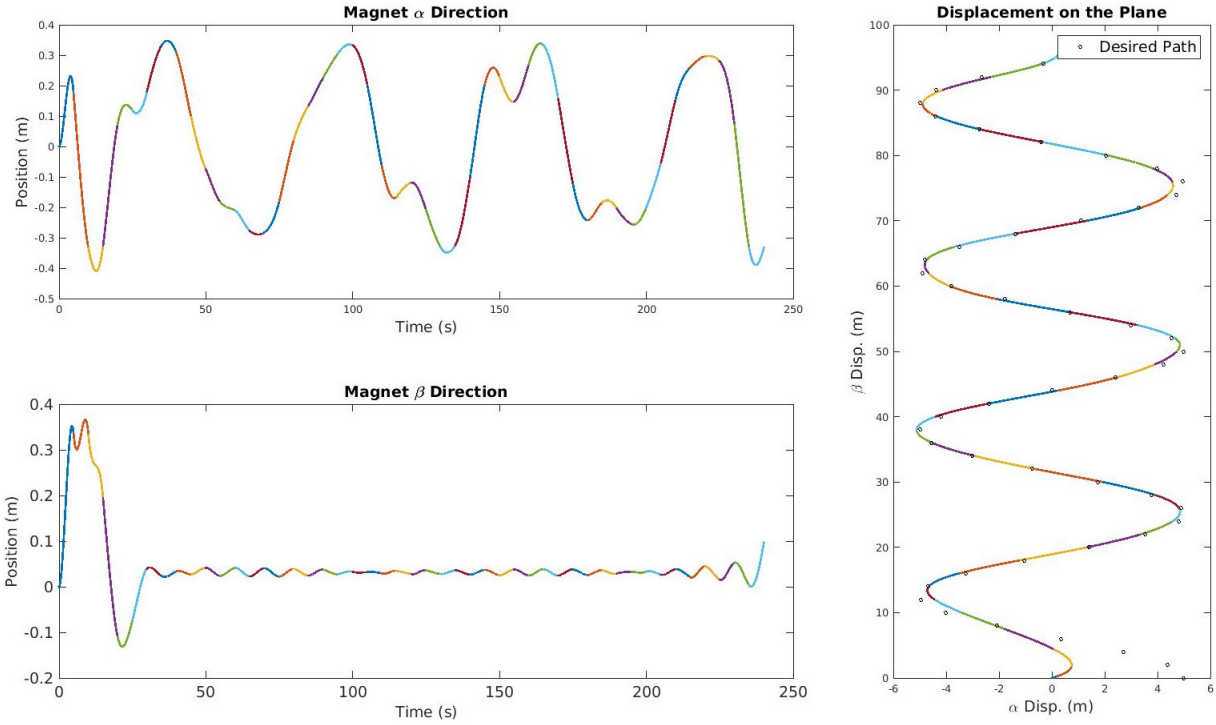

Figure 5.13: Feedforward Control, Serpentine.

magnets are placed at the COR and the vehicle is at rest. The magnet and ball trajectories that minimize the objective function (5.32) are shown in Fig. 5.11. The colors in these plots denote the individual time segments over which different state and input parameterizations are defined. Note that C^1 continuity is maintained between adjacent time segments as desired. A transient occurs in the first 50 s, in which $\tilde{\mathcal{X}}_\alpha$ drives the vehicle to the line along the y-direction with slight overshoot. The cyclic input $\tilde{\mathcal{X}}_\beta$ enables the vehicle to catch up to the desired trajectory in this transient phase, where the vehicle then overshoots the desired trajectory and must correct its speed at about 75 s. After approximately 100 s, $\tilde{\mathcal{X}}_\beta$ settles to a constant value required to match the 1 m/s velocity in the presence of air drag.

The momenta $\tilde{p}_\alpha$ is displayed in Fig. 5.12. Superimposed in the center of each time segment is the derivative of the momentum (5.28), shown as a black line, and evaluated using the approximations $\tilde{p}(\tau), \tilde{d}^b(\tau), \tilde{\mathcal{X}}(\tau)$. Each black line segment is aligned with the derivative of $\tilde{p}_\alpha$, suggesting that the defect constraints corresponding to $\tilde{p}_\alpha$ are near zero. In fact, SNOPT minimizes each of the defect constraints to a small tolerance on the order of 10^{-5}, such that the approximations $\tilde{d}^b(t)$ and $\tilde{p}(t)$ reasonably correspond to the vehicle's true position and momenta. In addition, by setting the number of major SQP iterations used by SNOPT to 100, a typical NLP

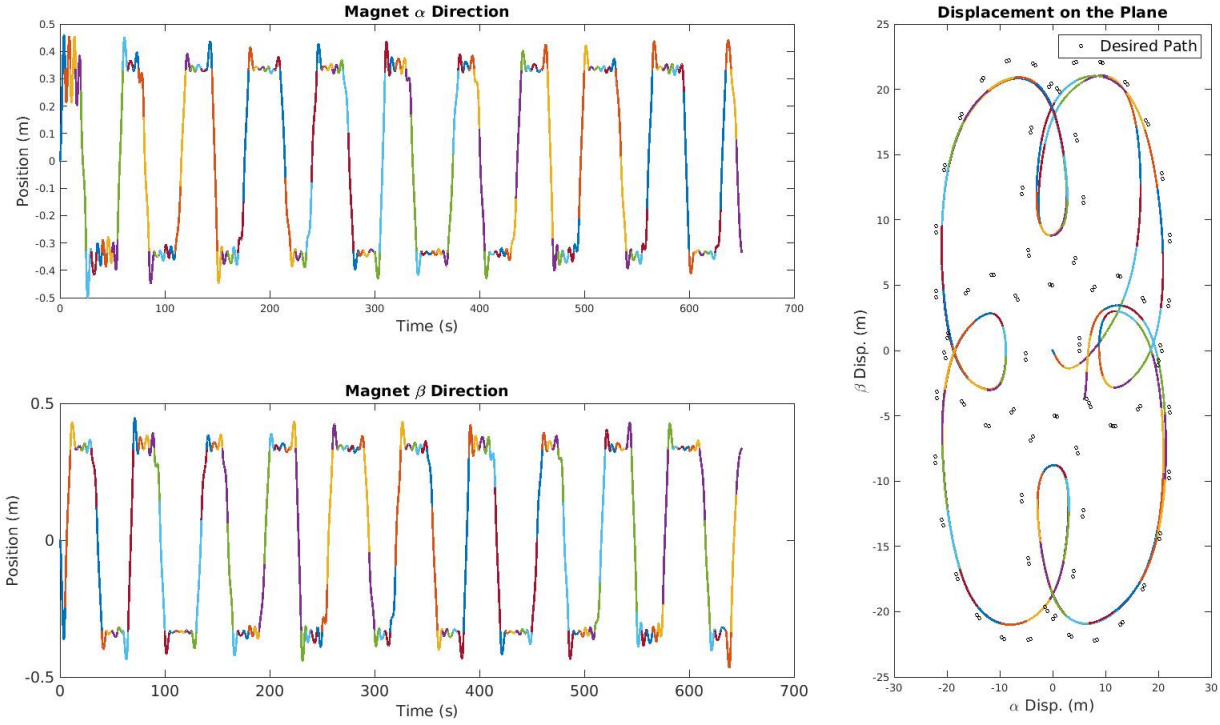

Figure 5.14: Feedforward Control, 4-Leaf Epitrochoid.

can be solved in less than $20s$, which is acceptable for field use.

In Fig. 5.13 and Fig. 5.14, Moball tracks a serpentine and a four leaf epitrochoid trajectory, illustrating the generality of the feedforward controller. Each of the NLPs underlying these trajectories were solved in less than $20s$. The four leaf epitrochoid trajectory in Fig. 5.14 demonstrates that the feedforward controller generates a reasonable trajectory even when it is not possible for the vehicle to exactly track the desired trajectory. In this case, minimizing the objective function 5.32 ensures that the resulting trajectory reasonably approximates the desired path.

5.5.5 Motion-Planning for Maximal Energy-Harvesting

A primary advantage of the Moball system is the incorporation of opportunistic energy-harvesting. Energy-harvesting increases the spatial reach and mission duration of a robotic asset as each individual vehicle is less burdened by the energy constraints of an onboard battery. To leverage this benefit, it is sensible to plan Moball's trajectories based on scientific objectives while continually seeking to expose the vehicle to available sources of energy in the environment. The two primary sources of environmental energy to harvest are caused by wind and the local topol-

ogy. Energy can be harvested and used to replenish the main battery when a wind gust blows Moball across the terrain, or when the vehicle rolls down a hill. This subsection introduces a simple motion planner which generates trajectories that satisfy scientific objectives while maximizing the energy-harvesting potential of the vehicle along its path.

First, a uniform grid in $\mathbb{R}^2$ is established, which may correspond to flat terrain or to the pre-image of an undulating surface. A vertex, v_i, is placed at the center of each grid square and the collection of vertices is denoted by V. The set V consists only of vertices that do not correspond to obstacles, which are regions of the grid over which the vehicle cannot pass (e.g. large rock outcrops). A directed edge, e_{ij}, passes from vertex i to vertex j, and the set of edges is denoted by E. A vertex is connected to each of its eight adjacent neighbors by an edge. Costs are associated to each edge in E depending on the proximity to scientific objectives, hazards, the orientation of the local wind field in relation to the goal, and the local topology. Each edge cost represents undesirability in moving between adjacent vertices, i.e. a large cost may denote that the vehicle is moving away from an objective, towards a hazard, against the wind, etc. Edge costs are chosen to be positive and each edge is initialized with a cost of unity, which corresponds to a simple distance penalty. An initial and terminal vertex are then identified and the path with the minimum net edge cost is selected using either the Dijkstra or A^* algorithm[5]. [32, 48]. The resulting path therefore minimizes the total distance traveled while balancing scientific objectives, hazard avoidance, and energy availability.

Some of the costs associated to each edge are *proximity costs*, which penalize edges based on the proximity of a vertex to a feature like a scientific objective or a hazard. Distance between a given vertex and a feature are measured using a *wavemap* [24]. Suppose that the distances from every vertex to a specified hazard are desired. A wavemap begins by assigning a value of unity to the hazard. Starting from the hazard's vertex, each adjacent vertex is assigned a value of two. Likewise, adjacent vertices to the newly labeled vertices are assigned the value of three, and this process continues until all vertices have been labeled with their distance to the hazard, denoted by δ. This measure of distance is more appropriate than a standard Euclidean distance metric when obstacles are present.

Using δ as a measure of distance, the edge cost associated with proximity to scien-

[5] Adaptive search algorithms, such as D^*, may also be implemented in this framework.

tific objectives is denoted by,

$$e_{ij}^{sci} = 1 + \delta_j^p, \tag{5.33}$$

where e_{ij} is an edge from vertex $i \rightarrow j$, δ_j is the wavemap distance of vertex j to the objective, and p is a user-defined exponent. It is clear from (5.33) that the minimum edge cost, e_{ij}^{sci}, will be directed towards the vertices closer to the scientific objective. Similarly, the edge cost associated with proximity to a hazard is denoted by,

$$e_{ij}^{haz} = (\delta_{max} - \delta_j)^q, \tag{5.34}$$

where δ_{max} is the largest wavemap distance of any node to the hazard, and q is a user-defined exponent. The edge cost, e_{ij}^{haz}, is minimized when the vertex j is furthest from the hazard. A hazard may correspond to terrain that is potentially dangerous, e.g. gullys that may trap the vehicle. In the simulations to follow, the exponents p and q from (5.33) and (5.34) are set to three.

Edge costs associated with local wind patterns and topology are *vector costs*, as these depend on various vector measurements. Consider the edge cost between two vertices in a local wind field, e_{ij}^{wind}. Assume that the wind field is defined over the grid, such that a wind blowing with a speed of $||w_i||$ acts tangent to the surface and is characterized by a direction θ_i relative to an arbitrary reference (e.g. a consistently chosen local tangent vector would suffice). Define d_j as the normalized local tangent direction pointing to an adjacent vertex, v_j. Then, $w_{||} = \langle w_i, d_j \rangle$ and $w_\perp = \sqrt{||w_i||^2 - w_{||}^2}$ define the wind's component acting along and orthogonal to the direction of v_j.

Energy from the wind can only be harvested over a finite range of wind-speeds. Below a minimum windspeed, $||w||_{min}$, the wind cannot rotate the vehicle and above a maximum windspeed, $||w||_{max}$, centrifugal forces will cause Moball's magnets to remain fixed to the vehicle's outer edge, preventing energy harvesting. Motivated by this, the component $w_{||}$ is weighted by a quadratic function whose minimum value of zero occurs at the wind speed, $\bar{w}_{||}$, that is optimal for energy harvesting. The quadratic's remaining degrees of freedom are chosen by penalizing $w_{||} = ||w||_{min}$ and $w_{||} = ||w||_{max}$ equally, by some value σ greater than zero. Any value of $w_\perp$ is undesirable for sustaining motion along d_j such that the edge weight associated with the wind e_{ij}^{wind} is defined by,

$$e_{ij}^{wind} = c_1 w_\perp^2 + a \cdot w_{||}^2 + b \cdot w_{||} + c, \tag{5.35}$$

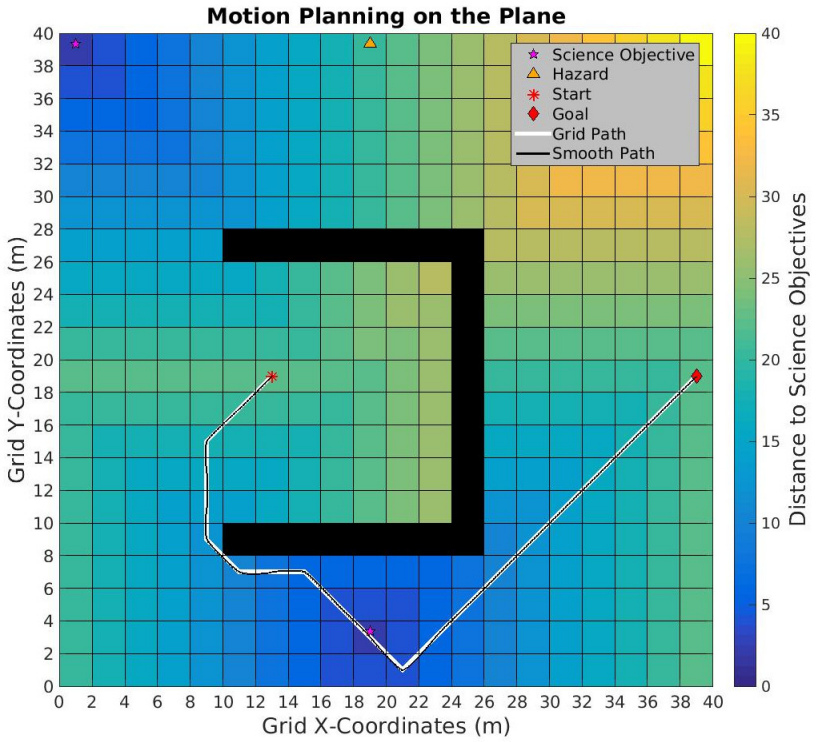

Figure 5.15: Path Planning for Motion on a Flat Plane.

where c_1 is a constant chosen by the user, and (a, b, c) are the quadratic coefficients penalizing $w_{||}$, defined by choosing $(\bar{w}, \sigma)$. The minimum edge weight occurs when the wind at v_i has a speed of $\bar{w}$ and is aligned in the direction of d_j.

Edge costs associated with the local topology are handled similarly to edge costs rewarding favorable wind gusts. Each vertex corresponds to a point on the terrain. At each vertex, the idea is to compute the torque caused by the gravitational force acting at the BSR's center of rotation, and weight an edge to a neighboring vertex based on the torque's alignment relative to the adjacent vertex. Recall from Subsection (4.2.3) that the torque due to the BSR's structure is given by,

$$T^g = r_b N \times (-M_s g e_3),$$

where N is the surface normal expressed in an inertial frame and M_s is the structure mass consisting of all vehicle components whose center of mass is centered at the COR. The torque T^g lies in the tangent plane of the surface at v_i. Let d_j denote the unit vector on the tangent space that points towards an adjacent vertex v_j. Then,

$$T^g_\perp = \langle T_g \times d_j, N \rangle = M_s g r_b \langle d_j, e_3 \rangle$$

denotes the component of the torque perpendicular to d_j. Gravity impedes motion along d_j when $T^g_\perp > 0$, and assists motion along d_j when $T^g_\perp < 0$. Let $T^g_{||} = \langle T^g, d_j \rangle$ denote the gravitational torque parallel to d_j, which corresponds to rotations orthogonal to d_j.

If $T^g_\perp$ is too large in magnitude, then energy-harvesting will be prohibited as the magnets will again be pinned to their outer edges via centrifugal forces. Let $||T^g_\perp||_{max}$ and $||\bar{T}^g_\perp||$ denote the maximum and optimal assistive torque magnitudes, respectively. Then, $T^g_\perp$ is weighted using a quadratic function whose minimum value is zero, centered at $||\bar{T}^g_\perp||$. The quadratic's remaining degrees of freedom are chosen by penalizing $T^g_\perp = -||T^g_\perp||_{max}$ and $T^g_\perp = 0$ equally, by some value σ greater than zero. Any value of $T^g_{||}$ is undesirable for sustaining motion along d_j such that $e^{gravity}_{ij}$ is defined by,

$$e^{gravity}_{ij} = c_1(T^g_{||})^2 + a \cdot (T^g_\perp)^2 + b \cdot (T^g_\perp) + c, \tag{5.36}$$

where c_1 is a constant chosen by the user, and (a, b, c) are the quadratic coefficients penalizing $T^g_\perp$, defined by choosing $(||\bar{T}^g_\perp||, \sigma)$. The minimum edge weight occurs when T^g is aligned along d_j with a magnitude $||\bar{T}^g_\perp||$.

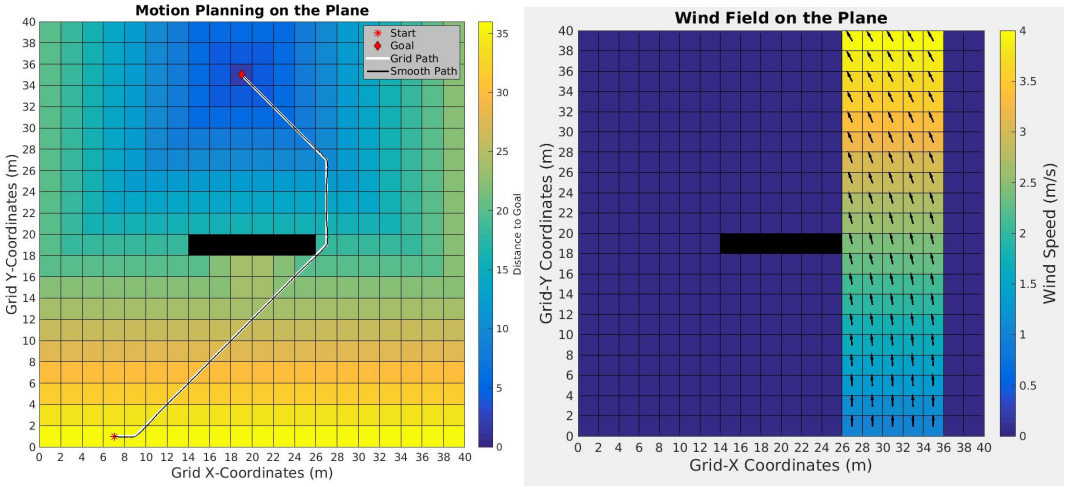

(a) Optimal Path in the Presence of Wind. (b) Wind Field On the Plane.

Figure 5.16: BSR Navigating to a Goal on the Plane in the Presence of Wind.

In Fig. 5.15, a trajectory is planned over a flat plane in the presence of scientific objectives and a hazard. The grid resolution is $2m$ and two scientific objectives are present on the plane (upper-left corner and lower-center). A hazard is located on the plane (upper-center) and a horseshoe obstacle depicted in black is centered in the plane. Each grid is colored according to a heatmap that corresponds to the

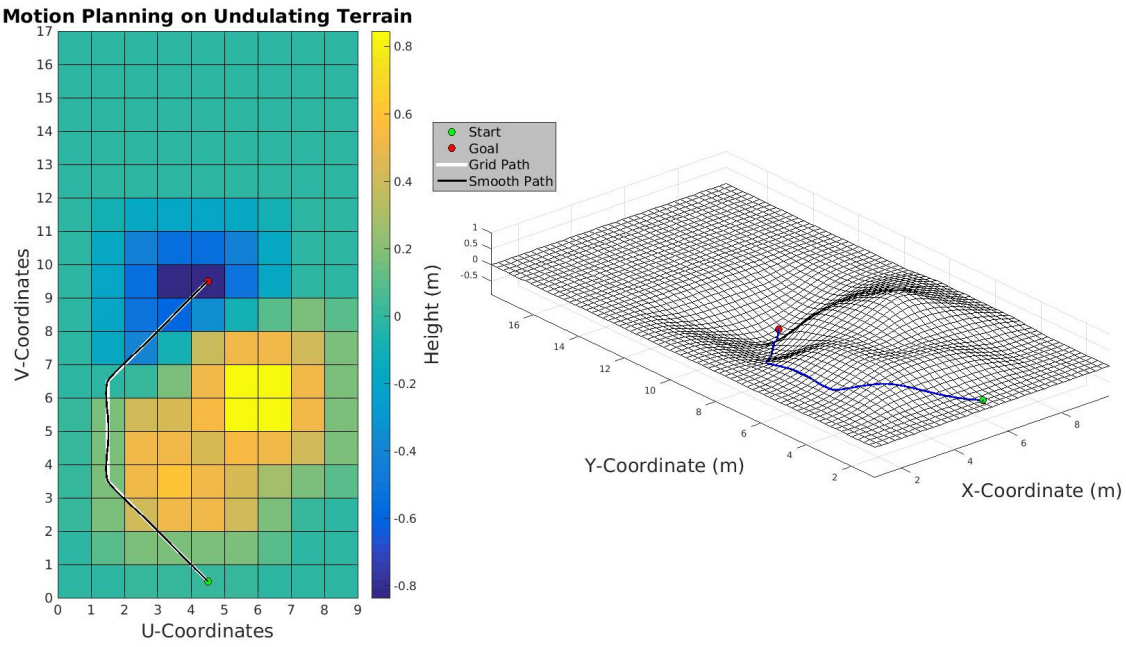

Figure 5.17: Topology Costs on Undulating Terrain.

proximity, δ, from the scientific objective using the wavemap. The vehicle begins in the center of the obstacle and must end its motion to the right-center of the grid. Based on the edge weights described above, a trajectory is identified using the A^* algorithm. This trajectory is biased towards the scientific objective and away from the hazard. As the trajectory is originally expressed in a grid-world, an interpolation scheme is used to smooth the trajectory for use in the feedforward and feedback controllers.

Incorporating wind into the motion planning scheme is demonstrated in Fig. 5.16. A wind field with speeds ranging from $1m/s$ to $4m/s$ acts over a portion of the plane shown in (5.16b), and the minimum cost path is identified in (5.16a). The wind speed optimal for energy harvesting, $\bar{w}_{||}$, is chosen as $2m/s$ and the maximum desirable wind speed, $||w||_{max}$, is chosen to be $5m/s$. From (5.16a), the BSR's desired path deviates from the shortest-distance path to take advantage of the present wind field, which can be used to harvest energy along the path to the goal. Topology costs are implemented for undulating terrain in Fig. 5.17. Similar to defining a grid over a plane, path planning is conducted in the surface's pre-image and the resulting minimum cost trajectory is projected onto the surface using the terrain map, $\varphi(u,v)$. In Fig. 5.17, a generic BSR begins its motion behind a series of low hills and the goal is located in a small valley. With topology edge costs, the minimum cost trajectory prevents the vehicle from scaling the hills (where gravity acts against the

motion), and instead guides the vehicle around the hills and down the valley to the objective. Proximity edge costs based on hazards and objectives, and vector costs associated with ambient wind fields and local topologies can be combined into a single path planner that intelligently selects energy-optimal trajectories.

This chapter detailed Moball's simulation environment, including a Lie-algebra based adaptive integrator and the use of BBPs to model smooth terrain. Then, Moball's control architecture was reviewed and two generic feedback controllers were introduced for BSRs and validated in simulation. A "ballistic" controller was proposed to cope with the lack of control authority over Moball's magnets, which involved solving a QP to determine the impulse to apply to a magnet passing a solenoid. Then, a feedforward path controller was developed based on numerical direct collocation, which enables Moball to follow arbitrary trajectories on the plane. Finally, a motion planning framework was introduced, enabling paths to be charted across smooth terrains while respecting scientific objectives, hazards, and the need to harvest energy from local wind fields and topology.

Chapter 6

CONCLUSION

The intent of this work was to provide a broad, rigorous framework to support the development of spherical vehicles intended for scientific exploration, with Moball as a motivating example. Chapters 3-5 introduced the main components of this framework as follows.

A spherical robot's dynamics possess geometrical structures that can be exploited to facilitate the analysis of control-theoretic issues, such as controllability or motion-planning. Lagrangian reduction and reconstruction using the nonholonomic connection is an expedient means to simplify the equations of motion and expose the underlying structure. Reduction and reconstruction based on the BKMM method was extended to dynamical systems with broken symmetries in Chapter 3. Incorporating advected parameters as additional states in the reduction step enables the symmetries of the kinetic energy to be applied to the entire system. In nearly all robotic systems this implies that the equations of motion can be reduced by $SO(3)$, which obviates the need to parameterize the rotation group using chart-dependent parameterizations such as Euler angles. Reconstruction leads to the nonholonomic connection that clarifies the role of momentum and actuator inputs in generating and sustaining vehicle motion. The nonholonomic connection provides the structure that is so useful in determining the controllability of spherical robotic vehicles. The method of deriving a system's dynamic equations introduced in Chapter 3 is generic and applies to dynamical systems with nonholonomic constraints (rolling, sliding, walking vehicles) as well as unconstrained systems (underwater or multi-rotor flying vehicles).

Chapter 4 used the reduction/reconstruction results of Chapter 3 to analyze the small-time local controllability (STLC) properties of spherical robots. The nonholonomic connection introduced the steering matrix, whose surjectivity can be used to determine whether a particular spherical vehicle is STLC. Local controllability was established using Sussmann's condition, without linearizing the system's full-order dynamics. Importantly, the theorems establishing STLC are identical for a spherical vehicle rolling on a flat plane, sloped, or generic undulating terrain. As the steering matrix depends on the internal construction of the vehicle, one may

easily understand how design changes or potential damage may impact a specific vehicle's controllability in the field. To illustrate the flexibility of the theory, STLC over the attitude and position of a class of commonly encountered multirotor aerial robots was also included in Chapter 4.

Controllers, motion-planning, and a simulation environment were introduced for Moball in Chapter 5, although many of these algorithms are generally applicable to Barycentric Spherical Robots (BSRs) and other spherical robots. A set of feedback-linearizing and PID controllers were developed for use by any BSR on flat or generic, undulating terrain. Each of these controllers were validated in a simulation environment where terrain is modeled using Bicubic B-Splines and the dynamics are integrated using geometric numerical techniques. Then, a ballistic-impulse controller was introduced that overcomes the lack of control authority inherent in Moball's electromechanical design. An impulse, whose magnitude is solved for using a QP, is applied when a magnet crosses one of Moball's solenoids. Following the impulse, the magnet is free to travel ballistically until a subsequent solenoid crossing. This unique controller was also validated in simulation. Next, a feedforward controller was developed specifically for Moball. Imposing a virtual constraint on Moball's inputs enabled a simplified dynamical model to be developed, which underpins the feedforward controller. Then, direct collocation was used to numerically identify a control policy that minimizes trajectory error and the force applied to Moball's magnets. Lastly, an energy-opportunistic motion-planning framework was introduced in Chapter 5. This algorithm finds a trajectory over undulating terrain that balances scientific objectives and hazard avoidance with the imperative of exposing the vehicle to external sources of energy, such as wind fields and the local topology. Such a motion planner is appropriate for any spherical vehicle that harvests external sources of energy in the environment.

6.1 Future Work

Although a comprehensive framework for the analysis and control of spherical vehicles was introduced in this thesis, the following topics are promising avenues of future work.

6.1.1 Changes to Moball's Vehicle Design

Moball's energy-harvesting and locomotion capabilities both stem from the same electromechanical apparatus consisting of internal dipole magnets and solenoids. Although this arrangement can be implemented in hardware with few components,

there are compelling reasons to separate the steering from the energy-harvesting subsystems.

It is recommended that the next Moball prototype harvest energy along a single internal axis while steering is accomplished by reaction wheels mounted orthogonally to the energy-harvesting axis. By steering using reaction wheels, the maximum torque is no longer limited by the vehicle's radius or the mass of an internal magnet. Consequently, a vehicle driven by reaction wheels would likely be able to traverse slopes with greater inclination angles and rougher terrain. Steering using reaction wheels would also eliminate the restrictive control authority that is inherent when controlling a magnet using a solenoid. Whereas the ballistic-impulse controller in Chapter 5 is necessary to control Moball's magnets, a vehicle using reaction wheels could take advantage of existing, proven, and continuous controllers.

Using reaction wheels to steer would considerably simplify the vehicle's electrical systems. Currently, a dual-purpose electrical circuit is required to absorb current harvested by a solenoid and then provide current to the same solenoid in order to control the internal magnet. Such a circuit is necessarily complex, custom, and expensive. Separating steering from energy-harvesting would require a simpler circuit whose function could be dedicated, and optimized, to harvesting energy. In the experiments detailed in Appendix A, different solenoid geometries were found to be optimal for energy-harvesting and control. Combining these roles then requires a compromise between energy-harvesting and control performance in the solenoid's design. When the vehicle is steered using reaction wheels, the solenoids can be optimized for harvesting energy, which would improve the efficiency and increase the performance of energy-harvesting on a per solenoid basis.

Separating Moball's energy-harvesting and steering capability may also decrease the architecture's risk. Damage to the vehicle's reaction wheels need not terminate a scientific mission, as the vehicle can continue to harvest energy and function as a passive, but mobile, sensor platform. However, if energy-harvesting and locomotion are combined in the same apparatus, then damage to this system, or more likely its electrical circuitry, may threaten the viability of the mission. Secondly, relying on reaction wheels for steering minimizes the risk of development. Reaction wheels and control-moment gyroscopes are mature technologies that have previously been deployed in space-based applications. These technologies, their electrical, and control systems can be acquired and implemented with greater confidence, and more cheaply, than Moball's current actuator scheme.

6.1.2 Application of Dynamics to Other Robotic Systems

The Lagrangian reduction and reconstruction method introduced in Chapter 3 is general, and has already been extended to a number of systems other than spherical robots. Of particular interest is the extension of this theory to legged locomotion, such as bipedal robotics. A bipedal robot is characterized by a broken symmetry, e.g. the system's kinetic energy is invariant with respect to $SE(3)$ but the Lagrangian's symmetry is limited by the potential energy's symmetry group, which is $SE(2)$. The method of advected parameters employed in Chapter 3 can then be readily applied to bipedal robots. Care must be taken, however, as these systems are described by hybrid systems and the notion of a Lagrangian symmetry would need to be extended to this case.

Another domain in which our dynamics formulation may apply is underwater vehicles. Similar to bipedal robots, these systems will experience a broken symmetry due to gravity, however there may also be a broken symmetry due to orientation dependent buoyancy forces. Again, it is anticipated that the incorporation of advected parameters will permit the dynamics of underwater vehicles to be reduced by $SO(3)$ and reconstructed using the method in Chapter 3. The reconstruction equation would be particularly useful for underwater systems that manipulate their environment using robotic arms, as the connection would describe how actuating the robotic limbs causes drift of the vehicle body.

6.1.3 Generalizing Feedforward Controller

The development of Moball's feedforward controller was largely dependent on a simplified dynamic model that resulted from the application of a virtual constraint, which was derived in Subsection (5.5.2). The virtual constraint's objective is to cancel the quadratic terms that arise from inertial forces in the nonholonomic momentum differential equation, Eq. (4.30), such that only gravity and damping terms remain. After all, torques due to gravity are the dominant terms sustaining BSR motions. An interesting area of future work is to identify virtual constraints that to simplify the momentum differential equation for Moball, and generic BSRs, on undulating terrain.

As an example, consider the nonholonomic momentum differential equations of Moball on undulating terrain, adapted from Eq. (4.27) for the Moball model in

Subsection (4.3.1),

$$\dot{p}_\alpha = r_b M_i(\omega^b_\alpha - \omega^b_{G,\alpha})\Big(\omega^b_\alpha\langle\mathcal{X},\beta\rangle - \omega^b_\beta\langle\mathcal{X},\alpha\rangle + \langle\mathcal{V},\gamma\rangle\Big) + \omega^b_{G,\gamma}p_\beta + T^{net}_\alpha(\mathcal{X}),$$
$$\dot{p}_\beta = r_b M_i(\omega^b_\beta - \omega^b_{G,\beta})\Big(\omega^b_\alpha\langle\mathcal{X},\beta\rangle - \omega^b_\beta\langle\mathcal{X},\alpha\rangle + \langle\mathcal{V},\gamma\rangle\Big) - \omega^b_{G,\gamma}p_\alpha + T^{net}_\beta(\mathcal{X}),$$

where T^{net} is the torque due to gravity and $\{\alpha,\beta,\gamma\}$ denotes a local normalized Gauss frame with ω^b_G as its angular velocity in a body-fixed frame. Previously, the virtual constraint imposed that $\langle\mathcal{X},\gamma\rangle \equiv$ const. In the case of undulating terrain, let

$$\langle\mathcal{X},\gamma\rangle \equiv \mathcal{X}_\gamma(t).$$

The objective is to find conditions on $\mathcal{X}_\gamma(t)$ that will simplify the nonholonomic momentum differential equation. Differentiating the virtual constraint yields,

$$\dot{\mathcal{X}}_\gamma(t) + \langle\mathcal{X},\beta\rangle\omega^b_{G,\alpha} - \langle\mathcal{X},\alpha\rangle\omega^b_{G,\beta} = \omega^b_\alpha\langle\mathcal{X},\beta\rangle - \omega^b_\beta\langle\mathcal{X},\alpha\rangle + \langle\mathcal{V},\gamma\rangle.$$

From this, we find that if

$$\dot{\mathcal{X}}_\gamma(t) = \langle\mathcal{X},\alpha\rangle\omega^b_{G,\beta} - \langle\mathcal{X},\beta\rangle\omega^b_{G,\alpha},$$

then the nonholonomic momentum differential equation will be greatly simplified:

$$\dot{p}_\alpha = \omega^b_{G,\gamma}p_\beta + T^{net}_\alpha(\mathcal{X}),$$
$$\dot{p}_\beta = -\omega^b_{G,\gamma}p_\alpha + T^{net}_\beta(\mathcal{X}).$$

This idea suggests that instead of constraining the system's input to a constant value along the direction of the surface normal, perhaps a virtual differential equation constraint would be more effective in simplifying the nonholonomic differential equation. More generally, it would be worthwhile to consider if a virtual constraint may simplify the momentum differential equation (4.27) for a generic BSR on smooth terrain, as such a simplification would enable the feedforward controller developed in Section (5.5) to be applied generally.

Another area of future work is to improve the feedforward controller's run-time to enable dynamic, online adjustments. The numerical optimization defining the feedforward controller can be solved in less than $20s$, which is sufficient provided that the platform moves slowly before initiating its plan. To decrease the run-time of the feedforward controller, one may imagine using reinforcement learning to select, or interpolate between, open-loop trajectories from a previously-computed library of solutions. Since running numerical simulations to create a training data set is relatively cheap and machine learning algorithms are becoming ubiquitous in robotics, this seems like a promising method to enable real-time performance of the feedforward controller on generic terrain.

6.1.4 Feedback Linearizability of Spherical Robots

In Chapter 4, STLC conditions were derived for generic spherical vehicles rolling on arbitrary terrain. The conditions for establishing controllability are closely related to the conditions establishing feedback linearizability. One avenue of future work would be to derive these conditions of feedback linearizability over the path error dynamics or orientation of the ball.

6.1.5 Relaxing Constraints & Model Assumptions

Several physical constraints were assumed in this work, including no-slip and no-spin rolling constraints as well as a curvature constraint that assured a single point of contact between a spherical vehicle and the terrain. An interesting extension of this work may include relaxing these constraints. Modeling surface friction, either with point or patch contact, and permitting slip may provide a more realistic simulation of a spherical vehicle in icy ground. Or, permitting the vehicle to travel over terrain without curvature constraints and permitting more than one point of contact with the ground may be considered.

Another assumption adopted in this work is that the spherical robot's shell is rigid. Videos of JPL's Tumbleweed show the vehicle bouncing through terrain, where the vehicle temporarily leaves the ground, and clearly deforming as it contacts the surface. Perhaps modeling the sphere as a flexible and deformable body would better capture the motions of these vehicles in practice, although modeling a deformable sphere may introduce a potentially infinite-dimensional state. Modeling a bouncing ball would also involve treating the vehicle as a hybrid system, with dynamics describing the vehicle in contact with the ground and airborne. It is possible that spherical vehicles traverse rough terrain more efficiently via bouncing than via smooth rolling, which may be an interesting line of investigation.

6.1.6 Extensions of Motion Planning Framework

In Chapter 5, a basic motion planning framework was developed for spherical vehicles that can harvest kinetic energy from the wind. Of course, knowledge of the local winds is a prerequisite for such an approach and in simulation the wind fields were known and time-invariant. In reality, wind fields in the Arctic and Antarctic vary with time and exhibit clear seasonal and diurnal variations. An extension of the motion planning framework would involve incorporating a time-varying, stochastic wind model based on real observations taken from the North or South Poles. A motion planner with time-varying wind fields would enable longer duration missions

to be planned, and would increase the likelihood of success for such missions.

Incorporating the system dynamics of a specific vehicle platform is another extension to the motion planning framework. Currently, the motion planner does not use any information from a specific vehicle model. However, knowledge of a vehicle's dynamic model could help in characterizing terrain as impassible or hazardous.

Appendix A

MOBALL DESIGN & EXPERIMENTS

The following experimental results have been previously published in [7, 8, 15, 18].

A.1 Physical Design

Moball's outer shell is composed of several fiberglass battens, arranged radially, which are bent to connect at antipodal points. Tension in the battens provide Moball with elasticity as it rolls. Moball is protected by a Mylar skin, which is abrasion and water resistant. Access to the vehicle's interior is enabled by a waterproof zipper. Moball's electronics are enclosed in an aluminum box at the center of the vehicle. Contained within this box are Moball's avionics, scientific sensors, a control computer, and a lithium-polymer battery to store harvested energy. Each inner tube is made from laminated carbon-fiber in order to reduce weight and prevent eddy currents from forming in the tubes[1]. A $2m$-diameter Moball prototype was constructed for field tests (see Fig. 1.2). The prototype's net weight is approximately $40kg$, although a target weight of $20kg$ is desirable for optimal field use.

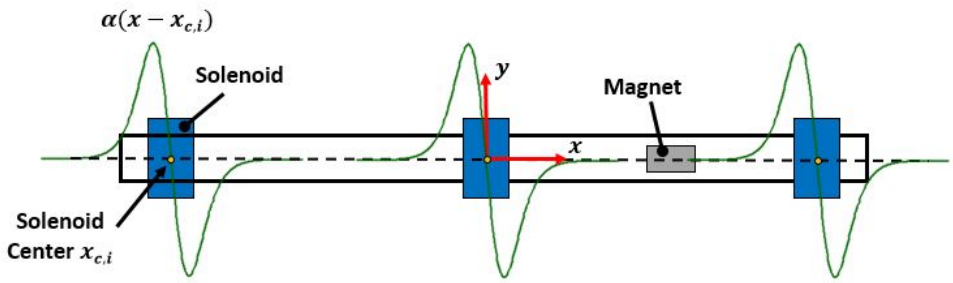

Figure A.1: Electromechanical Coupling Between Magnet and Solenoid.

A.2 Electromechanical Modeling & Design

Moball's energy harvesting depends on the electromagnetic induction between a stationary solenoid and a moving dipole magnet (see Fig. A.2). The magnet's velocity is proportional to the induced voltage through an electromechanical coupling function, $\alpha(\cdot)$,

$$v = \alpha(\bar{x})\dot{x},$$

[1] Eddy currents dampen the magnet's motion and lead to energy-harvesting inefficiencies

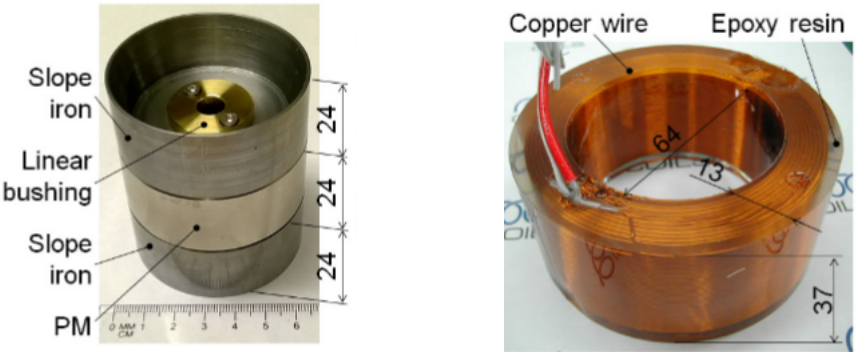

(a) Permanent magnet (PM) and sloped steel attachments to improve energy-harvesting

(b) Epoxy-impregnated copper solenoid

Figure A.2: Magnet Assembly and Solenoid. Dimensions in Millimeters. [7].

where the coupling function depends on the relative distance between the magnet and solenoid $\bar{x} = x - x_{c,i}$, the state of the magnet is $(x, \dot{x})$, and the position of the i^{th} solenoid is $x_{c,i}$. This function is shown schematically in Fig. A.1. The specific form of $\alpha(\bar{x})$ depends on the magnet and solenoid geometries and can be derived as,

$$\alpha(\bar{x}) = \oint_{L_w} B_r(\bar{x}) dL = \Big(\frac{1}{L_w} \oint_{L_w} B_r(\bar{x}) dL\Big) L_w \approx \Big(\frac{1}{V_c} \iiint B_r(\bar{x}) dV\Big) L_w,$$

where L_w is the length of wire used in the solenoid, $B_r(\bar{x})$ is the radial component of the magnetic flux at the solenoid, and V_c is the solenoid's volume [42]. Passing from the line to the volume integral follows by assuming a tightly wound solenoid; in which case the flux density over the total length of wire is approximated as the flux density over the solenoid's total volume. This volume integral can be solved analytically for the case of a simple cylindrical magnet travelling through a cylindrical solenoid.

One can see that the magnitude of $\alpha(\bar{x})$, and thus the efficiency of energy-harvesting, depends directly on the radial component of the magnetic field emanating from the dipole, $B_r(\bar{x})$. Sloped steel cups are attached to the ends of each magnet (shown in Fig. A.2a), which act as a lens to direct the magnetic field radially. A commercial finite-element software (JMAG, JSOL Corp., Japan) was used to model the magnetic flux density and eliminate low-density areas of the steel attachments, leading to the cupped shape. In [7], the addition of the sloped steel cups improved energy harvesting by approximately 30%. The magnets are rare earth NdFeB magnets and

the weight of the magnet assembly with steel attachments is approximately one kilogram.

Notice from Fig. A.1 that $\alpha(\bar{x})$ is nonlinear, and sharply peaked on both sides of the solenoid's center. The coupling function is also odd, signifying that induced currents may flow in either direction through the solenoid depending on the magnet's motion. As a result of the bidirectional current, a buck-converter is required to store the induced current to a battery (see [8] for a description and experiments). The coupling function is zero at each solenoid's center due to symmetry, i.e. an equal magnetic flux passes into and out of the solenoid at this position.

Locomotion is enabled by the same electromechanical apparatus that is used to harvest energy. Applying a current, i, to a solenoid will impart a force, F, to a nearby magnet proportional to the same function $\alpha(\bar{x})$ as described above,

$$F = \alpha(\bar{x})i.$$

Inherent to this actuation scheme is the challenge of limited control authority. The function $\alpha(\bar{x})$ relating current to imparted force is nonzero only in a small neighborhood around each solenoid. Using the magnets and solenoids as described in [7], control authority is negligible when the magnet is more than 2" from the center of each solenoid. A ballistic control scheme based on imparting impulses to a magnet near the peaks of $\alpha(\bar{x})$ is developed in Chapter 5 to overcome this challenge.

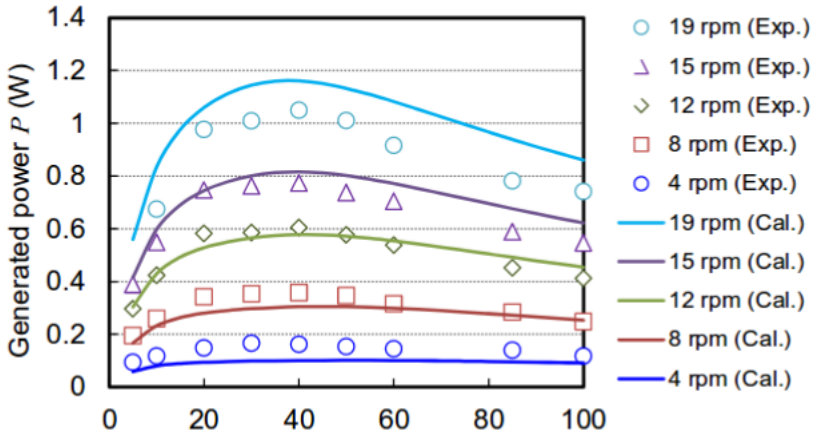

Figure A.3: Power of Single Solenoid Rotation Test vs. Resistive Load. [7].

A.3 Experimental Results

Several tests were conducted to measure and optimize Moball's energy-harvesting and control system. In [7], a benchtop test was conducted to validate the electromechanical model and measure the amount of harvested energy. This test involved rotating a 0.8-m long rod about its center at a variety of rotational speeds. A dipole magnet assembly slid along the rod and a single solenoid was affixed at the center of the rod's length. Power was measured over a dummy resistor and the data was wirelessly transmitted to a base station, the results of which are shown in Fig. A.3.

This figure shows the average power measured over one rotational period for several angular velocities, in addition to the electromechanical model's predictions. Interestingly, the average harvested power strongly depends on the impedance of the attached harvesting circuit. Changing the impedance affects the electromagnetic damping force applied to the magnet as it passes through the solenoid, which is directly related to the amount of harvested energy. These experiments showed a maximum average power of 1.05 watts at 19 revolutions per minute (RPM) with a load resistance of 40 Ω. Based on the electromagnetic model described above, it is predicted that 6-10 watts of energy can be harvested with three solenoids placed along each inner tube during a 12-24 RPM angular velocity.

In simulation [18] and the benchtop experiment described above [7], it was found that energy harvesting decreases for speeds greater than approximately 25 RPM. At these speeds, centrifugal forces tend to pin the magnets to the sphere's outer shell, preventing the magnets from reciprocating through the solenoids and harvesting energy. Attaching linear springs to the ends of each axis rectifies this problem and enables Moball to harvest energy over a larger range of rotational speeds.

In [15], a full-scale rotational test was conducted. A motor rotated Moball about its center such that four inner tubes were in the plane of rotation and two inner tubes were stationary, and thus removed. Two solenoids were attached to each tube and power was measured over each solenoid using a load resistor, as before. The results of this test are shown in Fig. A.4. Similar to earlier predictions, an average power of 7.2 watts was gathered by the solenoids while rotating at 20 RPM with a load of 47 Ω for each solenoid. Above approximately 22 RPM, energy harvesting decreased due to centrifugal forces. Deviations between experiment and simulation are believed to be caused by unmodelled dissipative forces including friction in the bearings on the magnet assembly and air damping within each inner tube.

Control was also tested in [15]. Similar to the rotation test described in [7], a mo-

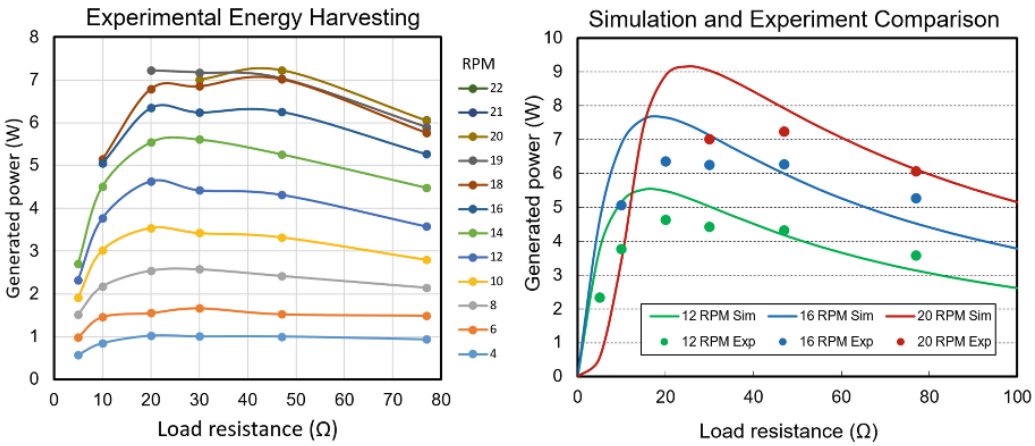

Figure A.4: (L) Power of Full Scale Rotational Experiment, Various Speeds. (R) Predicted and Measured Power. [15].

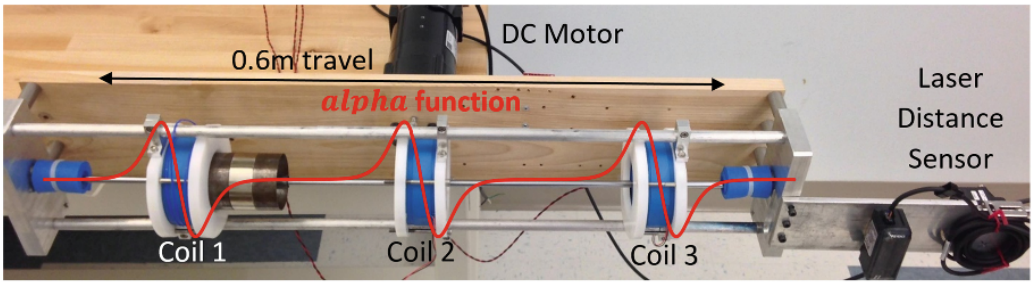

Figure A.5: Control Experiment. Various Frequency Sinusoids are Tracked while Rotated. [15].

tor rotated a 0.8-m rod about its center with three solenoids positioned along the direction of travel as shown in Fig. A.5. The objective of this test was to track a 0.6-m amplitude sinusoidal path of various frequencies by applying currents to the solenoids. A laser measured the position of the magnet, which is necessary for a controller to apply the correct direction of current to a nearby solenoid (since $\alpha(\bar{x})$ is odd). A lithium-polymer battery applied power to the solenoids. A feedback linearized controller was able to achieve 5 cm tracking error or less for rotational periods less than approximately three seconds. Smaller tracking errors may be possible by relying on non-continuous controllers like the ballistic-impulse controller introduced in Chapter 5.

BIBLIOGRAPHY

[1] Amir Homayoun Javadi A and P. Mojabi. “Introducing August: a novel strategy for an omnidirectional spherical rolling robot”. In: *2002 IEEE International Conference on Robotics and Automation*. 2002, 3527–3533 vol.4.

[2] J Alves and J Dias. “Design and control of a spherical mobile robot”. *Proceedings of the Institution of Mechanical Engineers, Part I: Journal of Systems and Control Engineering* 217.6 (2003), pp. 457–467.

[3] Jeffrey Antol et al. “Low cost mars surface exploration: The mars tumbleweed” (2003).

[4] Jeffrey Antol et al. “The NASA Langley mars tumbleweed rover prototype”. In: *AIAA Aerospace Sciences Meeting and Exhibit*. Vol. 64. 2006.

[5] Vladimir I Arnold. “Sur la géométrie différentielle des groupes de Lie de dimension infinie et ses applicationsa l’hydrodynamique des fluides parfaits”. *Ann. Inst. Fourier* 16.1 (1966), pp. 319–361.

[6] James Arvo. “Fast random rotation matrices”. In: *Graphics Gems III (IBM Version)*. Elsevier, 1992, pp. 117–120.

[7] J. Asama et al. “Design investigation of a coreless tubular linear generator for a Moball: A spherical exploration robot with wind-energy harvesting capability”. In: *2015 IEEE International Conference on Robotics and Automation (ICRA)*. May 2015, pp. 244–251.

[8] J. Asama et al. “Investigation of energy harvesting circuit using a capacitor-sourced buck converter for a tubular linear generator of a moball: A spherical wind-driven exploration robot”. In: *2015 IEEE Energy Conversion Congress and Exposition (ECCE)*. Sept. 2015, pp. 3167–3171.

[9] Karl Johan Aström and Richard M Murray. *Feedback systems: an introduction for scientists and engineers*. Princeton university press, 2010.

[10] Goran Jurisa Basic. “Power-scavenging tumbleweed rover”. PhD thesis. 2010.

[11] Alberto Behar et al. “NASA/JPL Tumbleweed polar rover”. In: *Aerospace Conference, 2004. Proceedings. 2004 IEEE*. Vol. 1. IEEE. 2004.

[12] S. Bhattacharya and S. K. Agrawal. “Spherical rolling robot: a design and motion planning studies”. *IEEE Transactions on Robotics and Automation* 16.6 (Dec. 2000), pp. 835–839.

[13] Antonio Bicchi et al. “Introducing the" sphericle": an experimental testbed for research and teaching in nonholonomy”. In: *Robotics and Automation, 1997. Proceedings., 1997 IEEE International Conference on*. Vol. 3. IEEE. 1997, pp. 2620–2625.

[14] Anthony Bloch et al. *Nonholonomic mechanics and control*. Vol. 24. Springer, 2003.

[15] Joseph Bowkett, Matt Burkhardt, and Joel W Burdick. "Combined Energy Harvesting and Control of Moball: A Barycentric Spherical Robot". In: *International Symposium on Experimental Robotics*. Springer. 2016, pp. 71–83.

[16] Roland Bulirsch et al. "Combining direct and indirect methods in optimal control: Range maximization of a hang glider". In: *Optimal control*. Springer, 1993, pp. 273–288.

[17] Francesco Bullo and Andrew D Lewis. *Geometric control of mechanical systems: modeling, analysis, and design for simple mechanical control systems*. Vol. 49. Springer Science & Business Media, 2004.

[18] M. R. Burkhardt et al. "Energy harvesting analysis for Moball, A self-propelled mobile sensor platform capable of long duration operation in harsh terrains". In: *2014 IEEE International Conference on Robotics and Automation (ICRA)*. May 2014, pp. 2665–2672.

[19] M.P. do Carmo. *Differential Geometry of Curves and Surfaces*. Prentice-Hall, 1976. ISBN: 9780132125895.

[20] Jeff R Cash and Alan H Karp. "A variable order Runge-Kutta method for initial value problems with rapidly varying right-hand sides". *ACM Transactions on Mathematical Software (TOMS)* 16.3 (1990), pp. 201–222.

[21] Hernán Cendra et al. "Lagrangian reduction, the Euler-Poincaré equations, and semidirect products". *Translations of the American Mathematical Society-Series 2* 186 (1998), pp. 1–26.

[22] Richard Chase and Abhilash Pandya. "A Review of Active Mechanical Driving Principles of Spherical Robots". *Robotics* 1.1 (2012), pp. 3–23.

[23] J. Chen et al. "Design and motion control of a spherical robot with control moment gyroscope". In: *2016 3rd International Conference on Systems and Informatics (ICSAI)*. Nov. 2016, pp. 114–120.

[24] H.M. Choset. *Principles of Robot Motion: Theory, Algorithms, and Implementation*. A Bradford book. Prentice Hall of India, 2005. ISBN: 9780262033275.

[25] Faranak Davoodi, Joel Burdick, and Mina Rais-Zadeh. "Moball network: a self-powered intelligent network of controllable spherical mobile sensors to explore solar planets and moons". In: *AIAA SPACE 2014 Conference and Exposition*. 2014, pp. 1–9.

[26] Faranak Davoodi et al. "Moball: An intelligent wind-opportunistic mobile sensor to monitor the polar regions". In: *SENSORS, 2015 IEEE*. IEEE. 2015, pp. 1–4.

[27] James R Forbes, Timothy D Barfoot, and Christopher J Damaren. “Dynamic modeling and stability analysis of a power-generating tumbleweed rover”. *Multibody System Dynamics* 24.4 (2010), pp. 413–439.

[28] Sneha Gajbhiye and Ravi N Banavar. “Local equilibrium controllability of a spherical robot actuated by a pendulum”. In: *Decision and Control (CDC), 2013 IEEE 52nd Annual Conference on*. IEEE. 2013, pp. 1616–1621.

[29] Sneha Gajbhiye and Ravi N Banavar. “The Euler-Poincaré equations for a spherical robot actuated by a pendulum”. *IFAC Proceedings Volumes* 45.19 (2012), pp. 72–77.

[30] Philip E Gill, Walter Murray, and Michael A Saunders. “SNOPT: An SQP algorithm for large-scale constrained optimization”. *SIAM review* 47.1 (2005), pp. 99–131.

[31] Bill Goodwine and Joel Burdick. “Controllability with unilateral control inputs”. In: *Decision and Control, 1996., Proceedings of the 35th IEEE Conference on*. Vol. 3. IEEE. 1996, pp. 3394–3399.

[32] Jonathan L Gross and Jay Yellen. *Graph theory and its applications*. CRC press, 2005.

[33] Ernst Hairer, Christian Lubich, and Gerhard Wanner. *Geometric numerical integration: structure-preserving algorithms for ordinary differential equations*. Vol. 31. Springer Science & Business Media, 2006.

[34] Gregory A Hajos et al. “An overview of wind-driven rovers for planetary exploration”. In: *43rd AIAA Aerospace Sciences Meeting and Exhibit, Reno, NV, Jan*. 2005, pp. 10–13.

[35] Ross L Hatton and Howie Choset. “Geometric motion planning: The local connection, Stokes’ theorem, and the importance of coordinate choice”. *The International Journal of Robotics Research* 30.8 (2011), pp. 988–1014.

[36] Ayonga Hereid et al. “Dynamic Humanoid Locomotion: A Scalable Formulation for HZD Gait Optimization”. *IEEE Transactions on Robotics* (2018).

[37] François Robert Hogan, James Richard Forbes, and Timothy David Barfoot. “Rolling stability of a power-generating tumbleweed rover”. *Journal of Spacecraft and Rockets* 51.6 (2014), pp. 1895–1906.

[38] Darryl D Holm, Jerrold E Marsden, and Tudor S Ratiu. “The Euler–Poincaré equations and semidirect products with applications to continuum theories”. *Advances in Mathematics* 137.1 (1998), pp. 1–81.

[39] Arieh Iserles et al. “Lie-group methods”. *Acta numerica* 9 (2000), pp. 215–365.

[40] Ch Jansch and M Paus. “Aircraft trajectory optimization with direct collocation using movable gridpoints”. In: *American Control Conference, 1990*. IEEE. 1990, pp. 262–267.

[41] Jack A Jones. “Inflatable robotics for planetary applications.” (2001).

[42] Bryan Steven Joyce. “Development of an electromagnetic energy harvester for monitoring wind turbine blades” (2011).

[43] Hossein Karimpour, Mehdi Keshmiri, and Mojtaba Mahzoon. “Stabilization of an autonomous rolling sphere navigating in a labyrinth arena: A geometric mechanics perspective”. *Systems & Control Letters* 61.4 (2012), pp. 495–505.

[44] Wang-Sang Koon and Jerrold E Marsden. “Optimal control for holonomic and nonholonomic mechanical systems with symmetry and Lagrangian reduction”. *SIAM Journal on Control and Optimization* 35.3 (1997), pp. 901–929.

[45] PS Krishnaprasad et al. “Nonholonomic Mechanical Systems with Symmetry” (1996).

[46] K. Landa and A. K. Pilat. “Design and start-up of spherical robot with internal pendulum”. In: *2015 10th International Workshop on Robot Motion and Control (RoMoCo)*. July 2015, pp. 27–32.

[47] Tom Lauwers, George Kantor, and Ralph L Hollis. “One Is Enough!.” In: *ISRR*. 2005, pp. 327–336.

[48] Steven M LaValle. *Planning algorithms*. Cambridge university press, 2006.

[49] P.D. Lax. *Linear Algebra and Its Applications*. Linear algebra and its applications v. 10. Wiley, 2007.

[50] Zexiang Li and John Canny. “Motion of two rigid bodies with rolling constraint”. *IEEE Transactions on Robotics and Automation* 6.1 (1990), pp. 62–72.

[51] Ralph Lorenz et al. “Field testing and dynamic model development for a Mars Tumbleweed rover”. In: *4th International Planetary Probe Workshop*. 2006, pp. 25–29.

[52] Robert Mahony, Vijay Kumar, and Peter Corke. “Multirotor aerial vehicles”. *IEEE Robotics and Automation magazine* 20.32 (2012).

[53] Alessia Marigo and Antonio Bicchi. “Rolling bodies with regular surface: Controllability theory and applications”. *IEEE Transactions on Automatic Control* 45.9 (2000), pp. 1586–1599.

[54] Jerrold E Marsden and Tudor S Ratiu. “Introduction to mechanics and symmetry”. *Physics Today* 48.12 (1995), p. 65.

[55] Jerrold E Marsden and Alan Weinstein. “Comments on the history, theory, and applications of symplectic reduction”. *Quantization of singular symplectic quotients* (2001), pp. 1–19.

[56] Kristi A Morgansen, Benjamin I Triplett, and Daniel J Klein. “Geometric methods for modeling and control of free-swimming fin-actuated underwater vehicles”. *IEEE Transactions on Robotics* 23.6 (2007), pp. 1184–1199.

[57] Ranjan Mukherjee, Mark A Minor, and Jay T Pukrushpan. “Simple motion planning strategies for spherobot: a spherical mobile robot”. In: *Decision and Control, 1999. Proceedings of the 38th IEEE Conference on*. Vol. 3. IEEE. 1999, pp. 2132–2137.

[58] Vijay Muralidharan and Arun D Mahindrakar. “Geometric controllability and stabilization of spherical robot dynamics”. *IEEE Transactions on Automatic Control* 60.10 (2015), pp. 2762–2767.

[59] Richard M Murray et al. *A mathematical introduction to robotic manipulation*. CRC press, 1994.

[60] *NASA Technology Roadmaps: Space Power and Energy Storage*. July 2015.

[61] Emmy Noether. “Invariant variation problems”. *Transport Theory and Statistical Physics* 1.3 (1971), pp. 186–207.

[62] James P Ostrowski. “Computing reduced equations for robotic systems with constraints and symmetries”. *IEEE Transactions on Robotics and Automation* 15.1 (1999), pp. 111–123.

[63] James P Ostrowski and Joel W Burdick. “Controllability tests for mechanical systems with symmetries and constraints”. *J. Appl. Math. Comp. Sci* 7.2 (1997), pp. 101–127.

[64] James P Ostrowski, Jaydev P Desai, and Vijay Kumar. “Optimal gait selection for nonholonomic locomotion systems”. *The International journal of robotics research* 19.3 (2000), pp. 225–237.

[65] James Patrick Ostrowski. “The mechanics and control of undulatory robotic locomotion”. PhD thesis. California Institute of Technology, 1996.

[66] Jim Ostrowski. “Reduced equations for nonholonomic mechanical systems with dissipative forces”. *Reports on Mathematical Physics* 42.1-2 (1998), pp. 185–209.

[67] Jim Ostrowski. “Steering for a class of dynamic nonholonomic systems”. *IEEE Transactions on Automatic Control* 45.8 (2000), pp. 1492–1498.

[68] Henri Poincaré. “Sur une forme nouvelle des équations de la mécanique”. *CR Acad. Sci* 132 (1901), pp. 369–371.

[69] William H Press et al. *Numerical recipes in C*. Vol. 2. Cambridge university press Cambridge, 1996.

[70] Anil V Rao. “A survey of numerical methods for optimal control”. *Advances in the Astronautical Sciences* 135.1 (2009), pp. 497–528.

[71] Edward John Routh. *The elementary part of a treatise on the dynamics of a system of rigid bodies*. Macmillan and Company, limited, 1905.

[72] Majd Saied et al. "Local controllability and attitude stabilization of multirotor UAVs: Validation on a coaxial octorotor". *Robotics and Autonomous Systems* 91 (2017), pp. 128–138.

[73] David Salomon. *Curves and surfaces for computer graphics*. Springer Science & Business Media, 2007.

[74] David Schneider. "Non-holonomic Euler-Poincaré equations and stability in Chaplygin's sphere". *Dynamical Systems: An International Journal* 17.2 (2002), pp. 87–130.

[75] Elie A Shammas, Howie Choset, and Alfred A Rizzi. "Geometric motion planning analysis for two classes of underactuated mechanical systems". *The International Journal of Robotics Research* 26.10 (2007), pp. 1043–1073.

[76] Elie Shammas and Maurıcio de Oliveira. "An Analytic Motion Planning Solution for the Snakeboard." *Robotics: Science and Systems VII* (2012), p. 297.

[77] Jinglai Shen, N Harris McClamroch, and Anthony M Bloch. "Local equilibrium controllability of multibody systems controlled via shape change". *IEEE Transactions on Automatic Control* 49.4 (2004), pp. 506–520.

[78] Jinglai Shen, David A Schneider, and Anthony M Bloch. "Controllability and motion planning of a multibody chaplygin's sphere and chaplygin's top". *International Journal of Robust and Nonlinear Control* 18.9 (2008), pp. 905–945.

[79] Guanghui Shu, Qiang Zhan, and Yao Cai. "Motion control of spherical robot based on conservation of angular momentum". In: *2009 International Conference on Mechatronics and Automation*. Aug. 2009, pp. 599–604.

[80] Steve Smale. "Topology and mechanics. I". *Inventiones mathematicae* 10.4 (1970), pp. 305–331.

[81] Hector J Sussmann. "A general theorem on local controllability". *SIAM Journal on Control and Optimization* 25.1 (1987), pp. 158–194.

[82] Meihua Tai. "Model reduction method for nonholonomic mechanical systems with semidirect product symmetry". In: *Robotics and Automation, 2004. Proceedings. ICRA'04. 2004 IEEE International Conference on*. Vol. 5. IEEE. 2004, pp. 4602–4607.

[83] Oskar Von Stryk and Roland Bulirsch. "Direct and indirect methods for trajectory optimization". *Annals of operations research* 37.1 (1992), pp. 357–373.

[84] Qiang Zhan, Yao Cai, and Caixia Yan. “Design, analysis and experiments of an omni-directional spherical robot”. In: *Robotics and Automation (ICRA), 2011 IEEE International Conference on*. IEEE. 2011, pp. 4921–4926.

[85] Bo Zhao et al. “Dynamics and motion control of a two pendulums driven spherical robot”. In: *2010 IEEE/RSJ International Conference on Intelligent Robots and Systems*. Oct. 2010, pp. 147–153.

[86] Huihua Zhao et al. “3D multi-contact gait design for prostheses: Hybrid system models, virtual constraints and two-step direct collocation”. In: *Decision and Control (CDC), 2016 IEEE 55th Conference on*. IEEE. 2016, pp. 3668–3674.

INDEX